Strongly correlated photons in arrays of nonlinear cavities

Alexandre Le Boité

Université Paris Diderot-Paris 7
Sorbonne Paris Cité

Ecole doctorale: Physique Ile-de-France

Laboratoire Matériaux et Phénomènes Quantiques

DOCTORAT

Physique

Alexandre Le Boité

Strongly correlated photons in arrays of nonlinear cavities

Photons fortement corrélés dans des réseaux de cavités non-linéaires

Thèse dirigée par Cristiano Ciuti et Giuliano Orso

Soutenue le 06 mai 2015

JURY

M.	Johann BLATTER	Rapporteur
M.	Cristiano CIUTI	Directeur de thèse
M.	Rosario FAZIO	Rapporteur
M.	Markus HOLZMANN	Examinateur
M.	Giuliano ORSO	Co-directeur de thèse
M.	Olivier PARCOLLET	Examinateur

Remerciements

Je voudrais tout d'abord remercier le directeur du laboratoire, Carlo Sirtori, pour m'avoir accueilli à MPQ pendant cette thèse.

Je suis reconnaissant à Gianni Blatter et Rosario Fazio d'avoir accepté d'être rapporteurs de ma thèse. Leur mérite est d'autant plus grand qu'ils sont venus de loin pour assister à ma soutenance. Un grand merci également à Markus Holzmann et Olivier Parcollet, mes autres examinateurs, pour l'intérêt qu'ils ont porté à mon travail.

Je souhaite bien sûr remercier ici Cristiano Ciuti. De ses nombreuses qualités scientifiques, je retiendrai tout particulièrement son inventivité débordante et sa grande culture. On l'aura compris, ces qualités assurent la réussite du chercheur. Quand elles se doublent de qualités humaines indéniables, elles en font également un excellent encadrant : son sens de l'humour et son enthousiasme indéfectible m'auront été tout aussi précieux pendant ces trois années et demie.

J'ai également eu la chance d'être encadré par un second chercheur exceptionnel, Giuliano Orso. Qu'il en soit ici remercié. J'ai beaucoup appris de sa manière calme et assurée d'aborder les problèmes physiques, bien loin de l'image mythologique du théoricien illuminé et déconnecté du monde réel. Je garde un souvenir ému de nos nombreuses conversations extra-scientifiques, toujours riches en anecdotes, contées avec un talent certain de la narration. Mon seul regret sera sans doute ne pas avoir rencontré les trois petits protagonistes dont il était souvent question...

Le dynamisme de l'équipe théorie doit aussi beaucoup à ses autres membres, que j'ai eu grand plaisir à côtoyer. Je voudrais remercier tout particulièrement ceux avec qui j'ai eu la chance de collaborer directement, à commencer par Alexandre, qui s'est lancé avec moi dans la "méthode du corner" pendant la dernière partie de ma thèse. Outre notre travail en commun, partager nos idées sur l'enseignement de la physique (ou le choix des meilleures séries...) a toujours été un plaisir. Je dois même avouer que son humour, pourtant si particulier, m'a beaucoup manqué après son départ. Merci également à Stefano, qui nous a

rejoint par la suite et dont la participation cruciale au projet m'a beaucoup apporté. Merci à Florent, dont le coup de pouce sur la fin fut salutaire et qui, j'en suis certain, fera une excellente thèse. Je n'oublie pas les autres membres de l'équipe, tout particulièrement Luc, Juan et notre escapade à Batimore, et Loïc, le théoricien stoïcien de la bande. Merci aussi aux "anciens", Simon, David, Pierre et Motoaki, pour leur accueil à mes débuts dans le laboratoire. Merci aux autres thésards et post-docs du groupe, arrivés plus récemment, Jared, Mizio, Wim, Nicola et Riccardo. Merci à Mickael pour nos conversations cinémato-philosophiques qui j'espère ne s'arrêteront pas là. Merci à Tom, Giulia, Andreas et aux autres membres de la composante info quantique. Merci à Indranil et Édouard pour nos échanges toujours enrichissants.

Je remercie également nos collaborateurs du projet Quandyde pour nos nombreuses discussions stimulantes: merci à Jacqueline Bloch, Alberto Amo et leur équipe du LPN, au groupe d'Alberto Bramati au LKB et à celui de Guillaume Malpuech à l'Institut Pascal.

S'il est vrai que la recherche est souvent un travail solitaire, les doctorants ne sont que très rarement seuls dans leur bureau. Je souhaite ici remercier tous les occupants du "thésarium" 645B, dont j'ai déjà cité quelques-uns, pour tous les moments mémorables passés ensemble. Je n'oublierai pas nos nombreuses soirées "wine and cheese" sur la terrasse (ou plutôt chips et bière...), le mölkky entre midi et deux, l'abonnement Bein sport pour la coupe du monde et le séminaire thésard et son petit déj. Merci, donc, à Jo Buhot pour sa bonne humeur et son sens de l'humour, à Philippe pour les raclettes "norvégiennes", à Constance et Charlotte, mes anciennes voisines de "l'îlot central", pour leur présence réconfortante. Merci à Siham pour sa théorie des beaux gosses, à Pierre pour les BN fraise et le jus d'orange à l'eau chaude. Merci à Hélène pour sa gentillesse et sa générosité à toute épreuve. Merci, à JB, thésard débonnaire, à Romain, Elisa, Bastien, Roméo, Pauline, Ludivine.

Merci aux permanents de l'équipe SQUAP, Alain, Marie-Aude, Max et Yann, avec qui j'ai eu l'occasion de partager de nombreux déjeuners, goûters et pauses thé.

Je voudrais également remercier l'équipe administrative du laboratoire, en particulier Anne et Jocelyne, pour leur efficacité et leur gentillesse.

Merci à Irène, Chloé, Thierry, Doan, Ammara et Benjamin pour tous les moments partagés. Merci à Colin et Dominique d'être venu me voir le jour J.

Je souhaite remercier à nouveau ma tante, Jacqueline Bloch. Son soutien et ses conseils éclairés remontent à mes tous premiers enthousiasmes pour la physique quantique et m'ont

accompagné jusqu'à aujourd'hui.

Je voudrais remercier également mes grands-mères Adi et Myriem pour leur présence chaleureuse le jour de ma soutenance.

Merci aux Fischer, Mattout et Horowitz pour leurs encouragements et leur intérêt pour mes travaux.

Un immense merci à mes parents et à mon frère pour leur soutien de tous les instants. Vous savoir à mes côtés m'a été pendant ces années, et me sera toujours, très précieux. Cette thèse vous doit beaucoup.

Je n'oublie pas Célia et ses nombreux conseils pratiques très appréciés.

Merci à également à la famille Chan-Lang, Solène pour nos longues discussions diverses et variées et pour ses macarons désormais célèbres, Sion pour ses conseils avisés sur ma présentation et ses leçons sur la théorie quantique des champs algébrique, et bien sûr Cynthia, 谢谢你对我的好意和款待，谢谢你的支持。这几年以来，有了机会欣赏你的许多才能，因之而感觉很幸运。

我当然也要感谢 Sophie。谢谢你在我的身边，温柔地照顾我。你的微笑、你的开朗性格总是我最好的鼓励。

Je souhaite dédier ce manuscrit à la mémoire de mes grands-pères, François Le Boité et Claude Bloch, en témoignage d'amour et d'admiration.

Résumé

Les progrès réalisés ces dernières années dans le contrôle des interactions photon-photon dans les milieux optiques non-linéaires ont permis l'observation expérimentale de fluides quantiques de lumière. Un des défis actuels du domaine est d'augmenter la force de ces interactions, afin d'atteindre le régime dit "fortement corrélé". Dans un tel régime, les effets des interactions deviennent importants dès que le système contient plus d'une particule, donnant ainsi lieu à de fortes corrélations quantiques. Pour atteindre cet objectif, les réseaux de cavités non-linéaires sont des candidats prometteurs. Nous montrons tout d'abord (chapitre 1), que de tels réseaux de cavités peuvent être décrits par une version hors-équilibre du modèle de Bose-Hubbard dans laquelle les pertes des cavités sont compensées par un pompage laser extérieur. Les photons ayant un temps de vie fini, ces systèmes sont en effet intrinsèquement hors-équilibre et les phénomènes dissipatifs y jouent un rôle important. L'étude théorique des différents états stationnaires de ce modèle quantique est le sujet principal de ce travail de thèse.

Dans sa formulation la plus générale et pour un nombre arbitrairement grand de cavités, le modèle de Bose-Hubbard hors-équilibre est, comme la plupart des modèles de physique à N corps, trop complexe pour être résolu de manière exacte. Il devient alors nécessaire de s'appuyer sur certaines approximations. En particulier, nous considérons dans un premier temps un réseau infini et calculons les états stationnaires dans le cadre de l'approximation de champ moyen (chapitre 2 et 3). La principale hypothèse simplificatrice est d'imposer une forme factorisée pour la matrice densité du système (ansatz de Gutzwiller). Cette approche est d'abord appliquée (chapitre 2) au régime de faible pompage et faible dissipation [22]. L'exploration de ce régime est essentielle pour une meilleure compréhension des relations entre le modèle de Bose-Hubbard hors-équilibre et son homologue "à l'équilibre", mieux connu et s'appliquant à des particules matérielles à l'équilibre thermique. Le modèle à l'équilibre se caractérise entre autres par une transition de phase quantique entre un état isolant de Mott et état superfluide. Dans le cadre du modèle hors-équilibre, nous identifions un équivalent

de l'état isolant de Mott sous la forme d'un mélange statistique d'états de Fock ayant une densité de photons deux fois moins élevée qu'un état de Fock pur, mais avec la même valeur de la fonction d'auto-corrélation d'ordre deux, $g^{(2)}(0)$. Ces états non-classiques de la lumière apparaissent lorsque la fréquence du laser est à résonance avec des processus d'absorption multi-photons. Il est montré que ces états existent jusqu'à une valeur critique du couplage entre les cavités, au-delà de laquelle une transition vers des états (classiques) quasi-cohérents a lieu. L'étude du régime de faible pompage et faible dissipation révèle également qu'hors des résonances multiphotoniques, une faible densité de photon dans l'état stationnaire peut être associée à de fortes fluctuations dans la statistique des photons, se manifestant par un phénomène de fort groupement de photons (*photon superbunching*), au voisinage de la résonance à deux photons.

L'approche de champ moyen est ensuite généralisée au cas d'un pompage et d'une dissipation arbitraire [23] (chapitre 3). Un diagramme de phase général est établi en utilisant une solution exacte du problème à une cavité. Cette solution s'appuie sur la représentation P complexe de la matrice densité. Un des traits caractéristiques du diagramme de phase est l'apparition d'une bistabilité induite par le couplage entre les cavités. Pour une large portion de l'espace des paramètres, la théorie de champ moyen prédit en effet l'existence de deux états stationnaires stables. Les propriétés des deux états stationnaires dans la région bistable sont liés aux états identifiés dans le régime de faible pompage et faible dissipation. L'un est caractérisé par une faible densité mais un fort groupement des photons (*photon bunching*). Dans l'autre, la densité est beaucoup plus élevée et les photons dégroupés (*photon anti-bunching*), en accord avec le cas des résonances multiphotoniques exposé précédemment. L'étude de la stabilité de ces solutions révèle également que dans la région monostable, pour certaines valeurs des paramètres, l'unique solution de champ moyen est instable. Ces instabilités indiquent la formation d'une phase inhomogène dans le système.

La principale motivation derrière l'emploi de l'approximation de champ moyen est avant tout sa prédiction qualitativement correcte de la transition isolant de Mott-superfluide du modèle à l'équilibre. Cette approximation ne peut cependant pas être contrôlée *a priori* et sa validité doit être testée par une comparaison avec d'autres résultats plus précis. Pour ce faire, nous présentons les résultats de simulations numériques exactes sur des réseaux de taille finie (chapitre 4). Le défi principal de cette approche est la dimension de l'espace de Hilbert, qui croit exponentiellement avec la taille du réseau. Toute simulation numérique "brutale" d'un réseau de grande taille est alors impossible. Pour contourner cette difficulté, nous développons une nouvelle méthode consistant à résoudre l'équation maîtresse gouver-

nant la dynamique du système dans une "petite partie" de l'espace seulement, mais contenant les états les plus importants [24]. La précision des résultats obtenus est contrôlée en augmentant progressivement la dimension de cette "petite partie", jusqu'à ce que les valeurs des différentes observables convergent. Appliquant cette méthode au modèle de Bose-Hubbard hors-équilibre, nous montrons que la théorie de champ moyen constitue une bonne approximation pour des petites valeurs du couplage entre les cavités. Des déviations significatives apparaissent lorsque le le couplage augmente et devient comparable à l'interaction photon-photon. Ces résultats numériques constituent la première étape d'un projet ambitieux et offrent de nombreuses perspectives. En particulier, la méthode présentée, spécifiquement conçue pour des systèmes dissipatifs avec pompage extérieur, peut être appliquée à de nombreux modèles sur réseaux. De futurs travaux pourront porter par exemple sur des réseaux à géométrie complexe, avec frustration ou désordre. L'étude des champs de jauges artificiels dans les réseaux de cavités est également envisageable et prometteuse.

Contents

Introduction

It is a common belief that titles of scientific PhD thesis must be utterly unintelligible to ordinary mortals. Judging by the bewildered faces and blank stares I often encountered while trying to convince people that my subject was fascinating, I am afraid that this manuscript is, in this respect, no exception to the rule. To make things worse, its title might even be puzzling for the physicist, as it contains an apparent contradiction. Indeed, how could photons, which are thought to be noninteracting particles, be strongly correlated? This paradox contributes of course to the charm of the subject.

Even before considering interacting photons, the simple fact of exploring, theoretically or experimentally, the particle-like behavior of light is in itself worthy of interest. After more than a century of quantum mechanics, the concept of photon has become very familiar to us, but one must not forget how traumatic an experience was the introduction of light quanta at the beginning of the XX^{th} century. Planck himself, when he presented for the first time his new results explaining the law of black-body radiation, had not yet accepted all the conceptual consequences of his discovery. He considered quanta solely as a working hypothesis, and described right away how calculations should be performed in case the energy was not a multiple of the elementary quantum. At that time, probably only Einstein was ready for the great quantum leap forward [1]. Needless to say, it was extremely fruitful and lead to spectacular developments. One of the many surprising ideas that emerged was that the particle-like behavior of light was not in contradiction with its well established wave-like nature. It was instead to be understood as part of the same phenomenon, formulated by De Broglie in 1924 as a general wave-particle duality. Of course, what makes this principle powerful is that it applies not only to light but to all kinds of material particles as well. Exploring the quantum world is still an on-going task and a considerable amount of work has been devoted to designing and carrying out experiments that would provide a better understanding of the wave-particle duality. One of the first remarkable success in this direction was the observation in 1927, by Davisson and Germer of diffraction patterns, which are a

clear evidence of wave-like behavior, with electron beams.

After having introduced the concept of wave-particle duality, gaining deeper insight on the quantum nature of light required further theoretical developments. In particular, a first fully quantum theory of the electromagnetic field was proposed by Dirac in 1927 [2] and later improved by Fermi [3]. Nevertheless, these first attempts in defining what would become quantum field theory suffered several flaws, such as seemingly unavoidable diverging quantities. It was only after the second world war with the breakthrough of Schwinger, Feynman and Tomonaga, that a mature theory of quantum electrodynamics was established. It turned out however, that in the field of optics, many effects involving interaction of light with matter, could be explained by quantizing only the matter degrees of freedom and considering light as a classical field. In the introduction of one of the seminal articles that were to lay the foundation of modern quantum optics, Roy Glauber indeed noted [4]:"*It would hardly seem that any justification is necessary for discussing the theory of light quanta in quantum theoretical terms. Yet, as we all know, the successes of classical theory in dealing with optical experiments have been so great that we feel no hesitation in introducing optics as a sophomore course. The quantum theory, in other words, has had only a fraction of the influence upon optics that optics has historically had upon quantum theory.*"

The quantum nature of light gradually came to the forefront when it became possible to perform photocounting experiments with photoelectric detectors. It was realized that the measure of statistical fluctuations in the photon distribution gave access to important information regarding the nature of the field. For example, it was shown that photons in laser light obey a Poissonian distribution, and that any sub-Poissonian distribution, (i.e with smaller fluctuations), could not be explained by a classical theory. The first observation of such sub-Poissonian statistics, also called photon antibunching, was reported by Kimble, Dagenais and Mandel in 1977 [5]. This was considered as the first quantum optical experiment. The term antibunching suggests that photons have a tendency to be emitted one by one rather than in bunches. In other words, the probability of detecting two photons at the same time is smaller in that case than for classical light. How this phenomenon is related to the quantum nature of the field can be understood easily by considering the ideal case of "perfect antibuching", for which the probability of detecting two photons at the same time goes to zero. A perfect antibunching simply means that the light source is emitting *single photons only*, which is of course the most direct evidence of "quantumness". Apart from its important theoretical implications, the efficient emission and manipulation of single photons is also of great practical interest. Indeed, single photons are an invaluable tool to implement

various quantum cryptography and quantum information protocols.

Quantum physics is already very rich at the single particle level, but is even more intriguing in systems composed of many interacting particles. An example of such spectacular many-body effect is the superfluidity of Helium-4. When cooled down below 2 K, the viscosity of liquid Helium vanishes and the fluid starts to flow without friction. This phenomenon, discovered by the Russian physicist Piotr Kapitza in 1937 [6], can be seen as a quantum effect at a macroscopic scale. For Helium-4, the main mechanism behind superfluidity is that of Bose-Einstein condensation (BEC). At low enough temperature, a fraction of the atoms, which, as bosons, obey the Bose-Einstein statistics, condense in the same lowest-energy quantum state. All the atoms of this condensate then behave in exactly the same way, forming a macroscopic quantum object. A related and no less famous manifestation of this kind of "quantum fluid" is superconductivity. In certain materials and under a critical temperature, a sort of condensation mechanism involving pairs of electrons takes place, allowing electric current to flow without any dissipation. Generally speaking, the large number of particles and the crucial role of interactions between them make the study of quantum fluids extremely complex. In fermionic as well as bosonic systems, to understand fully all the different mechanisms behind strong quantum correlations is still one of the biggest challenge of quantum physics. Nevertheless, great progress has been made in the last decades. In particular, the field of quantum fluids gained considerable momentum in the nineties with the experimental realization of a BEC with ultra cold alkali atoms [7, 8]. Since then, cold atoms have been a very efficient platform for manipulating, controlling and testing many-particle quantum systems. In this context, many other promising routes have also been explored and in particular, the question of whether photons could behave like a quantum fluid and exhibit collective behavior was asked. To some extent, this question is pushing the wave-particle duality one step further: light is composed of particles, but could these particles interact with each other? As we shall see throughout this manuscript, going from a fluid composed of material particles like atoms to a photon fluid is not conceptually trivial. The first reason is simply that photons in vacuum do not interact. It is only through the coupling of light to matter degrees of freedom that many-body effects become significant in optical systems. In fact, all the photon-photon interactions discussed in this work are mediated by a nonlinear medium to which light is coupled. In other words, the photons we will consider are not bare photons but photons "dressed" by the interaction with matter. Another non trivial aspect of photonic systems is that photons, unlike atoms, have a finite life time: they are continuously leaking out of the cavities and must be injected into the system by an external

source. As a result, instead of a thermal equilibrium with a well defined number of particles, the system can only reach a steady-state, in which losses are exactly compensated by the external driving. As we shall see shortly, this also has important consequences.

The first studies on photon hydrodynamics were motivated by the close analogy between the Gross-Pitaevskii equation describing atoms in a condensate and the equation of the electromagnetic field in a dielectric nonlinear medium. [9, 10]. Since then, "quantum fluids of light" in various systems and setups have attracted a great deal of interest [11]. Concerning the genesis of this PhD thesis, some of the most influential results were those obtained in semiconductor microcavities. In these structures (which will be described in more details in the next chapter), it is possible, due to the confinement of the electromagnetic field, to reach so strong a coupling between light and matter that the two can no longer be distinguished. They form instead hybrid quasiparticles called polaritons. In the last decade, tremendous experimental progress in creating and controlling polariton fluids in microcavities has been made, which lead to important achievements. In particular, observation of polariton Bose-Einstein condensation was reported in 2006 [12]. Superfluidity of polartions in planar microcavities was predicted in 2004 [13] and observed experimentally for the first time in 2009 [14]. Other aspects of quantum fluids, such as the presence of quantized vortices or other topological excitations has also been investigated [15, 16, 17, 18, 19]. In all these experiments, the observed hydrodynamic behavior resulted from the interactions of a very large number of particles, but interactions between single photons or polaritons remained relatively weak. An important step further in the investigation of quantum many-body effects in photon fluids would be to be able to increase the strength of the interactions and enter the so-called "strongly correlated regime", where the effect of interactions becomes significant as soon as there is more than one particle in the system. To achieve this goal, arrays of nonlinear optical cavities, which are the main focus of this work, are a very promising candidate. As for the photon fluids presented above, there are exciting analogies between photons propagating in an array of cavities and cold atoms moving in an optical lattice. In the latter case, interesting quantum many-body effects, such as the celebrated Mott-insulator-to-superfuid phase transition have already been reported [20] and one of the objective of this PhD thesis was to determine whether a similar phenomenon could be observed with photons. Besides, apart from semiconductor microcavities, such arrays of cavities can also be implemented with superconducting circuits composed of microwave resonators and Josephson junctions [21].

The first chapter of this thesis manuscript is aimed at introducing the theoretical characterization of photon-photon interactions in more quantitive terms. In particular, we will

present the so-called driven-dissipative Bose-Hubbard model describing arrays of nonlinear cavities under an homogenous coherent pumping by an external laser. The last part of Chapter 1 is devoted to a short review of the most recent results in the field.

In Chapter 2, we will explore in more details the analogies between the equilibrium Bose-Hubbard model describing, e.g, atoms in an optical lattice, and its driven-dissipative version. By considering the regime of weak pumping and weak dissipation, we will be able to find the closest equivalent of the Mott-insulator-to-superfluid transition in the driven-dissipative system [22].

In Chapter 3, the results of Chapter 2 are extended to arbitrary pumping and dissipation and the general mean-field phase diagram is presented [23]. In addition, the stability and collective excitations of the different steady-states phases are studied by including fluctuations above the mean-field solution.

In Chapter 4, we address the issue of how to go beyond the mean-field approximation by performing exact numerical simulations on finite-size arrays. In particular, we implement a new method [24], specifically tailored for driven-dissipative systems that enable us to simulate large arrays of cavities.

Chapter 1

General introduction to quantum fluids of light

As we have seen in the introduction, the idea of considering photons as strongly interacting particles is not particularly obvious and needs further clarification. This chapter aims at introducing the key physical notions underlying the concept of effective photon-photon interactions and the subsequent use of effective Hamiltonians to describe them. Equipped with these theoretical tools, we will be able to present and justify the model used throughout this work to describe arrays of nonlinear cavities.

As a gentle introduction to the matter, we will begin with a quick review of a few fundamental concepts of quantum optics such as photons, correlations and coherence. Then, we will move on to the central question of this chapter: how to get photons to interact with each other. We will see that the key mechanism is the coupling of light with matter degrees of freedom. Of course, the phenomenon of light matter-interaction does not belong exclusively to the quantum world. It is indeed already present in the classical theory of dielectric media with nonlinear polarisability: upon elimination of matter degrees of freedom, nonlinear terms arise in the electric field equations. Building up on this consideration, we will begin our introduction to the quantum theory of photon-photon interactions by quantizing the classical equations of nonlinear optics. Applying these results to a single mode in a Fabry-Pérot cavity we will derive the Hamiltonian that will serve as a building block for the studies conducted in this thesis: the quantum Kerr Hamiltonian.

As suggested by the title of this manuscript, we will mainly focus in this thesis on configurations where the effective photon-photon interaction is large enough to enter the strongly correlated regime. Although for the theorist it is only a matter of choosing a numerical parameter, controlling the interaction strength in a real experiment is a considerable challenge.

With current state of the art technologies there are nonetheless prominent candidates for the implementation of strongly-correlated photonic systems [11, 21]. To show that our model is relevant for realistic experimental setups we will derive an effective Kerr Hamiltonian for two of them: quantum wells in semiconducting microcavities and superconducting circuits with Josephson junctions.

We will conclude this chapter by a survey of recent theoretical advances in the field of nonlinear cavity arrays that will give an overview of the scientific context in which this work was conducted.

1.1 Fundamental concepts of quantum optics

This section is a brief introduction to quantum optics. We begin by presenting the concept of photon. In doing so, we shall see that second quantization (or quantum field theory), provides a unified description of light and matter degrees of freedom, which will prove highly valuable in the treatment of light-matter coupling.

1.1.1 Photons

The first requirement for a successful quantum theory of light is obviously to describe the electromagnetic field in a quantum mechanical framework. Generally speaking, "quantumness" is introduced in optics by considering that light beams are composed of many photons which can be absorbed and emitted in various processes. In this simple assertion is contained a crucial property of photons that will guide us towards the right formalism: their number is not conserved. This has obviously important theoretical consequences. In particular, a suitable framework for quantum optics must allow for particle creation and annihilation and be convenient for manipulation of many-particle states.

The standard formulation of quantum mechanics that fulfills all these conditions is called second quantization [25]. The aim of this section is not to provide a comprehensive account of this theoretical framework but to underline that switching from first to second quantization can be seen as essentially the same procedure as quantizing the electromagnetic field.

To put it in a nutshell, second quantization consists in a change of variables. Instead of the particles' coordinates and spin projections, that are usually chosen as arguments of the wave-function, the independent variables are now the occupation numbers of single-particle states. The number of particles in the single-particle state $|\psi\rangle$ is raised by the creation operator and $a^\dagger_{|\psi\rangle}$ and lowered by its Hermitian conjugate $a_{|\psi\rangle}$. The symmetry postulate for many-particle systems is included in the definition of these operators. Indeed, they act in such a way that the resulting (first-quantized) wave function is symmetric for bosons and antisymmetric for fermions. As a result, the symmetry properties of the wave function are transferred to creation and annihilation operators in the form of specific commutation relations that they must obey.

The relation between the two formulations is best seen by considering creation and annihilation operators associated with the position representation. Let us therefore introduce the operator $a^\dagger_{|\mathbf{r}\rangle}$, usually denoted by $\hat{\psi}^\dagger(\mathbf{r})$ that creates a particle at point $\mathbf{r}$. If $\{|\phi_n\rangle\}$ is a basis of the Hilbert space of single-particle states, for example eigenstates of the Hamiltonian, the

operator $\hat{\psi}^\dagger(\mathbf{r})$ can be expressed as:

$$\hat{\psi}^\dagger(\mathbf{r}) = \sum_n \phi_n^*(\mathbf{r}) a^\dagger_{|\phi_n\rangle}, \tag{1.1}$$

where $\phi_n(\mathbf{r})$ is the wave-function of the state $|\phi_n\rangle$ in the position representation. Similarly the Hermitian conjugate, usually called "field operator" may be written as:

$$\hat{\psi}(\mathbf{r}) = \sum_n \phi_n(\mathbf{r}) a_{|\phi_n\rangle}. \tag{1.2}$$

If, in addition, the particles are not interacting, the time-dependence of the field operator (in the Heisenberg picture) is simply:

$$\hat{\psi}(\mathbf{r}, \mathbf{t}) = \sum_n e^{-i\omega_n t} \phi_n(\mathbf{r}) a_{|\phi_n\rangle}, \tag{1.3}$$

where $E_n = \hbar\omega_n$ is the energy of eigenstate $|\phi_n\rangle$. In Eq.(1.3), the motivation behind the choice of notation for the field operator appears clearly. The left-hand side is indeed very similar to the decomposition of the usual wave function $\psi(\mathbf{r})$ on a basis of eigenstates:

$$\psi(\mathbf{r}, \mathbf{t}) = \sum_n e^{-i\omega_n t} \phi_n(\mathbf{r}) \alpha_n, \tag{1.4}$$

with

$$\alpha_n = \langle \phi_n | \psi \rangle. \tag{1.5}$$

The only (crucial) difference is that in Eq.(1.3), the complex amplitude α_n is replaced with a annihilation operator. Looking back at Eqs.(1.3)and (1.4), we see that they actually define a quantization procedure (hence the name "second quantization"). A classical field obeying a wave equation has been promoted to a field operator through its decomposition into orthogonal eigenmodes.

In the light of the above derivation, introducing the photon into the theory will consist in defining properly creation and annihilation operators by quantizing a classical wave equation. For the electromagnetic field, this wave equation stems from Maxwell equations (in the absence of charge and currents):

$$\nabla \cdot \mathbf{B} = 0, \qquad \nabla \times \mathbf{E} = -\frac{\partial \mathbf{B}}{\partial t}, \tag{1.6}$$

$$\nabla \cdot \mathbf{E} = 0, \qquad \nabla \times \mathbf{B} = \frac{1}{c^2}\frac{\partial \mathbf{E}}{\partial t}. \tag{1.7}$$

Due to gauge invariance and partial arbitrariness in the definition of the vector potential, quantization of the electromagnetic field is in general more involved than the procedure outlined above. A complete theory is presented in Ref.[26]. Nevertheless, if we choose an appropriate gauge and assume that the field is contained in a finite volume, the basic ideas presented so far are sufficient. The following treatment is inspired by Ref.[27].

In the context of quantum optics, the best choice is the Coulomb gauge, in which the vector potential is transverse, i.e., fulfills the following condition:

$$\nabla \cdot \mathbf{A}(\mathbf{r}) = 0, \tag{1.8}$$

In the absence of charge, the electric field is also transverse and the scalar potential can be set to $V = 0$. Since in this gauge, both the electric and magnetic fields can be expressed trough the vector potential, we will quantize the latter. The needed wave equation is:

$$\nabla^2 \mathbf{A}(\mathbf{r}, t) - \frac{1}{c^2} \frac{\partial \mathbf{A}(\mathbf{r}, t)}{\partial t} = 0. \tag{1.9}$$

We have seen in Eq.(1.3) that annihilation operators correspond to amplitudes varying in time as $e^{-i\omega t}$ with $\omega > 0$ whereas creation operators are associated with amplitudes varying with negative frequencies. The first step is then to divide the vector potential into two complex fields varying respectively with positive and negative frequencies:

$$\mathbf{A}(\mathbf{r}, t) = \mathbf{A}^{(+)}(\mathbf{r}, t) + \mathbf{A}^{(-)}(\mathbf{r}, t), \tag{1.10}$$

and then to expand $\mathbf{A}^{(+)}(\mathbf{r}, t)$, through a temporal Fourier transform, in terms of a discrete set of orthogonal mode functions:

$$\mathbf{A}^{(+)}(\mathbf{r}, t) = \sum_k \sqrt{\frac{\hbar}{2\omega_k \epsilon_0}} \alpha_k \mathbf{u}_k(\mathbf{r}) e^{-i\omega_k t}, \tag{1.11}$$

where the amplitudes α_k are dimensionless. The mode functions, which depend on the boundary conditions imposed on the field, are also transverse and satisfy the following equation:

$$(\nabla^2 + \frac{\omega_k^2}{c^2}) \mathbf{u}_k(\mathbf{r}) = 0. \tag{1.12}$$

From Eq.(1.11), the quantization procedure is carried on by promoting α_k and α_k^* to mutually adjoint operators:

$$\alpha_k \to a_k, \tag{1.13}$$

$$\alpha_k^* \to a_k^\dagger. \tag{1.14}$$

Since photons are bosonic particles, these operators must satisfy the following commutation relations:

$$[a_k, a_{k'}] = [a_k^\dagger, a_{k'}^\dagger] = 0, \tag{1.15}$$

$$[a_k, a_{k'}^\dagger] = \delta_{kk'}. \tag{1.16}$$

The quantum expression for the vector potential of a free field in the Heisenberg picture is then:

$$\mathbf{A}(\mathbf{r},t) = \sum_k \sqrt{\frac{\hbar}{2\omega_k \epsilon_0}} (a_k \mathbf{u}_k(\mathbf{r}) e^{-i\omega_k t} + a_k^\dagger \mathbf{u}_k^*(\mathbf{r}) e^{i\omega_k t}), \tag{1.17}$$

and the electric field is expressed as:

$$\mathbf{E}(\mathbf{r},t) = i \sum_k \sqrt{\frac{\hbar\omega_k}{2\epsilon_0}} (a_k \mathbf{u}_k(\mathbf{r}) e^{-i\omega_k t} - a_k^\dagger \mathbf{u}_k^*(\mathbf{r}) e^{i\omega_k t}). \tag{1.18}$$

It is noteworthy that the complex fields $\mathbf{E}^{(+)}(\mathbf{r},t)$ and $\mathbf{E}^{(-)}(\mathbf{r},t)$, which are defined in the same way as $\mathbf{A}^{(+)}(\mathbf{r},t)$ and $\mathbf{A}^{(-)}(\mathbf{r},t)$ in Eq.(1.10), are mathematical objects without precise physical meaning in classical electrodynamics, whereas in the quantum theory, they are associated with distinct physical processes, namely absorption and emission of photons [4]. As such, as we shall see in the following, they play an important role in the theory of photodetection.

The quantization scheme presented above is consistent with the more general procedure of canonical quantization. The latter is based on the Hamiltonian formalism for classical fields. In the case of the electromagnetic field, the dynamical variables are the $A_i(\mathbf{r},t)$ and their conjugate momentum $\Pi_i(\mathbf{r},t) = -\epsilon_0 E_i(\mathbf{r},t)$. Quantization is performed by associating to these variables operators that obey the following commutation relations:

$$[A_i(\mathbf{r},t), \Pi_j(\mathbf{r}',t')] = i\hbar \delta_{ij}^{(tr)}(\mathbf{r}-\mathbf{r}'), \tag{1.19}$$

where we have introduced the so-called "transverse delta function", which has the same effect on transverse fields as the usual delta function but is compatible with the gauge condition and Gauss law. It is a distribution defined by [28]:

$$\delta_{ij}^{(tr)}(\mathbf{r}) = \int \frac{\mathrm{d}^3 k}{(2\pi)^3} e^{i\mathbf{k}\cdot\mathbf{r}} (\delta_{ij} - \frac{k_i k_j}{k^2}). \tag{1.20}$$

The quantum Hamiltonian for the free electromagnetic field is then:

$$H = \int \mathrm{d}^3 r (\frac{1}{2}\epsilon_0 E^2 + \frac{1}{2\mu_0} B^2). \tag{1.21}$$

Writing this Hamiltonian in terms of creation and annihilation operators, we recover the usual picture of the free electromagnetic field as an infinite collection of harmonic oscillators:

$$H = \sum_k \hbar\omega_k (a_k^\dagger a_k + \frac{1}{2}). \tag{1.22}$$

For a more thorough treatment of quantum electrodynamics in the Coulomb gauge the reader may consult Ref.[28].

1.1.2 Field correlation functions

The next step, after quantizing the electromagnetic field, is to describe, in a purely quantum framework, the outcome of experiments that reveal the quantum nature of the field. One way to study quantum properties of light is to perform photon counting experiments with one or several detectors. In such experiments, photons are usually absorbed by an electronic medium. Regardless of the microscopic details of the photoabsorption process, the matrix element for a transition of the field from a state $|i\rangle$ to a state $|f\rangle$, in which one photon is absorbed, is:

$$\langle f|E^{(+)}(\mathbf{r},t)|i\rangle. \tag{1.23}$$

In this expression we have neglected the vectorial character of the field by assuming only one photon polarization.

Following one of Glauber's seminal papers [4], we define a perfect photodetector as a device of negligible size, for which the probability of absorbing a photon is proportional to the sum over all final states of the squared absolute values of Eq.(1.23):

$$p \propto \sum_f |\langle f|E^{(+)}(\mathbf{r},t)|i\rangle|^2 = \langle i|E^{(-)}(\mathbf{r},t)E^{(+)}(\mathbf{r},t)|i\rangle. \tag{1.24}$$

Similarly, in an experiment like the one first performed by Hanbury Brown and Twiss [29], which measures delayed photon coincidences using two detectors, the probability of detecting a photon in $\mathbf{r}$ at t and another one at $\mathbf{r}'$ at t' is:

$$p_{coincid.} \propto \langle i|E^{(-)}(\mathbf{r},t)E^{(-)}(\mathbf{r}',t')E^{(+)}(\mathbf{r}',t')E^{(+)}(\mathbf{r},t)|i\rangle. \tag{1.25}$$

This can be extended to the case where the initial state of the field is not known with certainty by defining:

$$\langle E^{(-)}(\mathbf{r},t)E^{(-)}(\mathbf{r}',t')E^{(+)}(\mathbf{r}',t')E^{(+)}(\mathbf{r},t)\rangle = \mathrm{T}r[\rho E^{(-)}(\mathbf{r},t)E^{(-)}(\mathbf{r}',t')E^{(+)}(\mathbf{r}',t')E^{(+)}(\mathbf{r},t)], \tag{1.26}$$

where ρ is the field density matrix. Note that for a stationary field, this quantity depends only on the time delay $\tau = t' - t$.

Equation (1.26) is a particular example of field correlation functions that we can use to describe quantitatively the properties of light. A general definition for the n^{th}-order correlation function is:

$$G^{(n)}(x_1, \ldots, x_{2n}) = \langle E^{(-)}(x_1) \ldots E^{(-)}(x_n) E^{(+)}(x_{n+1}) \ldots E^{(+)}(x_{2n}) \rangle, \tag{1.27}$$

where $x_i = (\mathbf{r}_i, t_i)$. It is often more judicious to deal with normalized correlation functions, defined as:

$$g^{(n)}(x_1, \ldots, x_{2n}) = \frac{G^{(n)}(x_1, \ldots, x_{2n})}{\prod_{i=1}^{2n} \sqrt{G^{(1)}(x_i, x_i)}}. \tag{1.28}$$

In this thesis, we will be mostly interested by electromagnetic modes confined in optical cavities, and will focus on two correlation functions. The first one is the single-mode version of $G^{(1)}(x_i, x_i)$, namely:

$$n = \langle a^\dagger a \rangle. \tag{1.29}$$

This is simply the mean photon number. The other quantity of interest is the zero-delay second order correlation function:

$$g^{(2)}(\tau = 0) = \frac{\langle a^\dagger a^\dagger a a \rangle}{\langle a^\dagger a \rangle^2}. \tag{1.30}$$

As seen in Eq.(1.25), this quantity is related to the probability of detecting two photons at the same time. It provides valuable information on the photon distribution function. Expressed in term of the mean photon number n and its variance, $g^{(2)}(0)$ reads:

$$g^{(2)}(0) = 1 + \frac{V - n}{n^2}, \tag{1.31}$$

with $V = \langle (a^\dagger a)^2 \rangle - \langle a^\dagger a \rangle^2$. This shows that a Poissonian statistics for the photon distribution, as it is the case with laser light, corresponds to $g^{(2)}(0) = 1$. For a Fock state $|n\rangle$ with n photons, there is no fluctuation in the number of photons and we have:

$$g^{(2)}(0) = 1 - \frac{1}{n} < 1, \tag{1.32}$$

so that the statistics is sub-Poissonian. The inequality $g^{(2)}(0) < 1$ also implies photon antibunching. This phenomenon, cannot be explained outside of a quantum theory of light, since a classical theory always predicts $g^{(2)}(0) \geq 1$. This correlation function is therefore

a useful tool for identifying "quantumness". In particular, $g^{(2)}(0) = 0$ is obtained for the most quantum of states, that is a single-photon Fock state, with a density matrix $\rho = |1\rangle\langle 1|$. In this case, it is impossible to detect two photons at the same time, there is a perfect antibunching of photons. In this thesis, we shall also encounter the phenomenon of photon bunching, associated with $g^{(2)}(0) > 1$. It is not however, a purely quantum feature, since thermal light also shows a super-Poissonian photon distribution with $g^{(2)}(0) = 2$.

The definition of Eq.(1.28), introduced by Glauber, allowed him to give a precise meaning to the idea of optical coherence. First order coherence is, e.g., the quantity associated with the production of interference fringes in an experiment where two modes are superposed and detected with a single device. However, field showing such interference patterns may lack higher-order coherence in the sense of Eq.(1.28). He called "fully coherent" a state which satisfies $g^{(n)}(x_1, \ldots, x_{2n}) = 1$, for every $n \in \mathbb{N}^*$. A sufficient condition for a pure state $|\psi\rangle$ to be fully coherent is that there exists a function $\mathcal{E}^{(+)}(\mathbf{r}, t)$ such that:

$$E^{(+)}(\mathbf{r}, t)|\psi\rangle = \mathcal{E}^{(+)}(\mathbf{r}, t)|\psi\rangle. \tag{1.33}$$

States $|\alpha\rangle$ that satisfy Eq.(1.33) for a single mode a:

$$a|\alpha\rangle = \alpha|\alpha\rangle, \tag{1.34}$$

are called coherent states. As they will play a crucial role in Chapter 3, we recall some of their basic properties in the next subsection.

1.1.3 Coherent states

Coherent states have a wide range of applications in quantum physics, going well beyond the subject of quantum optics [30]. These states were first introduced by Schrödinger [31] as states for which expectation values are classical sinusoidal solutions of a one-dimensional harmonic oscillator. In this sense they can be considered as the closest to classical states.

From Eq.(1.34), we can determine their expansion in Fock space:

$$|\alpha\rangle = e^{-|\alpha|^2/2} \sum_n \frac{\alpha^n}{\sqrt{n!}} |n\rangle. \tag{1.35}$$

Hence, coherent states appear as an infinite superposition of number states $|n\rangle$ which is left unmodified (up to a complex factor) under the action of the operator annihilating a elementary quantum.

One of the most important properties of coherent states is that they form an overcomplete basis. In other words, one can write a resolution of identity in terms of coherent states:

$$\frac{1}{\pi}\int |\alpha\rangle\langle\alpha| \mathrm{d}^2\alpha = I_d, \tag{1.36}$$

but the states are not orthogonal:

$$\langle\alpha|\beta\rangle = e^{-\frac{1}{2}|\alpha-\beta|^2} e^{\alpha\beta^*}. \tag{1.37}$$

An important consequence of Eq.(1.36) is that it is possible to write coherent state representations of operators and density matrices. This idea will be developed further in Chapter 3. For now, let us conclude this section by stating another useful properties of coherent states: the expectation value, in a coherent state, of any normally ordered second-quantized operator $H(a^\dagger, a)$ is given by

$$\langle\alpha|H(a^\dagger, a)|\alpha\rangle = H(\alpha^*, \alpha). \tag{1.38}$$

This equation is at the basis of the semiclassical (or Gross-Pitaevskii) approximation, in which second-quantized operators are replaced with complex numbers.

1.2 Effective photon-photon interactions

It is well known that the typical cross-section of photon-photon interactions in vacuum is too small to play any significant role in realistic optical experiments. Effective interactions between photons are therefore mediated by the coupling of light with matter. In this thesis we will be interested in coupling a nonlinear medium with a single mode of the electromagnetic field confined in an optical cavity. Such nonlinear cavities can then be coupled together to form a lattice on which photons will propagate.

There are various ways to create a nonlinear medium and the microscopic model of the nonlinear cavity depends in general on the particular medium that is used. To remain as general as possible in our description, we will focus on an effective Hamiltonian whose interest is threefold: it is conceptually simple, it bears strong similarities with models for material particles and it is sufficient to capture the essential features of many experimental setups.

In this effective model, photon-photon interaction is included as a two-body interaction term (Kerr nonlinearity). The Hamiltonian for the cavity mode is then:

$$H_{\mathrm{Kerr}} = \hbar\omega_c b^\dagger b + \frac{U}{2} b^\dagger b^\dagger b b. \tag{1.39}$$

In the following we show how this Hamiltonian arises naturally in different contexts such as the macroscopic theory of nonlinear optics, semiconductor nanostructures or superconducting circuits. We conclude this section by presenting how to include an external driving field as well as cavity losses in the description of the system.

1.2.1 Quantization of macroscopic nonlinear optics

The idea that light-matter coupling may induce effective interactions between light beams is not specifically quantum and is already present in the classical theory of electrodynamics. At this level of description, interaction of light with matter in a dielectric medium is taken into account through the polarization $\mathbf{P}$ whose components are given by:

$$P_i = \epsilon_0[\chi^{(1)}_{ij}E_j + \chi^{(2)}_{ijk}E_jE_k + \chi^{(3)}_{ijkl}E_jE_kE_l + ...], \tag{1.40}$$

and the following Maxwell equations:

$$\nabla \cdot \mathbf{B} = 0, \qquad \nabla \times \mathbf{E} = -\frac{\partial \mathbf{B}}{\partial t}, \tag{1.41}$$

$$\nabla \cdot \mathbf{D} = 0, \qquad \nabla \times \mathbf{B} = \mu_0 \frac{\partial \mathbf{D}}{\partial t}, \tag{1.42}$$

where $\mathbf{D} = \epsilon_0\mathbf{E} + \mathbf{P}$ is the displacement vector. A possible approach to the quantum theory of nonlinear optics is to use the procedure of the previous section and quantize these equations [32, 33]. For simplicity we will first treat the case of a nondispersive homogeneous medium. The way to proceed is to find the Hamiltonian and impose on canonical variables commutation relations similar to Eq.(1.19). The Hamiltonian is most easily found by writing an appropriate Lagrangian density, which in the present case is:

$$\mathcal{L} = \epsilon_0[\frac{1}{2}(E^2 - c^2B^2) + \frac{1}{2}\chi^{(1)}_{ij}E_iE_j + \frac{1}{3}\chi^{(2)}_{ijk}E_iE_jE_k + \frac{1}{4}\chi^{(3)}_{ijkl}E_iE_jE_kE_l]. \tag{1.43}$$

The conjugate momentum to the vector potential's components are then given by:

$$\Pi_0 = \frac{\delta\mathcal{L}}{\delta(\partial_0 A_0)} = 0, \quad \Pi_i = \frac{\delta\mathcal{L}}{\delta(\partial_i A_i)} = -D_i. \tag{1.44}$$

Applying to $\mathcal{L}$ a Legendre transform yields the following Hamiltonian:

$$H = \int \mathrm{d}^3r\epsilon_0[\frac{1}{2}(E^2 + c^2B^2) + \frac{1}{2}\chi^{(1)}_{ij}E_iE_j + \frac{2}{3}\chi^{(2)}_{ijk}E_iE_jE_k + \frac{3}{4}\chi^{(3)}_{ijkl}E_iE_jE_kE_l] \tag{1.45}$$

$$+ \int \mathrm{d}^3r\mathbf{D}\cdot\nabla A_0 \tag{1.46}$$

The last term may be eliminated by performing an integration by part and using the condition $\nabla \cdot \mathbf{D} = 0$. Since E_i is no longer a canonical momentum, it is more convenient to rewrite H as a function of D_i. This yields:

$$H = \int \mathrm{d}^3 r \frac{1}{2\mu_0} B^2 + \frac{1}{2}\beta_{ij}^{(1)} D_i Dj + \frac{1}{3}\beta_{ijk}^{(2)} D_i D_j D_k + \frac{1}{4}\beta_{ijkl}^{(3)} D_i D_j D_k D_l, \tag{1.47}$$

Where we have introduced the tensors $\beta^{(j)}$ through which we express $\mathbf{E}$ as a function of $\mathbf{D}$:

$$\beta^{(1)} = [\epsilon_0(1+\chi^{(1)})]^{-1}, \tag{1.48}$$

$$\beta_{imn}^{(2)} = -\epsilon_0 \beta_{ij}^{(1)} \beta_{km}^{(1)} \beta_{ln}^{(1)} \chi_{jkl}^{(2)}, \tag{1.49}$$

$$\beta_{imnp}^{(3)} = -\epsilon_0 \beta_{ij}^{(1)} \beta_{km}^{(1)} \beta_{ln}^{(1)} \beta_{qp}^{(1)} \chi_{jklq}^{(3)}, \tag{1.50}$$

Quantization now consists in imposing the following commutation relations:

$$[A_i(\mathbf{r},t), -D_j(\mathbf{r}',t')] = i\hbar \delta_{ij}^{(tr)}(\mathbf{r}-\mathbf{r}'). \tag{1.51}$$

As we did for the free field in the previous section we can introduce annihilation and creation operators by decomposing the field in orthogonal modes. The annihilation operator corresponding to a mode function $\mathbf{u}_k(\mathbf{r})$ reads:

$$a_k(t) = \int \mathrm{d}^3 r \frac{1}{\sqrt{\hbar}} \mathbf{u}^*(\mathbf{r}) \cdot [\sqrt{\frac{\epsilon_0 \omega_k}{2}} \mathbf{A}(\mathbf{r},\mathbf{t}) - \frac{i}{\sqrt{2\epsilon_0 \omega_k}} \mathbf{D}(\mathbf{r},t)]. \tag{1.52}$$

From this last expression we see that the annihilation operator now contains matter degrees of freedom through its dependence on $\mathbf{D}$. We are therefore in presence of a "dressed" photon, a kind of hybrid light-matter excitation. We will encounter another type of hybrid light-matter excitation in the next subsection on a more microscopic level.

Let us conclude this discussion on macroscopic nonlinear optics by showing how the Kerr Hamiltonian Eq.(1.39) for an optical cavity may be derived from Eq.(1.47). First, it will be possible in a medium with $\chi^{(3)}$ nonlinearity when the effect of $\chi^{(2)}$ may be neglected (e.g., in the absence of phase matching). Then if the modes frequency spacing is large relative to the nonlinear frequency shift, a single mode approximation is appropriate and the field $\mathbf{D}$ can be written as:

$$\mathbf{D}(\mathbf{r},t) = i\sqrt{\frac{\hbar\omega_c \epsilon_0}{2}} [\mathbf{u}(\mathbf{r}) b(t) - b^\dagger(t) \mathbf{u}^*(\mathbf{r})]. \tag{1.53}$$

Besides, we will consider an homogeneous and isotropic medium, for which the general tensor $\beta_{imnp}^{(3)}$ is diagonal and defined by a single scalar $\beta^{(3)}$. Finally, we can perform the so-called rotating wave approximation, and neglect in the Hamiltonian all nonresonant terms

that generate in the Heisenberg equations of motions rapidly oscillating terms, whose effect average to zero. Under such circumstances, we find a Kerr Hamiltonian similar to Eq.(1.39) by injecting Eq.(1.53) into Eq.(1.47). The nonlinear coefficient is then given by:

$$U = \frac{3}{4}\beta^{(3)}(\hbar\omega_c\epsilon_0)^2 \int \mathrm{d}^3 r |\mathbf{u}(\mathbf{r})|^4. \tag{1.54}$$

The above results are valid for a nondispersive homogeneous medium. A complete theory, taking into account inhomogeneity and dispersion is presented in Ref.[34]. It is based on quantization of the dual potential $\mathbf{\Lambda}(\mathbf{r}, t)$ instead of the usual vector potential. The existence of this potential is guarantied by Gauss law $\nabla \cdot \mathbf{D} = 0$ and defined as:

$$\mathbf{D} = \nabla \times \mathbf{\Lambda}, \tag{1.55}$$

$$\mathbf{B} = \mu_0[\frac{\partial}{\partial t} + \nabla\Lambda_0]. \tag{1.56}$$

Although the two quantization methods are equivalent, the use of the dual potential makes all calculations much more straightforward.

Dressed photons are expected to be strongly correlated if the interaction strength U is much larger that the width of the cavity mode, $\hbar\gamma$. Interaction between dressed photons in bulk materials with $\chi^{(3)}$ nonlinearity is usually too small to have $U/(\hbar\gamma) \gg 1$. The nonlinearity can be significantly higher in systems where the interaction between light and matter enters the so-called "strong coupling regime". This regime, where the coupling strength is much larger that the photon loss rate can be achieved in a variety of systems such as atomic gases [35, 36], semiconductor nanostructures [37, 38] and superconducting circuits [39, 40, 21]. In the following we will present two of the most promising candidates for the implementation of cavity arrays with strong nonlinearities: semiconductor quantum wells embedded in microcavities and superconducting circuits with nonlinear resonators based on Josephson junctions. We will see that in both cases it is possible to describe the system with an effective Kerr Hamiltonian similar to Eq.(1.39).

1.2.2 Exciton-polaritons in a photonic box

A quantum well is an heterostructure formed by layers of two types of semiconductors, each with a different band gap. The well itself is a thin central layer of the first semiconductor (a few nanometers), which is surrounded by two layers of the other semiconductor that acts as a "barrier material". The materials are chosen such that both electrons and holes are confined

inside the well: the bottom of the well's conduction band is at a lower energy than in the surrounding material and the bottom of its valence band at a higher energy (see Fig.(1.1)). The motion of carriers being confined in the plane of the well, a quantum well is essentially a two-dimensional structure.

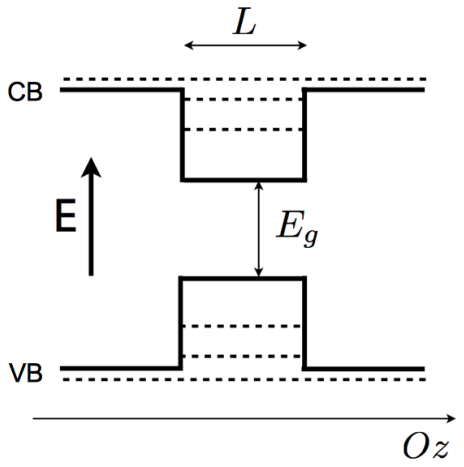

Figure 1.1: Energy of quantum states confined in a quantum well as a function of the position along the growth direction Oz. VB is the valence band and CB the conduction band. Dashed lines represent energy levels. E_g denotes the energy gap and L the width of the well.

Due to Coulomb interaction, a hole of the valence band and an electron of the conduction band can form an hydrogen-like bound state called "exciton". The creation of such (quasi)-bosonic excitation corresponds to the lowest energy optical transition of the quantum well.

The coupling between excitons and photons is enhanced by embedding one or more quantum wells in a Fabry-Pérot cavity with semiconducting Bragg mirrors. The cavity mode is usually tuned to be quasi-resonant with the exciton frequency and quantum wells placed at antinodes of the cavity electromagnetic field. Such two-dimensional planar cavities have proved extremely useful for the investigation of hydrodynamical effects in optical systems [11]. However, making cavities described by a single-mode hamiltonian such as Eq.(1.39) requires further confinement of exciton and photons. To do so, several strategies are available [41]. Zero-dimensional cavities or "photonic boxes" have been obtained by locally changing the thickness of the cavity layer [42], as shown on the top panel of Fig.(1.2). Confinement in the 3 dimensions has also been achieved by deep etching of the cavity layer, so as to design a micropillar with a lateral dimension of a few microns (see bottom panel of Fig.(1.2)). In such a structure a strong lateral confinement is induced by the large refractive index difference

between air and semiconductors.

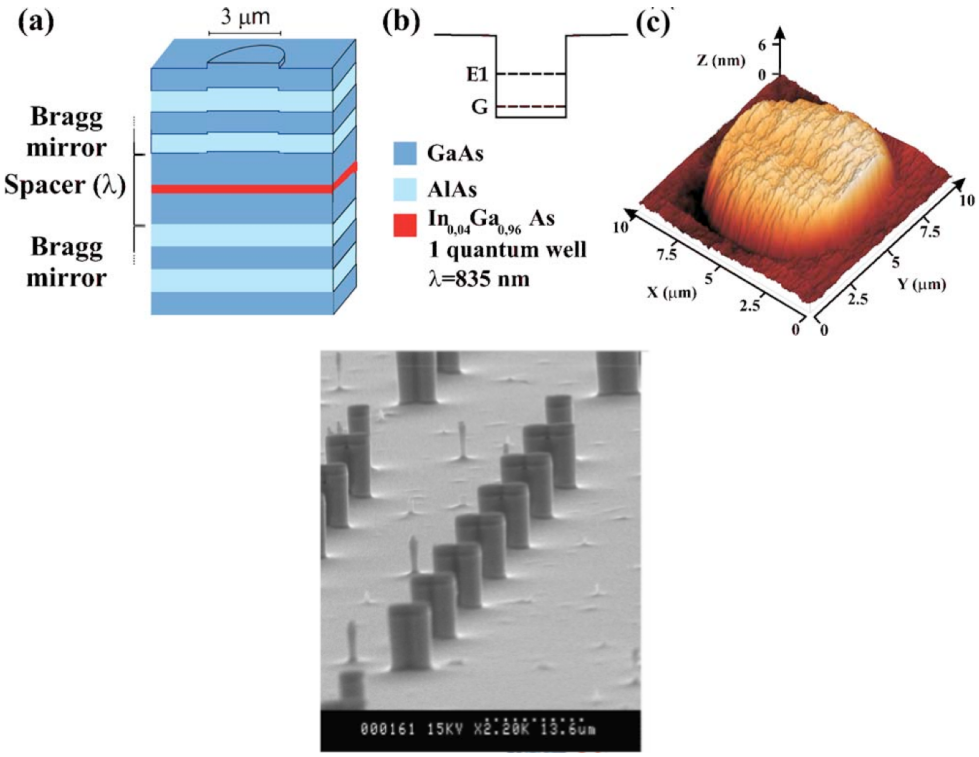

Figure 1.2: Top panels: photonic box from a microcavity with position-dependent thickness. (a) Scheme of a cavity with circular mesa etched on the spacer layer. (b) Scheme of the potential trap with two confined levels. (c) AFM image of a 9-μm-diameter circular mesa on the surface of the top mirror [42]. Bottom panel: coupled micropillars designed at Laboratoire de Photonique et Nanostructures in Marcoussis (France).

If the confinement is sufficiently strong, the energy spacing between confined modes of the field is much larger that the mode spectral width. It can also be much larger than the detuning between the pump and the excitonic frequency. Under such circumstances, it is safe to consider only a single photonic mode and a single excitonic level [43]. The Hamiltonian (without external driving) then reads:

$$H_{exc-ph} = \hbar\omega_X d^\dagger d + \hbar\omega_C a^\dagger a + \hbar\Omega_R (d^\dagger a + a^\dagger d) + \frac{\hbar\omega_{nl}}{2} d^\dagger d^\dagger dd, \tag{1.57}$$

where $\hbar\omega_X$ is the exciton energy, $\hbar\omega_C$ the photon energy, $\hbar\Omega_R$ the coupling constant (Rabi energy) and $\hbar\omega_{nl}$ the exciton-exciton interaction. The operator $a^\dagger$ creates a photon in the cavity mode and $d^\dagger$ an exciton.

To begin with, let us first consider the quadratic part of the Hamiltonian: $\hbar\omega_X d^\dagger d + \hbar\omega_C a^\dagger a + \hbar\Omega_R(d^\dagger a + a^\dagger d)$.
It can be readily diagonalized by performing a unitary transformation on the operators $a^\dagger$ and $d^\dagger$. The new operators create and annihilate hybrid ligh-matter bosonic quasiparticles called exciton-polaritons. This polaritonic creation and destruction operators are given by:

$$\begin{pmatrix} p_1^\dagger \\ p_2^\dagger \end{pmatrix} = \begin{pmatrix} X & C \\ -C & X \end{pmatrix} \begin{pmatrix} d^\dagger \\ a^\dagger \end{pmatrix}. \tag{1.58}$$

The coefficients X and C are respectively the polariton excitonic and photonic ampltudes. They obey a normalization condition: $X^2 + C^2 = 1$.

The polaritonic modes have frequencies

$$\omega_\pm = \frac{\omega_X + \omega_C}{2} \pm \sqrt{\Omega_R + (\frac{\omega_X - \omega_C}{2})^2}. \tag{1.59}$$

The lowest of these frequencies is denoted by ω_{LP} and corresponds to the lower polariton branch. With these notations, excitonic and photonic amplitudes read:

$$C = -\frac{1}{\sqrt{1 + (\frac{\omega_{\mathrm{LP}} - \omega_C}{\Omega_R})^2}} \ , \ X = \frac{1}{\sqrt{1 + (\frac{\Omega_R}{\omega_{\mathrm{LP}} - \omega_C})^2}}. \tag{1.60}$$

Before rewriting the Hamiltonian of Eq.(1.57) as a function of polaritonic operators, a useful simplification may be introduced if the laser frequency is chosen to be quasi-resonant with the lower polariton branch: one can neglect the effect of the upper branch and discard all terms containing p_2 and $p_2^\dagger$. The Hamiltonian then reads:

$$H_{exc-ph} = \hbar\omega_{\mathrm{LP}} p_1^\dagger p_1 + \frac{\hbar\omega_{nl}}{2} X^4 p_1^\dagger p_1^\dagger p_1 p_1. \tag{1.61}$$

We see that this Hamiltonian is once again similar to Eq.(1.39). This is another example, treated at a more microscopic level, of effective interactions between dressed photons induced by the coupling of light to a nonlinear medium.

1.2.3 Example of nonlinear resonators in circuit QED

Other very promising candidates for the experimental implementation of cavity arrays with large nonlinearities come from the relatively young, but prominent field of circuit quantum electrodynamics (circuit QED). The nonlinear elements are this time superconducting circuits with Josephson junctions and the role of the Fabry-Pérot cavity is played by microwave

transmission line resonators. Since one of the major focus of the field is quantum information processing, the nonlinear elements considered in most of the literature are two-level systems (qubits). From a theoretical point of view, the interaction of such qubits with microwave photons is well described by the Jaynes-Cummings model. This model does share some similarities with the Kerr Hamiltonian that will be discussed in the next subsection. For now, let us take a different route and focus on a circuit that is actually modeled by a Kerr nonlinearity.

The superconducting circuits used in circuit QED are macroscopic objects, with a size ranging from a hundred of microns to a few millimeters, and that behave quantum mechanically. Macroscopic variables such as currents or voltages are still the relevant degrees of freedom, but they are described by noncommuting operators. The general procedure employed to derive Hamitonians for these circuits follows the rules of canonical quantization and is therefore not very different from the one outlined earlier in this chapter. In particular the mains steps remain the same: first, one must write an appropriate Lagrangian for the classical circuit, the corresponding classical Hamiltonian is then obtained by means of a Legendre transform. Finally, quantization is achieved by imposing canonical commutation relations to conjugate dynamical variables. Following Girvin [44], we first illustrate these rules on the circuit with the simplest dynamics: the LC resonator.

Basics in circuit quantization: The LC resonator

A natural choice of dynamical variables for a LC oscillator is the charge q accumulated on the capacitor by the current I flowing through the circuit. The Lagrangian is then:

$$\mathcal{L} = \frac{1}{2}L\dot{q}^2 - \frac{1}{2C}q^2. \tag{1.62}$$

In this description the "kinetic part" is represented by the inductor while the "potential energy" is stored in the capacitor. For a reason that will become clear later when we include nonlinear elements in the circuit, it is more convenient to adopt an alternative point of view and choose the node flux ϕ as a "position" variable. It is defined as follows:

$$\phi(t) = \int_{t_0}^{t} V(t')\mathrm{d}t', \tag{1.63}$$

where

$$V = -\frac{q}{C}, \tag{1.64}$$

is the voltage at the node connecting the inductor and the capacitor and t_0 a fixed reference time. The relation:

$$V = L\dot{I} = \dot{\phi}, \tag{1.65}$$

show that ϕ is the magnetic flux winding through the inductor (in the absence of external flux). With this choice of variables, the Lagrangian now reads:

$$\mathcal{L} = \frac{1}{2}C\dot{\phi}^2 - \frac{1}{2L}\phi^2. \tag{1.66}$$

Equipped with this Lagrangian, we can move on to the second step of our quantization procedure and write the corresponding Hamiltonian. The momentum conjugate to the flux is:

$$Q = \frac{\delta\mathcal{L}}{\delta\dot{\phi}} = C\dot{\phi}, \tag{1.67}$$

which gives for the Hamiltonian:

$$\mathcal{H} = \frac{1}{2C}Q^2 + \frac{1}{2L}\phi^2. \tag{1.68}$$

According to the last step, we have to impose the canonical commutation rule:

$$[\phi, Q] = i\hbar. \tag{1.69}$$

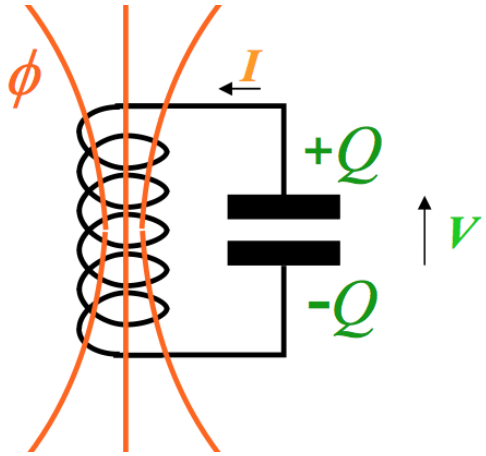

Figure 1.3: Scheme of a LC resonator with variables ϕ, V and Q as defined in the main text. From Ref.[45]

A nonlinear resonator

Capacitor and inductors are basic linear elements of a circuit. In particular, transmission lines can be modeled by a chain of capacitors and inductors. As for nonlinear elements, their building block is the Josephson junction. Such a junction is formed by two superconductors separated by a thin layer of insulating material. It can be shown that under appropriate conditions, the Cooper pairs of the superconductors can tunnel through the insulating barrier without dissipation. Inserted in a circuit the Josephson junction acts as a nonlinear inductor governed by the two celebrated Josephson equations:

$$I = I_0 \sin\delta, \tag{1.70}$$

$$\frac{\mathrm{d}\delta}{\mathrm{dt}} = \frac{V}{\phi_0} = V\frac{2e}{\hbar}, \tag{1.71}$$

with δ the difference between the phases of the two superconductors order parameter, V the voltage applied to the junction and I_0 a critical intensity depending on the superconductor energy gap and on the resistance of the junction. We have also introduced the flux quantum $\phi_0 = \hbar/2e$.

Note that if we choose the set of variables defined in Eq.(1.62), where the "kinetic part" is represented by inductors and the "potential energy" by capacitors, the inclusion of a Josephson junction in the circuit would result in non-quadratic kinetic terms. Introducing the flux variable as in Eq.(1.63) in order to avoid this complication, we find that the intensity can be rewritten as:

$$I = I_0 \sin(\frac{\phi}{\phi_0}). \tag{1.72}$$

The nonlinear inductance of the junction is characterized by

$$L_J = \left(\frac{\mathrm{d}I}{\mathrm{d}\phi}\right)^{-1} = \frac{L_{J0}}{\cos(\frac{\phi}{\phi_0})}, \tag{1.73}$$

where L_{J0} is the effective linear inductance of the junction, $L_{J0} = \phi_0/I_0$. Finally, in view of writing a Lagrangian for circuits containing Josephson junctions, we can compute the energy stored in the junction, $E(t) = \int_{-\infty}^{t} I(t')V(t')\mathrm{d}t'$, and find:

$$E(t) = -E_J \cos(\frac{\phi}{\phi_0}), \tag{1.74}$$

with $E_J = I_0\phi_0$.

The method of circuit quantization presented above can now be extended to more complex circuits with n different nodes, with a Lagrangian $\mathcal{L}(\phi_1, \phi_n, \ldots, \dot{\phi}_1, \ldots, \dot{\phi}_n)$ depending on flux variables in the n nodes. The Lagrangian can be cast in the form $\mathcal{L} = T - V$ where T contains the "kinetic energy" stemming from capacitors and V the "potential energy" that comes from inductors and Josephson junctions. The contribution of each type of element connecting the nodes n and $n+1$ has the form:

$$T_{\text{capacitor}} = \frac{C}{2}(\dot{\phi}_{n+1} - \dot{\phi}_{n+1})^2, \tag{1.75}$$

$$V_{\text{inductor}} = \frac{1}{2L}(\phi_{n+1} - \phi_n)^2, \tag{1.76}$$

$$V_{\text{JJ}} = -E_J \cos\left(\frac{(\phi_{n+1} - \phi_n)}{\phi_0}\right). \tag{1.77}$$

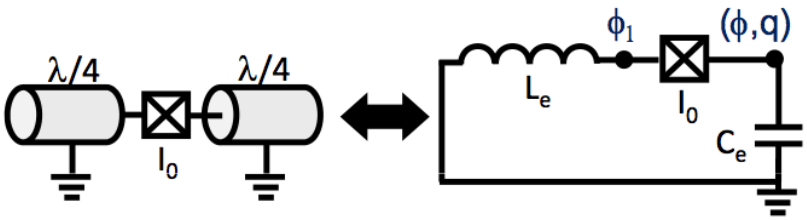

Figure 1.4: Scheme of a series combination of an inductor, capacitor and Josephson junction, and of its equivalent implementation with distributed elements (such as transmission lines). From Ref.[46]

Let us now consider, as in Ref.[46], a series combination of a Josephson junction placed between a capacitor and an inductor. Let ϕ_1 denote the flux at the node connecting the inductor and the junction and ϕ the flux at the node connection the junction and the capacitor. The third node being connected to the ground has zero flux and does not play any role.

The Hamiltonian of this circuit is given by:

$$H = \frac{\phi_1^2}{2L} - E_J \cos(\frac{\phi - \phi_1}{\phi_0}) + \frac{q^2}{2C}, \tag{1.78}$$

where q is the momentum conjugate to ϕ. Since the current I flowing through the inductor and the junction is the same, ϕ and ϕ_1 are not independent and must obey the following equation:

$$I = \frac{\phi_1}{L} = I_0 \sin(\frac{\phi - \phi_1}{\phi_0}). \tag{1.79}$$

This in turn defines a implicit relation between ϕ_1 and ϕ, $\phi_1 = g(\phi)$. Injecting this last expression into the Hamiltonian and expanding it in powers of ϕ up to fourth order, we find:

$$H = \frac{\phi^2}{2L_t} + \frac{q^2}{2C_e} - \frac{1}{24}\frac{L_{J0}^3}{L_t^4\phi_0^2}\phi^4, \tag{1.80}$$

with L_t the total inductance $L_t = L_{J0} + L_e$. Introducing now the creation and destruction operators associated with ϕ and q:

$$\phi = i\sqrt{\frac{\hbar Z_e}{2}}(a - a^\dagger), \tag{1.81}$$

$$q = \sqrt{\frac{\hbar}{2Z_e}}(a + a^\dagger), \tag{1.82}$$

where the impedance $Z_e = \sqrt{L_t/C_e}$, and keeping only the resonant terms, we get the Kerr Hamiltonian:

$$H = \hbar\omega_0 a^\dagger a + \frac{U}{2}a^\dagger a^\dagger a a, \tag{1.83}$$

with

$$U = -\frac{e^2\omega_0 Z_e}{2}\left(\frac{L_{J0}}{L_t}\right)^3, \tag{1.84}$$

and $\omega_0 = 1/\sqrt{L_t C_e}$.

1.2.4 Kerr vs Jaynes-Cummings

As it was mentioned above, most of circuit-QED experiments focus on the interaction of microwave photons with circuit elements forming a qubit, the latter being (up to a very good approximation) a two-level system. Under such circumstances, the most relevant effective model to treat light-matter coupling is the Jaynes-Cummings model [47]. In the following, we briefly present its most important characteristics and compare it to the Kerr Hamiltonian of Eq.(1.39).

This model describes the interaction of a single mode of the electromagnetic field with a two level-system, which has a ground state $|g\rangle$ and an excited state $|e\rangle$. The Jaynes-Cummings Hamiltonian is the following:

$$H_{\rm JC} = \hbar\omega_0|e\rangle\langle e| + \hbar\omega_c a^\dagger a + i\hbar\frac{\Omega}{2}(a^\dagger|g\rangle\langle e| - a|e\rangle\langle g|), \tag{1.85}$$

where a is, as usual the annihilation operator for photons, ω_c the frequency of the corresponding mode, $\hbar\omega_0$ the energy of the state $|e\rangle$ and Ω the Rabi frequency of light-matter coupling.

If one tries to derive such a Hamiltonian from first principles, one will realize that all nonresonant terms were neglected. This rotating wave approximation is valid provided that the Rabi frequency Ω is much smaller than ω_0 and ω_c. In the so-called "ultrastrong coupling regime", where $\Omega \sim \omega_0, \omega_c$, these nonresonant terms play a crucial role [48, 49, 50]. However, in the following, we will always consider the regime $\Omega \ll \omega_0, \omega_c$ and we will thus neglect their effect. We mention this approximation primarily to emphasize one of its consequences, namely that the total number of excitations (photonic + matter-like) is conserved. In other words, the subspaces $\mathcal{M}_n$ generated by two states of the form $|n, g\rangle$ and $|n-1, e\rangle$ are closed under the action of H_{JC}.

As a result, the full energy spectrum of H_{JC} is obtained by diagonalizing its restriction to each of the $\mathcal{M}_n$ subspaces. The eigenstates of the resulting 2×2 Hamiltonians are the following [51]:

$$|\Psi_{+,n}\rangle = \cos\theta_n |g, n\rangle + i \sin\theta_n |e, n-1\rangle, \tag{1.86}$$

$$|\Psi_{-,n}\rangle = i \sin\theta_n |g, n\rangle + \cos\theta_n |e, n-1\rangle, \tag{1.87}$$

with:

$$\tan 2\theta_n = \frac{-\Omega\sqrt{n}}{\delta} \quad 0 \leq \theta_n < \pi/2, \tag{1.88}$$

and

$$\delta = \omega_c - \omega_0. \tag{1.89}$$

The energy of these states is:

$$E_{\pm,n} = n\hbar\omega_c - \frac{\delta}{2} \pm \frac{1}{2}\sqrt{n\Omega^2 + \delta^2}. \tag{1.90}$$

As in Eq.(1.58), $|\Psi_{\pm,n}\rangle$ are hybrid light-matter eigenstates and are also called dressed states.

If the Rabi frequency goes to zero while the detuning δ remains positive, then $\theta_n \to 0$ and we recover that within the subspace $\mathcal{M}_n$, the ground state is

$$|\Psi_{-,n}\rangle = |e, n-1\rangle, \tag{1.91}$$

with the energy $E_{-,n} = n\hbar\omega_c - \delta$. In the opposite case of negative detuning, we see from the condition $0 < \theta < \pi/2$, that $\theta \to \pi/2$, and as expected the ground state is

$$|\Psi_{-,n}\rangle = |g, n\rangle, \tag{1.92}$$

and the corresponding energy $E_{-,n} = n\hbar\omega_c$.

The photonic and matter parts of the dressed states are equal (up to a phase) when the cavity mode is at resonance with the $e \to g$ transition ($\delta = 0$). In this case the energy difference, or vacuum Rabi splitting, between the two dressed levels is :

$$E_{+,n} - E_{-,n} = \sqrt{n}\Omega. \tag{1.93}$$

As it can be seen from Eq.(1.90), Kerr and Jaynes-Cummings spectra are, generally speaking, different [52]. The latter can nonetheless be mapped into the former, up to a certain value of n_0, in the limit of large detuning $n_0\Omega \ll |\delta|$. For example, in the case of a large negative detuning, the lowest energy states $|\Psi_{-,n}\rangle$ are almost purely photonic and a Taylor expansion of their energy gives:

$$E_{-,n} = n\hbar\omega' + \frac{U'}{2}n(n-1), \tag{1.94}$$

with an effective cavity frequency

$$\hbar\omega' = \hbar\omega_c - \frac{\Omega^2}{4|\delta|}, \tag{1.95}$$

and a nonlinearity

$$U' = \frac{\Omega^4}{8|\delta|^3}. \tag{1.96}$$

To compare the two models outside of this mapping, it is convenient to define a effective nonlinearity for the Jaynes-Cummings model as

$$U_{eff} = E_{-,2} - 2E_{-,1}. \tag{1.97}$$

An example of energy levels of the two models illustrating this definition is shown on Fig.(1.5). As we shall see when discussing the "photon blockade ", this quantity is particularly relevant in the regime where only a few excited states are populated (e. g., $n = 0, 1, 2$).

1.2.5 Drive and dissipation

We have so far deliberately ignored the issue of driving and dissipation in our description of a cavity. Of course, since the number of photons is not conserved, a pump-loss mechanism of some sort is always at play in optical systems. As we will see at the end of this chapter, the first theoretical investigations of cavity arrays neglected the effects of dissipation on the time scale of simulations (and potential experiments). As a result, only quasi-equilibrium

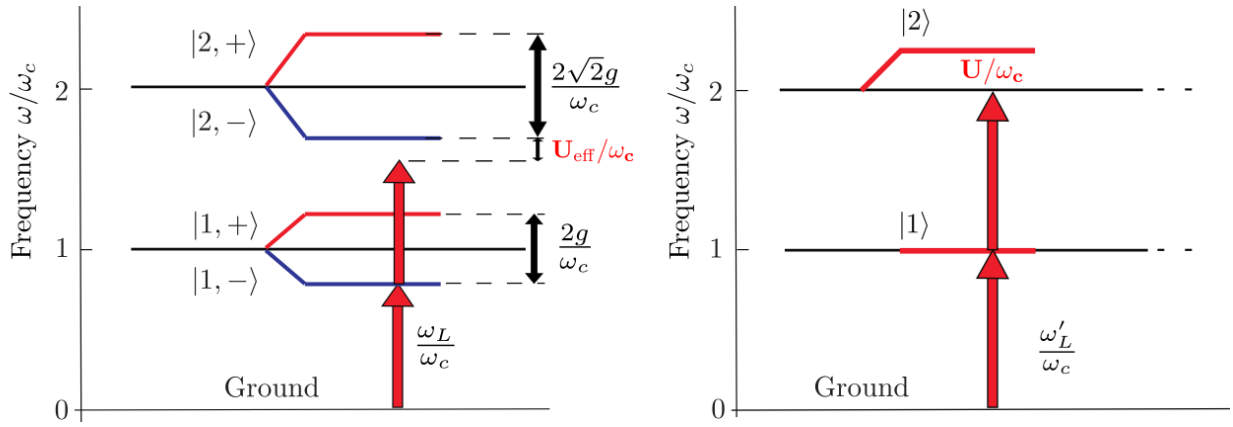

Figure 1.5: Low lying energy levels of Jaynes-Cummings and Kerr Hamiltonians. Left: Jaynes-Cummings with the two-level transition at resonance with the cavity mode ($\delta = 0$). Note that $g = \Omega/2$. Right: Kerr Hamiltonian. Red arrows show that a driving laser exciting resonantly a single-excitation mode from the ground state is detuned from higher excitation modes. From Ref.[52]

dynamics was examined. It is not the choice that we have made in this work. To the contrary we assumed, as it is the case in many cavity and circuit QED experiments, that the intrinsic dissipative nature of the system has a crucial influence on the dynamics.

Let us first look at driving mechanisms. In all that follows we consider optical cavities pumped by an external laser beam. From a theoretical point of view, the coupling of a single cavity to a laser in accounted for by adding an extra term to the Hamiltonian of Eq.(1.39):

$$H_{\text{Kerr+pump}} = \hbar\omega_c b^\dagger b + \frac{U}{2} b^\dagger b^\dagger b b + F e^{-i\omega_p t} b^\dagger + F^* e^{i\omega_p t} b, \tag{1.98}$$

where we have introduced the frequency of the pump ω_p and its amplitude F. Note that in this Hamiltonian, the laser appears as a classical field. We would actually obtain the same result by considering the laser as a quantum field in a purely coherent and stationary state. Indeed a fully quantum Hamiltonian would be:

$$H_{\text{tot}} = \hbar\omega_c b^\dagger b + \frac{U}{2} b^\dagger b^\dagger b b + \hbar\omega_p a^\dagger a + g(a^\dagger b + b^\dagger a), \tag{1.99}$$

with a the annihilation operator corresponding to the laser mode and g a coupling constant. Since the laser is supposed to stay in a purely coherent state at any time, and not to be perturbed by its coupling to the cavity, the total density matrix would be of the form:

$$\rho_{\text{tot}}(t) = \rho_{\text{cav}}(t) \otimes (|\alpha(t)\rangle\langle\alpha(t)|). \tag{1.100}$$

Besides the evolution of $\alpha(t)$ must be governed by free field equations, which gives:

$$\alpha(t) = \langle a(t) \rangle = \alpha_0 e^{-i\omega_p t}. \tag{1.101}$$

Tracing over the laser mode in the Liouville-von Neumann equation [53]

$$i\partial_t \rho_{\text{tot}} = \frac{1}{\hbar}[H_{\text{tot}}, \rho_{\text{tot}}], \tag{1.102}$$

we recover the Hamiltonian of Eq.(1.98) with $F = g\alpha_0$ for the cavity.

The choice of a coherent pumping is not the only possible scenario. For example, a lot of works have been devoted to dissipative Bose-Einstein condensates of polaritons under incoherent pumping. As we will see shorty, one of the fundamental differences between these two choices is that $U(1)$ gauge invariance is preserved in the Hamiltonian under incoherent pumping while it is broken explicitly by a coherent pump.

Let us now turn to dissipation. Spontaneous emission processes originate from the coupling of the cavity mode to the external vacuum modes. This infinite collection of modes act as a Markovian bath of harmonic oscillators. Under appropriate approximation a master equation for the cavity density matrix can be derived by starting from the Liouville-von Neumann equation and tracing over the bath [27]. In contrast with the driving field, dissipation will not be included in the Hamiltonian, since its most important effect is to break the unitarity of the system dynamics. As it is usually the case in quantum optics, the resulting master equation can be cast into a canonical Linblad form and expressed as:

$$i\partial_t \rho_{\text{cav}} = \frac{1}{\hbar}[H_{\text{Kerr+pump}}, \rho_{\text{cav}}] + \frac{i\gamma}{2}[2b\rho_{\text{cav}}b^\dagger - b^\dagger b\rho_{\text{cav}} - \rho_{\text{cav}}b^\dagger b], \tag{1.103}$$

where γ is the cavity loss rate. The main goal of this thesis is to find the stationary solutions of Eq.(1.103) extended to arrays of cavities.

1.2.6 Effective Hamiltonian for nonlinear cavity arrays

At this point we have at our disposal all the necessary ingredients for writing down an effective Hamiltonian and a master equation for the full array of coupled cavities. Photon hopping is allowed by evanescent coupling of neighboring cavities due to their proximity. It is included in the Hamiltonian in the from of:

$$H_{\text{hop}} = -J \sum_{\langle i,j \rangle} b_i^\dagger b_j, \tag{1.104}$$

where $\langle i,j\rangle$ indicates that the sum runs over first neighbors only. Bringing Eq.(1.104) together with single-cavity Kerr Hamiltonians, we obtain the driven-dissipative Bose-Hubbard model:

$$H = -\frac{J}{z}\sum_{<i,j>} b_i^\dagger b_j + \sum_{i=1}^{N}\hbar\omega_c b_i^\dagger b_i + \sum_{i=1}^{N}\frac{U}{2}b_i^\dagger b_i^\dagger b_i b_i + \sum_{i=1}^{N}(Fe^{-i\omega_p t}b_i^\dagger + F^* e^{i\omega_p t}b_i), \tag{1.105}$$

where N is the number of cavities and z the lattice coordination number (number of nearest neighbors). The corresponding master equation is:

$$i\partial_t\rho = \frac{1}{\hbar}[H,\rho] + \frac{i\gamma}{2}\sum_{i=1}^{N}(2b_i\rho b_i^\dagger - b_i^\dagger b_i\rho - \rho b_i^\dagger b_i). \tag{1.106}$$

The first thing to be noticed about Eq.(1.105) is that it is time-dependent. It is convenient to eliminate this time dependence by performing a unitary transformation on the density matrix:

$$\rho \to U\rho U^\dagger, \tag{1.107}$$

where $U = e^{i\omega_p t\sum_i b_i^\dagger b_i}$. This amounts to writing the density matrix in a frame rotating at the pump frequency ω_p. In this rotating frame, the general Linblad form of the master equation remains the same but the Hamiltonian governing the dynamics is now time independent:

$$H_{rf} = -\frac{J}{z}\sum_{<i,j>} b_i^\dagger b_j - \sum_{i=1}^{N}\hbar\Delta\omega b_i^\dagger b_i + \sum_{i=1}^{N}\frac{U}{2}b_i^\dagger b_i^\dagger b_i b_i + \sum_{i=1}^{N}(Fb_i^\dagger + F^* b_i). \tag{1.108}$$

We have introduced the detuning between the pump the bare cavity frequency $\Delta\omega = \omega_p - \omega_c$. From now on, we will be exclusively studying this rotating frame Hamiltonian.

Note that the chemical potential μ, which is a key quantity for equilibrium quantum gases, is replaced in this non-equilibrium model by three other parameters, F, $\Delta\omega$ and γ. This substantially enlarges the parameter space.

Before starting to investigate in details the model described by Eq.(1.108) and Eq.(1.106) (which will be the focus of the remaining chapters), we first discuss some of the most important results regarding nonlinear cavity arrays that have been obtained recently. We begin by presenting the phenomenon that has triggered a lot of these works: the photon blockade.

1.3 Photon blockade

A blockade effect analogous to the Coulomb blockade of electrons in mesoscopic quantum dots [54], occurs in a nonlinear optical cavity when the presence of a single photon is sufficient

to inhibit the absorption of a second one. This spectacular effect is therefore one of the most eloquent example of strong quantum correlations in optical systems. In terms of photon emission, it means that in the ideal case, it is impossible for the cavity to emit two photons at the same time. A perfect photon blockade thus yields perfect antibunching, i.e., $g^{(2)}(0) = 0$.

1.3.1 Photon blockade in Kerr and Jaynes-Cummings Hamiltonians

In an optical system described by the Kerr or Jaynes-Cummings Hamiltonian, the photon blockade originates from a very large photon-photon interaction. In both models, the nonlinearity between the lowest-energy single-photon state and the lowest-energy two-photon state is given by $|E_2 - 2E_1|$, where E_1 and E_2 are the energies of the single-photon and two-photon states respectively. If this energy shift is much larger than the line width $\hbar\gamma$ of the energy levels, an external laser field tuned at the single-photon frequency will not be able to inject a second photon inside the cavity. In the case of the Kerr Hamiltonian, the nonlinearity defined above is given directly by the parameter U and the condition for photon blockade then reads

$$U/(\hbar\gamma) \gg 1. \tag{1.109}$$

In the Jaynes-Cummings model, this relation becomes $\Omega/(\hbar\gamma) \gg 1$, since in this case the nonlinearity is given by $\Omega(1 - \sqrt{2}/2)$.

Although the principles underlying the photon blockade seem relatively simple, its experimental observation is a real challenge. Indeed, the strength of the effective photon-photon interaction is always the most crucial parameter when discussing experiments on quantum fluids of light and reaching high enough nonlinearities is non trivial. In this context, the theoretical proposal of Imamoglu *et al.* [55] was an important milestone. Using a more complex model than the ones outlined above they showed that the photon blockade regime could be reached using a gas of 4-level atoms as a nonlinear medium. Before discussing in more details the mechanism responsible of photon-photon interactions in this proposal, let us mention that, regarding the photon blockade with Jaynes-Cummings nonlinearities, spectacular results have been obtained more recently with superconducting circuits [56] and single atoms in optical cavities [57]. Possible observation of photon blockade in semiconductor microcavities was also proposed by Verger *et al.*[43].

1.3.2 Giant Kerr effect with 4-level atoms

The medium considered by Imamoglu *et al.* [55] was an assembly of 4-level atoms embedded in a optical cavity. A scheme of the atomic levels is presented in Fig.(1.6). They form a Λ shape with one extra level and the frequencies of the $3 \rightarrow 4$ and $1 \rightarrow 3$ transitions are assumed to be close to the cavity frequency. In addition, the $2 \rightarrow 3$ transition is driven by a nonperturbative external laser field. In order to grasp the meaning of this choice let us first go back to the more general phenomenon of Kerr nonlinearities in a standard 3-level system.

Let the atoms under consideration have a ground state $|a\rangle$, an intermediate state $|b\rangle$ and a final state $|c\rangle$. In the most general case, the $|a\rangle \rightarrow |b\rangle$ transition is addressed by a pump laser with a coupling Rabi frequency Ω_p and the $|b\rangle \rightarrow |c\rangle$ transition by a signal field with a coupling frequency Ω_s (see right panel of Fig.(1.6)) In the proposal of Ref.[55], signal and pump fields are in fact the same incident field. The nonlinear susceptibility $\chi^{(3)}$ is deduced from the atomic polarization:

$$P(t) = \frac{\langle e\mathbf{r}\rangle}{V}, \tag{1.110}$$

which is in turn computed by solving the Bloch equations for the atoms perturbatively in the fields. The real part of $\chi^{(3)}$, which is responsible for photon-photon interactions, is given by:

$$\mathrm{Re}[\chi^{(3)}_{3-\mathrm{level}}] = \frac{|d_{ab}|^2|d_{bc}|^2\rho}{8\hbar^3\epsilon_0}\frac{1}{\Delta\omega_{ab}^2\Delta\omega_{bc}}, \tag{1.111}$$

where ρ is the atomic density, d_{ab} and d_{bc} the dipole matrix elements of the transitions and $\Delta\omega_{ab}$ and $\Delta\omega_{bc}$ the detuning of the lasers with respect to these transitions.

What we learn from Eq.(1.111) is that in order for the nonlinearity to be high, the detunings should be small. There is however an intrinsic limitation to $\Delta\omega_{ab}$ and $\Delta\omega_{bc}$: they must be much larger than the transitions width in order to avoid absorption.

It is however possible to overcome this limitation by using the 4-level system presented above. Indeed, one of the effects of the laser coupling the levels 2 and 3 is a drastic reduction of absorption, known as electromagnetically induced transparency [36]. It is a consequence of an interference effect involving the two states dressed by the external field (see Fig.(1.6), right panel). In this 4-level scheme, the real part of the nonlinear susceptibility is given by:

$$\mathrm{Re}[\chi^{(3)}_{4-\mathrm{level}}] = \frac{|d_{13}|^2|d_{24}|^2\rho}{2\hbar^3\epsilon_0}\frac{1}{\Omega_c^2\Delta\omega_{42}}. \tag{1.112}$$

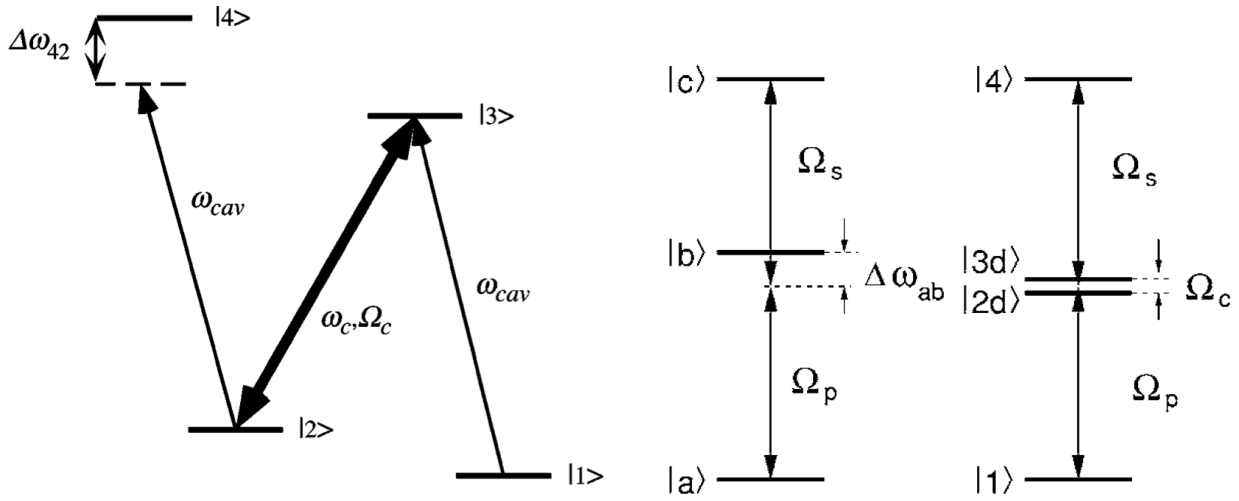

Figure 1.6: Left: Level scheme leading to a giant Kerr effect. Optical transitions $3 \rightarrow 2$ and $3 \rightarrow 1$ are assumed to be resonant. From Ref.[55]. Left: Levels configuration in a ordinary 3-level system (right) and dressed-state representation of the giant Kerr scheme. From Ref.[36].

The two expressions Eq.(1.111) and Eq.(1.112) look very similar, but in the second one, $\Delta\omega_{ab}^2/4$ is replaced with Ω_c^2. In contrast to the standard 3-level system, it is possible to have $\Omega_c \ll \Gamma_3$ in a scheme with EIT. This implies that the magnitude of the Kerr nonlinearity can be orders of magnitude larger in the latter case.

As will shall the see at the end of this chapter, this EIT scheme played an important role in the first investigations of many-body phenomena in arrays of coupled nonlinear cavities.

1.3.3 Unconventional Photon Blockade

The above presentation of the photon blockade leads to believe that huge nonlinearities are necessary to observe the required quasi-perfect antibunching. It turns out however, that perfect antibunching is also achievable with very weak nonlinearities, provided that we consider not a single cavity but a "molecule" of two coupled cavities.

This "unconventional photon blockade" in photonic molecules was first predicted by Liew and Savona [58]. They considered a two-site version of the driven-dissipative Bose-Hubbard Hamiltonian of Eq.(1.108), but where only one of the two cavities is pumped. As shown in the left panel of Fig.(1.7), quasi-perfect antibunching in the pumped cavity is obtained for optimized values of U and $\Delta\omega$ and for a nonlinearity as small as $U/\gamma \approx 0.08$. An interpretation of this surprising result in term of a quantum interference effect was given

shortly after by Bamba *et al.* [59]. In this case, the probability of having two photons in the driven cavity is cancelled by the destructive interference of the two paths presented in the right panel of Fig.(1.7). By solving the master equation exactly in the limit of very weak pumping, i.e. $F/\gamma \ll 1$, Bamba *et al.* provided an analytical formula for the optimal value of the parameters leading to the strongest antibunching:

$$\Delta\omega_{\rm opt} \approx -\frac{\gamma}{2\sqrt{3}}, \tag{1.113}$$

$$U_{\rm opt} \approx \frac{4}{3\sqrt{3}}\frac{\gamma^3}{J^2}, \tag{1.114}$$

where we have used the same notations as in Eqs.(1.105) and (1.108). In view of the potential applications in the design of photonic devices, the unconventional photon blockade has been the focus of several studies in the past few years [60, 19, 61].

Interestingly, it was shown very recently by Lemonde *et al* that this interference effect could be also viewed as a particular case of optimal amplitude squeezing in a Gaussian state [62].

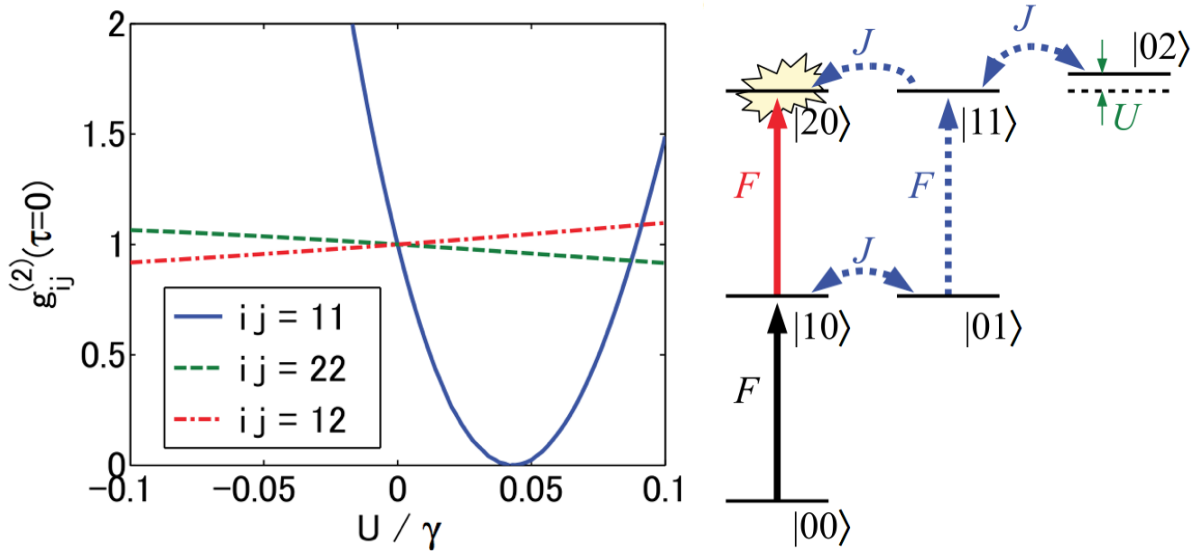

Figure 1.7: Left: Equal-time second-order correlation functions $g^{(2)}_{ij}(0) = \langle b_i^\dagger b_j^\dagger b_i b_j\rangle/(\langle b_i^\dagger b_i\rangle\langle b_j^\dagger b_j\rangle)$ as functions of the nonlinearity. Nearly perfect antibunching is obtained for $U/\gamma = 0.0856$ The parameters are $\Delta\omega/\gamma = -0.275$, $J/\gamma = 3$ and $F/\gamma = 0.01$. Right: Transition paths leading to the quantum interference responsible for the strong antibunching. One path is the direct excitation from $|10\rangle$ to $|20\rangle$, but it is forbidden by the interference with the other path drawn by dotted arrows. From Ref.[59]

1.4 Review of recent theoretical results on arrays of nonlinear cavities

The experimental demonstration of the photon blockade and the possibility of achieving large effective photon-photon interactions triggered the theoretical investigation of quantum phase transition in arrays of coupled cavities. For material particles in thermal equilibrium propagating on a lattice (such as cold atoms in an optical lattice), the interplay between on-site repulsion and hopping between neighboring sites is known to give rise to a quantum phase transition between a Mott insulator and a superfluid phase [63]. This transition is predicted by the equilibrium Bose-Hubbard model which will be reviewed in more details in the next chapter. For now let us keep in mind that in a Mott state at integer fillings, particles are well localized on each sites, while they are delocalized on the whole lattice in the superfluid phase. Recovering a similar behavior with photons or polaritons was at the heart of the first studies on cavity arrays.

1.4.1 Quasi-equilibrium phase transitions

The first proposals considered the strong coupling of light to 2-level [64, 65] or 4-level atoms [66]. All these works were based on the assumption that dissipation processes in the system do not significantly alter the dynamics on the time scale of realistic experiments.

Neglecting dissipation allowed for the use of the well-tried techniques of equilibrium many-body physics. Following this path, Greentree *et al.* established the equilibrium mean-field phase diagram of the Jaynes-Cummings-Hubbard model [64]. The photonic coherence was identified as the order parameter of a Mott-insulator-to-superfluid transition with a "lobe" structure that shares many similarities with that of the Bose-Hubbard model (see Fig.(1.9)). Investigating the same phase transition, Hartmann *et al.* [66] and Angelakis *et al.* [65] chose a different strategy: by means of exact numerical calculations, they explored the time evolution of a few polaritons in small arrays (3-7 cavities). They were able to characterize the transition by evaluating the fluctuation of the polaritons occupation number as the system parameters varied in time (see Fig.(1.8)). As expected fluctuations are suppressed in the Mott phase and increased when driving into the superfluid phase.

Numerical simulations of large one-dimensional arrays ($\sim$ 100 cavities) performed by Rossini and Fazio [67] confirmed these first results. In particular, the lobe structure of the phase diagram predicted by mean-field theory was recovered (see Fig.(1.9)). Inspired by what had been successfully done for the equilibrium Bose-Hubbard model, they extended

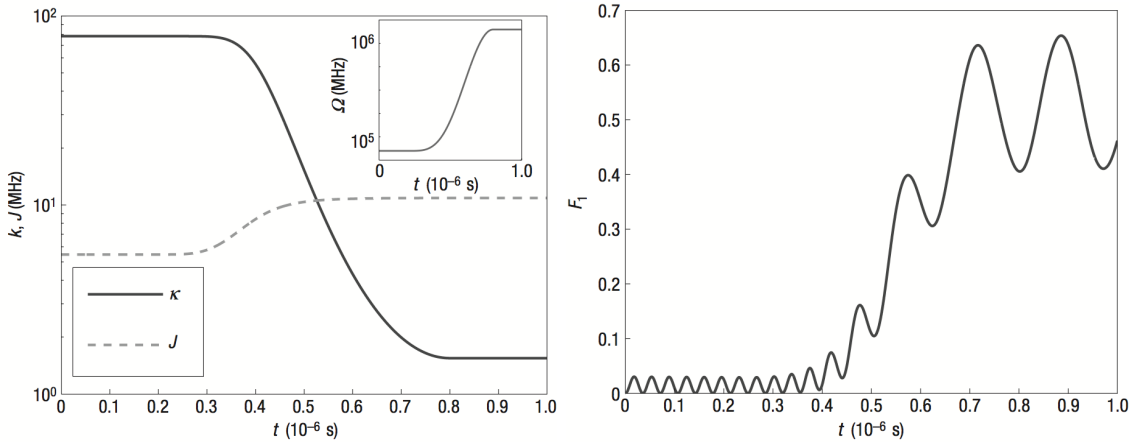

Figure 1.8: Mott-insulator-to-superfluid transition seen from the dynamics of 3 polaritons in 3 cavities. Left: log plots of the on-site repulsion κ and the tunneling rate J, linear plot of time-dependent coupling to the driving laser Ω_L. Right: Number fluctuations for polaritons in the first cavity $F_1 = \langle n_1^2 \rangle - \langle n_1 \rangle^2$ as a function of time. Bulding-up of fluctuations in the occupation number as J/κ is increased is a signature of the phase transition. From [66]

.

their study to include the effects of disorder and showed the emergence of a glassy photon phase.

In their treatment of light-matter coupling, all the work cited in this section so far are based on the rotating-wave approximation. In the Hamiltonian coupling the electromagnetic field to atoms, all non-resonant terms are discarded. As we have seen above, this leads, in the case of two-level atoms to the Jaynes-Cummings model. This approximation ceases to be valid in the ultra-strong coupling regime, when the Rabi frequency is of the same order as the atomic frequency. In this regime the Jaynes-Cummings model is to be replaced with the quantum Rabi model. The mean-field phase diagram of the Rabi-Hubbard model has been obtained by Schiro *et al.* [68]. The authors show that the non-resonant terms drastically modified the nature of the phase transition. While in the Jaynes-Cummings model, the total number of excitations (matter excitations + photons) is conserved, only the parity of this number remains a conserved quantity in the Rabi-Hubbard model. As a consequence, the phase transition exhibits a Z_2 symmetry breaking and is of Ising universality class.

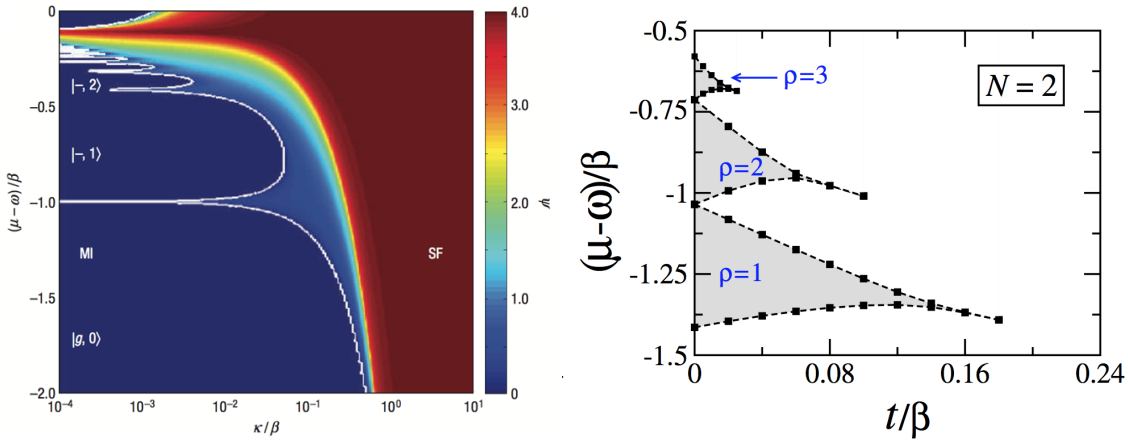

Figure 1.9: Right: Mean-field phase diagram of the Jaynes-Cummings-Hubbard model. Order parameter $\psi = \langle b \rangle$ as a function of the tunneling rate κ and the chemical potential μ. From Ref.[64]. Left: DMRG simulations on 1D arrays with $N = 2$ atoms per cavities. ρ is the polariton density. The atomic transition frequency is at resonance with the cavity mode. From Ref.[67].

1.4.2 Photon Fermionization and Crystalization in Driven-Dissipative models

Soon after the first proposals regarding arrays of nonlinear cavities, it was realized that a better understanding of many-body effects in systems where dissipation could not be neglected would be of great interest. On the one hand driven-dissipative models are undoubtedly relevant in view of experimental implementations with microcavities and superconducting circuits and on the other hand new phenomena may arise from their intrinsic non-equilibrium nature.

The first theoretical study with a full account of driving and dissipation was performed by Carusotto *et al.* [69]. They considered a one dimensional Hamiltonian similar to Eq.(1.108) with periodic boundary conditions and under homogeneous coherent pumping. When compared with the works on quasi-equilibrium configurations mentioned above, there is a clear change of paradigm. The system is now considered as an optical device characterized by its transmission, and second-order correlation functions. In particular, the energy spectrum is probed by computing the total transmission $\sum_i \langle b_i^\dagger b_i \rangle$ (using same conventions as in Eq.(1.108)) for different pumping frequencies. Peaks in the transmission spectrum are associated with different many-body states containing n particles (see Fig.(1.10)). By means of a Bose-Fermi mapping in the limit of strong interactions $U/J \gg 1$ (hard-core bosons),

and weak pumping F, the authors predict in this regime a fermionization of photons and the onset of a Tonks-Girardeau phase. This picture is confirmed by the value of second-order cross and autocorrelation functions.

Closely related results were obtained by Hartmann [70]. Investigating the same system, but with the phase of the laser tuned so as to pump the $\mathbf{k} = \pi/2$ polariton mode he identified 'polariton crystallization'. Instead of analytical estimates as in [69], his results were based on numerical simulations using time evolving block decimation algorithm for a one-dimensional array of 16 cavities. The concept of photon crystal was later extended to arrays of cavities with cross-Kerr nonlinearities by Jin *et al.* [71]. To the driven-dissipative Bose-Hubbard Hamiltonian of Eq.(1.108) was added the term: $\sum_{<i,j>} V b_i^\dagger b_j^\dagger b_j b_i$ representing the coupling of cavities by nonlinear elements (see Fig.(1.11)). A mean-field study backed up by numerical simulation on 1D arrays showed a checkerboard ordering of the mean photon density.

A mean-field study of the driven-dissipative Jaynes-Cummings-Hubbard model was performed by Nissen *et al* [72]. The external laser was tuned so as to pump the bottom of the lower polariton branch. They showed that for weak hopping the photon blockade effect remained present but was destroyed in the strong hopping limit. As the crossover between the two regimes is smooth, no trace of the MI-SF transition was visible. The authors briefly suggested that tunneling induced bistability might occur for high pumping intensities.

In all of the works presented in this subsection, the effects of strong photon-photon interactions are not formulated in terms of a Mott insulator to superfluid phase transition. One of the reason is that the equilibrium phase transition is associated with spontaneous breaking of the Hamiltonian's $U(1)$ symmetry which is explicitly broken when adding a coherent pumping to the system. To circumvent this apparent difficulty while remaining in a driven-dissipative regime with coherent pumping, Tomadin *et al.* investigated the dynamics of a cavity array excited by a pulsed laser [73]. Momentarily broken for the duration of the excitation pulse which injects photons into the system, the $U(1)$ symmetry is restored afterwards. In what is identified by the authors as a superfluid regime, instabilities in the photonic coherence develop, similarly to what happens with material particles. Most importantly, the change in $g^{(2)}(0)$, from 0 to 1 occurring as the ratio J/U is increased is considered a strong signature of the MI-SF transition (see Fig.(1.10)).

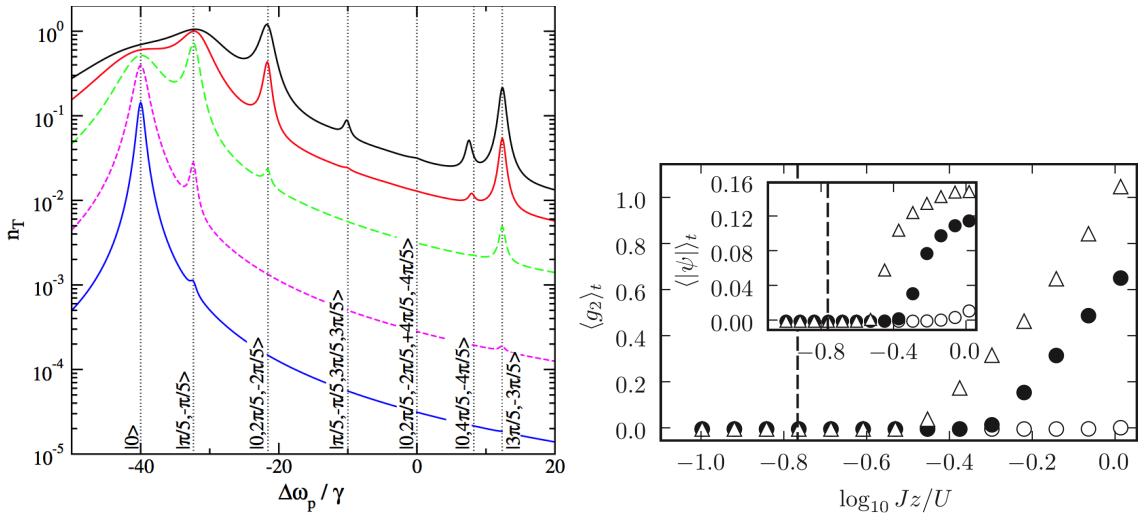

Figure 1.10: Left: photon fermionization in a 1D array. From Ref.[69]. Total transmission spectra as a function of the detuning frequency $\Delta\omega_p = \omega_p - \omega_c$. System of 5 cavities in the impenetrable boson limit $U/J = \infty$, with $J/\gamma = 20$. Different curves correspond to increasing values of the pump amplitude $F/\gamma = 0.1, 0.2, 1, 2, 3$. Vertical dot lines indicate the spectral position of the peaks predicted by the fermionization procedure. Right: MI-SF transition in an array of cavities pumped by a pulsed laser [73]. Time average of $g^{(2)}(0)$ and integral of $\langle b \rangle$ (inset) in the time interval $1/\gamma < t < 2/\gamma$ for different values of the damping: $\gamma/U = 0.02$ (empty circles), 0.01 (filled circles) and 0.005 (triangles), $\Delta\omega = 0$. The vertical dashed line marks the critical value of the MI-SF transition for the equilibrium Bose-Hubbard model.

1.5 Conclusion

In this chapter, we have introduced the basic concepts and key state-of-the-art literature which are essential to the understanding of this PhD thesis. The remainder of the manuscript is devoted to the study of the driven-dissipative Bose-Hubbard Model. From the short review presented above, we see that the relation between equilibrium and driven-dissipative models is of crucial importance, in particular when discussing the Mott-insulator-to-superfluid phase transition. Defining an equivalent of this transition in the driven-dissipative case, where the $U(1)$ symmetry is explicitly broken and the mean density of particles in the steady-states determined by three parameters, F, γ and $\Delta\omega$ instead of the single chemical potential, is not obvious. Consequently, we will begin our investigation in the next chapter by elucidating this question.

Besides, at the time this thesis was started, there was no systematic study of this model for a two-dimensional lattice in the thermodynamical limit. It is therefore on this aspect that

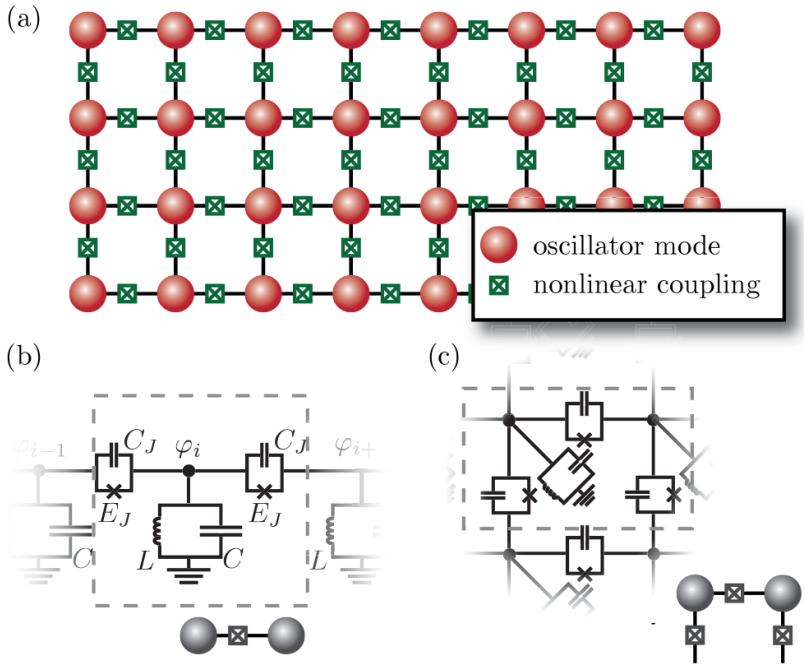

Figure 1.11: (a) An array of cavities described by oscillator modes (red circles) that are coupled via nonlinear elements (crossed boxes). (b), (c) Implementation of its building blocks in circuit QED for one- and two-dimensional lattices. The circuit cavities are represented by a LC circuit with capacitance C and inductance L and mutually coupled through a Josephson nanocircuit, with capacitance C_J and Josephson energy E_J, that generates the on-site and cross-Kerr terms. From Ref.[71].

part of the work presented here is focused. A good start in this direction is to establish the general phase-diagram within the mean-field approximation. This is the aim of Chapter 3.

Chapter 2

Equilibrium vs driven-dissipative Bose-Hubbard model

When discussing results on the driven-dissipative Bose-Hubbard model with people from the cold-atom community, a question inevitably arises: "What happens in your model when F and γ go both to zero?". In this limit, it should indeed resemble more and more to its better-known equilibrium counterpart. Exploring the regime of weak pumping and weak dissipation seems therefore a good way to clarify the relation between the two models. Before embarking on this investigation, we will review some important results on the equilibrium Bose-Hubbard model.

Originally introduced by Hubbard for the understanding of electron transport in metals [74], its study for bosonic particles was first carried out in 1989 in a seminal paper by Fisher *et al.* [63]. Using mean-field theory, they predicted the celebrated Mott-insulator-to-superfluid transition that we have already encountered in the preceding chapter. The understanding of this phase transition was subsequently deepened by numerous theoretical studies using various methods, such as the random phase approximation [75], strong-coupling expansions [76, 77, 78] or dynamical mean-field theory [79]. This model gained a renewed interest with the experimental observation of the transition with cold atoms in optical lattices [20]. In particular, the advent of efficient quantum Monte-Carlo algorithms for equilibrium bosonic systems allowed for very accurate numerical simulations [80, 81]. All these works confirmed that the results of mean-field theory were qualitatively correct.

After reviewing the mean-field phase diagram of the equilibrium Bose-Hubbard model, we will extend this approach to the driven-dissipative model and present our results concerning the regime of weak pumping and weak dissipation. Instead of pure Mott insulator states, we find statistical mixtures with the same second-order coherence $g^{(2)}(0)$ as a Fock state with n

photons, but a mean photon number of $n/2$. These mixed states occur when n pump photons have the same energy as n interacting photons inside the nonlinear cavity and survive up to a critical tunneling coupling strength, above which a crossover to classical coherent state takes place. The original results presented in this chapter are published in [22].

2.1 Bose-Hubbard model at equilibrium

In this first section we derive the mean-field phase diagram of the equilibrium Bose-Hubbard model. This will give us the opportunity to go over the main features of the Mott-insulator-to-superfluid phase transition and to introduce important methods that will be extended to driven-dissipative systems.

For material particles in thermal equilibrium, the grand-canonical Bose-Hubbard Hamiltonian is the following ($\hbar = 1$):

$$H_{eq} = -\frac{J}{z}\sum_{<i,j>} b_i^\dagger b_j + \sum_{i=1}^{N}\frac{U}{2} b_i^\dagger b_i^\dagger b_i b_i - \sum_{i=1}^{N}\mu b_i^\dagger b_i. \tag{2.1}$$

We recognize the parameters J and U introduced previously. As for μ, it denotes the chemical potential. In this thesis, we will only consider the repulsive model, with $U > 0$. The physical meaning of U in this context appears more clearly when the repulsion term is written as a function of the number operator $\hat{n}_i$: $\frac{1}{2} b_i^\dagger b_i^\dagger b_i b_i = \frac{1}{2}\hat{n}_i(\hat{n}_i - 1)$. The right-hand side of this last equation gives the number of pairs of particles at site i. The parameter U is thus the energy cost of on-site pair formation.

2.1.1 Two simple limits: $J = 0$ and $U = 0$

As all the interesting physics in this model stems from the competition between the kinetic part of the Hamiltonian governed by J and the on-site repulsion characterized by U, it is instructive to look at the two limiting cases $J = 0$ and $U = 0$.

Isolated "Hubbard atoms"

For $J = 0$, all the sites are decoupled and may be seen as individual "Hubbard atoms". The Hamiltonian reads:

$$\sum_i \frac{U}{2}\hat{n}_i(\hat{n}_i - 1) - \sum_i \mu\hat{n}_i. \tag{2.2}$$

It is diagonal in real space. At zero temperature, the ground state is therefore a tensor product of the form:

$$|\psi\rangle_{MI} = \bigotimes_i |\overline{n}\rangle_i, \tag{2.3}$$

where $\overline{n}$ is the number of particles per site, whose value is fixed by the chemical potential μ. The energy of each Hubbard atom is:

$$E_n^{(0)} = -\mu n + \frac{1}{2}n(n-1)U. \tag{2.4}$$

Thus the ground state in the atomic limit is a so called Mott insulator, with the particles perfectly localized on each site and without any fluctuations in the occupation number.
It is useful to compute the energy required, in such a state, for a particle to move from one site to the next:

$$\begin{aligned}\Delta E &= E(n+1) + E(n-1) - 2E(n) \\ &= \frac{U}{2}\left(n(n+1) + (n-1)(n-2) - 2n(n-1)\right) \qquad (2.5)\\ &= U. \qquad (2.6)\end{aligned}$$

This confirms the physical interpretation of U given above.

Freely propagating particles

In the opposite case where $U = 0$ the Hamiltonian becomes:

$$-\frac{J}{z}\sum_{<i,j>} b_i^\dagger b_j - \sum_{i=1}^{N}\mu\hat{n}_i. \tag{2.7}$$

It is not diagonal in real space anymore, but it is in reciprocal space. The ground state is then a state with all the particles condensed in the one-particle zero-momentum state $|k=0\rangle$. In real space, the state of the system reads:

$$|\psi\rangle_{SF} = \frac{1}{\sqrt{N!}}\left(\frac{1}{\sqrt{M}}\sum_{i=1}^{N} b_i^\dagger\right)^N |0\rangle, \tag{2.8}$$

where N is the total number of particles and M the number of lattice sites. It is clear from the expression for $|\psi\rangle_{SF}$ that in this state, contrary to the preceding case, particles are delocalized on the entire lattice and that on a given lattice site, the number of particles fluctuates.

It is interesting to notice that in the thermodynamical limit $N \to \infty$, the state $|\psi\rangle_{SF}$ can be approximately written as a tensor product of coherent states on each site [82]:

$$|\psi\rangle_{SF} \approx \bigotimes_i |\alpha\rangle_i, \tag{2.9}$$

the parameter α being the same on each site, and such that $|\alpha|^2$ is equal to the mean particle density.

2.1.2 Mean-field phase diagram

Equations (2.3) and (2.9) indicate that in both limits $J = 0$ and $U = 0$, the ground state is factorized, that is, a tensor product of single-site states. This encourages to try a variational approach to the general problem [83]. Let us assume that the total ground state takes the form of a Gutzwiller ansatz:

$$|\psi\rangle_{GS} = \bigotimes_{i=1}^{N} |\phi\rangle. \tag{2.10}$$

The problem is then reduced to finding the state $|\phi\rangle$ that minimizes the energy. The virtue of this approximation is that it reduces the original many-body problem to a single-site problem. The effective Hamiltonian H_{mf} for $|\phi\rangle$ is derived by injecting Eq.(2.10) into the general Schrödinger equation and projecting it on a single site. This procedure is actually equivalent to a decoupling of the sites directly inside the total Hamiltonian H_{eq}. Indeed, the approximation:

$$b_i^\dagger b_j \approx \langle b_i^\dagger\rangle b_j + \langle b_j\rangle b_i^\dagger - \langle b_i^\dagger\rangle\langle b_j\rangle, \tag{2.11}$$

which is typical of mean-field theories, yields the same effective single-site Hamiltonian, namely:

$$H_{mf} = -\mu b^\dagger b + \frac{U}{2} b^\dagger b^\dagger b b - J\langle b\rangle^* b - J\langle b\rangle b^\dagger. \tag{2.12}$$

From here, the idea is to start from the ground state at $J = 0$ and to treat the source term due to the hopping appearing in Eq.(2.12) as a perturbation.

Let n be an integer such that $\mu/U \in [n-1, n]$. As seen in the previous subsection, the ground state is $|n\rangle$, with the corresponding energy $E_n^{(0)}$. Since our primary goal is to write a self-consistent equation for $\langle b\rangle$, we need to determine the perturbed eigenstates $|\phi_n\rangle$ and compute $\langle\phi_n|b|\phi_n\rangle$. Operators b and $b^\dagger$ only couple $|n\rangle$ to $|n-1\rangle$ and $|n+1\rangle$ respectively. At first order, the expansion of $|\phi_n\rangle$ in the unperturbed Fock basis is therefore:

$$|\phi_n\rangle = c_{n-1}|n-1\rangle + c_n|n\rangle + c_{n+1}|n+1\rangle, \tag{2.13}$$

and the expression for $\langle b\rangle$ is:

$$\langle\phi_n|b|\phi_n\rangle = \sqrt{n}c_n c_{n-1}^* + \sqrt{n+1}c_{n+1}c_n^*. \tag{2.14}$$

The coefficients c_k are given by usual time-independent perturbation theory:

$$c_n = 1 + O(J^2|\langle b\rangle|^2), \tag{2.15}$$

$$c_{n-1} = \frac{-J\langle b\rangle^*\langle n-1|b|n\rangle}{E_n^{(0)} - E_{n-1}^{(0)}} = \frac{-J\langle b\rangle^*\sqrt{n}}{-\mu + (n-1)U}, \tag{2.16}$$

$$c_{n+1} = \frac{-J\langle b\rangle\langle n+1|b^\dagger|n\rangle}{E_n^{(0)} - E_{n+1}^{(0)}} = \frac{-J\langle b\rangle\sqrt{n+1}}{\mu - nU}. \tag{2.17}$$

Injecting the above expressions into Eq.(2.13) yields the following self-consistent equation for $\langle b\rangle$:

$$\langle b\rangle = J\langle b\rangle\left(\frac{n}{\mu - (n-1)U} + \frac{n+1}{nU-\mu}\right). \tag{2.18}$$

We see that a non-zero solution for $\langle b\rangle$ may exist only if the relation:

$$J\left(\frac{n}{\mu - (n-1)U} + \frac{n+1}{nU-\mu}\right) = 1, \tag{2.19}$$

is satisfied. Expression (2.19) is actually an implicit equation for the boundary between the two phases: at small J the only solution is $\langle b\rangle = 0$. This last equality holds until J reaches a critical value given by Eq.(2.19). A plot for $n = 1, 2, 3$ is presented on Fig.(2.1).

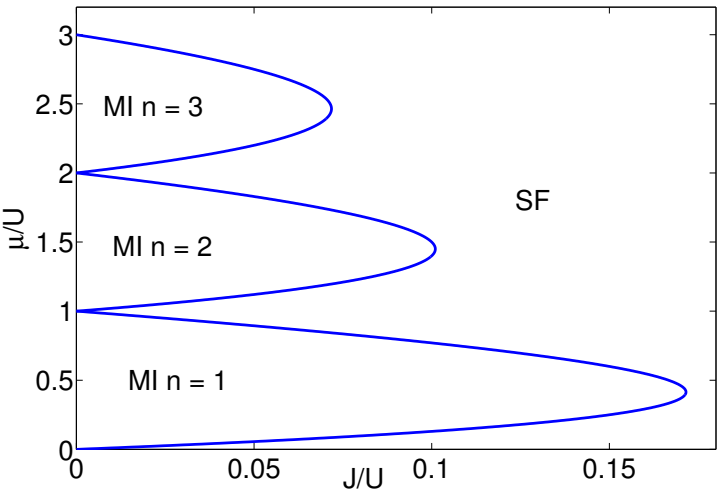

Figure 2.1: Mean-field phase diagram of the equilibrium Bose-Hubbard model. Inside each lobe, the ground state is a Mott insulator (marked "MI"), with a definite number of particle on each site ($n = 1$, 2, 3). Outside of the lobes, the state is superfluid (marked "SF").

It is convenient to study the phase diagram in the $(\mu/U, J/U)$-plane and write $\tilde{J} = J/U$; $\tilde{\mu} = \mu/U$. Equation (2.19) expressed in terms of these normalized variables can be written as:

$$\tilde{J} = \frac{(\tilde{\mu} - n + 1)(n - \tilde{\mu})}{\tilde{\mu} + 1}. \tag{2.20}$$

The maximal value of J on the boundary is given by the condition $\frac{d\tilde{J}}{d\tilde{\mu}} = 0$. This yields:

$$\tilde{\mu}_m = \sqrt{n(n+1)} - 1, \tag{2.21}$$

$$\tilde{J}_m = \frac{1}{(\sqrt{n} + \sqrt{n+1})^2}. \tag{2.22}$$

Note that $\tilde{\mu}_m < n - 1/2$, which reflects the fact that the lobes are not symmetric with respect to $\mu = n - 1/2$. Besides, Eq.(2.22) indicates that the size of the lobe shrinks as n increases.

2.2 Driven-dissipative model under weak pumping and weak dissipation

While keeping in mind the results at equilibrium, we now turn to the driven-dissipative case. We recall that the Hamiltonian under consideration (in the rotating frame) is the following:

$$H_{rf} = -\frac{J}{z} \sum_{<i,j>} b_i^\dagger b_j - \sum_{i=1}^{N} \hbar\Delta\omega b_i^\dagger b_i + \sum_{i=1}^{N} \frac{U}{2} b_i^\dagger b_i^\dagger b_i b_i + \sum_{i=1}^{N} (F b_i^\dagger + F^* b_i), \tag{2.23}$$

and that the dynamics is given by the master equation (1.106), characterized by a dissipation rate γ. In addition, we assume that F and γ are both very small when compared with the detuning $\Delta\omega$. Without any loss of generality, we will also assume that F is real. The way to proceed in order to find the steady-states will be the same as in the previous section: we consider first the case of an isolated cavity with $J = 0$ and then treat the coupling between sites within the mean-field approximation.

2.2.1 Single cavity: Analytical solution

At equilibrium, we have seen that the ground state of an isolated site is a pure Fock state $|n\rangle$, with n fixed by the value of the chemical potential. If we are to find some sort of equivalent in the driven-dissipative case, we must look for steady-states with a mean photon density $\langle b^\dagger b \rangle \geq 1$. Since photon always have to be injected inside the cavity, and since in the present case the coupling to the external field is assumed to be very weak, the only way to have $\langle b^\dagger b \rangle \geq 1$ is to be at resonance with multiphotonic absorption processes.

Multiphotonic resonances

Absorption of photons is resonantly enhanced when n incident laser photons have the same energy as n photons inside the cavity. In the case of the Kerr Hamiltonian considered so far, it means: $n\omega_p = n\omega_c + Un(n-1)/2$. Expressed in terms of the pump-cavity detuning, this relation reads:

$$\frac{U}{\Delta\omega} = \frac{2}{n-1}. \tag{2.24}$$

This energy matching condition can be satisfied for $n > 1$ only if $\Delta\omega > 0$. If the pump is resonant with the bare cavity frequency, i.e $\Delta\omega = 0$, only single photons can be absorbed resonantly. There is no relation between U and $\Delta\omega$ in this case and the density matrix is found by expanding the master equation in powers of F/U and γ/U. In the following, we will focus on the more interesting case of multiphotonic resonances ($n > 1$) and assume $\Delta\omega > 0$.

For simplicity, let us first look at the two-photon resonance ($U = 2\Delta\omega$). It appears that in the rotating frame, the vacuum $|0\rangle$ has the same energy as the two photon-state $|2\rangle$ in the absence of driving. This degeneracy is lifted by the coupling to the external field whose effect on the dynamics can be understood qualitatively in the following way. Suppose that at time $t = 0$ the intra-cavity field is in the vacuum state $|0\rangle$. Since the vacuum is no longer an eigenstate of the rotating-frame Hamiltonian, but a linear combination of eigenstates $\frac{1}{\sqrt{2}}(|0\rangle + |2\rangle)$ and $\frac{1}{\sqrt{2}}(|0\rangle - |2\rangle)$, the cavity field will start to oscillate between $|0\rangle$ and $|2\rangle$. These Rabi oscillations will take place until the occurrence of a quantum jump, due to cavity losses. After the emission of a first photon out of the cavity, the field is projected into the state $|1\rangle$ and it is only after the emission of a second photon that it returns to vacuum. In that sense, the two-photon absorption process results, as expected, in the emission of a photon "pair" out of the cavity. Since the single-photon state has a decay rate γ, the time between emission of photons from the same pair will be of the order of $1/\gamma$.

If the frequency splitting between the two quasi-degenerate eigenstates is much smaller than the dissipation rate, i.e. $F^2/\Delta\omega \ll \gamma$, the field will not have time to oscillate and will stay mostly in the vacuum state. In this low density regime, the average time required to absorb a photon pair is much larger that the single-photon decay time $1/\gamma$. Therefore, photons will appear strongly bunched when compared with coherent light of the same intensity.

The time between successive pairs decreases with decreasing dissipation and photon bunching eventually disappears for $F^2/\Delta\omega \gg \gamma$. We will see quantitatively in the following that the emitted light is even antibunched in this limit. Similar photon correlations

have also been predicted for the two-photon resonance of the Jaynes-Cummings model [84].

More quantitative results can be obtained by solving the master equation explicitly. To fully grasp the effect of the resonance, we will assume that $F/\Delta\omega \gg \gamma/\Delta\omega$. We will work is the basis formed by the eigenstates of the total Hamiltonian (up to the lowest order in $F/\Delta\omega$), given by:

$$|a\rangle = \frac{1}{\sqrt{2}}(|0\rangle + |2\rangle), \tag{2.25}$$

$$|b\rangle = \frac{1}{\sqrt{2}}(|0\rangle - |2\rangle), \tag{2.26}$$

$$|c\rangle = |1\rangle.$$

Since the driving term only couples Fock states $|m\rangle$ to $|m \pm 1\rangle$, the coupling of $|0\rangle$ and $|2\rangle$ is of order 2. The energies given by second-order perturbation theory are:

$$E_a \simeq \frac{F^2}{\Delta\omega}(1 + \sqrt{2}), \tag{2.27}$$

$$E_b \simeq \frac{F^2}{\Delta\omega}(1 - \sqrt{2}), \tag{2.28}$$

$$E_c \simeq -\Delta\omega. \tag{2.29}$$

As expected, the energy splitting between states $|a\rangle$ and $|b\rangle$ is proportional to $(F/\Delta\omega)^2$. In the "dressed-state" basis, the dissipative term of the master equation couples populations and coherences of the density matrix. However, in the lowest order in $F/\Delta\omega$ and $\gamma/\Delta\omega$, the coefficients ρ_{ac} and ρ_{bc} vanish. The master equation in this basis reads:

$$\partial_t \rho_{aa} = \gamma[\frac{1}{2}\rho_{cc} - \rho_{aa} + \frac{1}{2}(\rho_{ab} + \rho_{ba})], \tag{2.30}$$

$$\partial_t \rho_{bb} = \gamma[\frac{1}{2}\rho_{cc} - \rho_{bb} + \frac{1}{2}(\rho_{ab} + \rho_{ba})], \tag{2.31}$$

$$\partial_t \rho_{ab} = \Delta\omega[(-i2\sqrt{2}\frac{F^2}{\Delta\omega^2} - \frac{\gamma}{\Delta\omega})\rho_{ab} + \frac{\gamma}{2\Delta\omega}], \tag{2.32}$$

$$\partial_t \rho_{cc} = \gamma[\rho_{aa} + \rho_{bb} - \rho_{cc} - (\rho_{ab} + \rho_{ba})]. \tag{2.33}$$

The stationary value for ρ_{ab} is then:

$$\rho_{ab} = \frac{1}{2}\frac{1}{1 + \frac{i2\sqrt{2}F^2}{\gamma\Delta\omega}}, \tag{2.34}$$

giving:

$$\rho_{ab} + \rho_{ba} = \frac{1}{1 + \frac{8F^4}{\gamma^2\Delta\omega^2}} = \xi. \tag{2.35}$$

All the other coefficients along with the observables can be expressed as functions of the parameter ξ. Namely, we have:

$$\rho_{11} = \rho_{cc} = \frac{1}{2}(1-\xi), \tag{2.36}$$

$$\rho_{aa} = \rho_{bb} = \frac{1}{4}(1+\xi), \tag{2.37}$$

$$\rho_{22} = \frac{1}{2}(\rho_{aa}+\rho_{bb}) - \frac{1}{2}(\rho_{ab}+\rho_{ba}) = \frac{1}{4}(1-\xi). \tag{2.38}$$

Once we have computed the steady-state density matrix, relevant observables are readily accessible. As stated in the previous chapter, of particular interest are the mean photon density and $g^{(2)}(0)$. They are given by

$$\langle b^\dagger b\rangle = 1-\xi, \tag{2.39}$$

$$g^{(2)}(0) = \frac{1}{2(1-\xi)}. \tag{2.40}$$

Before discussing these results any further, let us mention that we have checked the validity of these two expressions by comparing them with exact formulas (obtained using a P-representation for the density matrix), that are to be presented in the next chapter. Anticipating these more general results, Fig.(2.2) shows the mean photon density and $g^{(2)}(0)$, plotted as a function of ξ for $F/\Delta\omega = 10^{-2}$. In order to stay in the domain of validity of Eqs.(2.39) and (2.40), $\gamma/\Delta\omega$ is ranging from $\frac{F^2}{10\Delta\omega^2}$ to $\frac{F}{5\Delta\omega}$. In these conditions, the approximations underlying the derivation are justified and the above expressions are very accurate.

Let us now look at the two limits $\frac{F^2}{\gamma\Delta\omega} \ll 1$ and $\frac{F^2}{\gamma\Delta\omega} \gg 1$. They correspond to $\xi \to 1$ and $\xi \to 0$ respectively. In the first case, the photon density goes to zero as expected, and $g^{(2)}(0)$ diverges. In the other limit, the field is in a statistical mixture of three states and the density matrix in Fock space is:

$$\rho = \frac{1}{4}|0\rangle\langle 0| + \frac{1}{2}|1\rangle\langle 1| + \frac{1}{4}|2\rangle\langle 2|. \tag{2.41}$$

The photon density is then equal to one and $g^{(2)}(0) = 0.5$. Note that these results are consistent with the qualitative picture outlined at the beginning of this section. The emission of photon pairs manifests itself through photon superbunching in the low-density regime (limit $\frac{F^2}{\gamma\Delta\omega} \ll 1$), and through photon antibunching for higher density (limit $\frac{F^2}{\gamma\Delta\omega} \gg 1$). Furthermore, the state obtained for $\xi \to 0$ is highly nonclassical and the closest to a Fock state that one can hope for in this context.

This study of the two-photon resonance also shows that one must be careful in discussing the limit $\frac{F}{\Delta\omega}, \frac{\gamma}{\Delta\omega} \ll 1$ as the system behavior varies qualitatively depending on the ratio $\frac{F^2}{\gamma\Delta\omega}$.

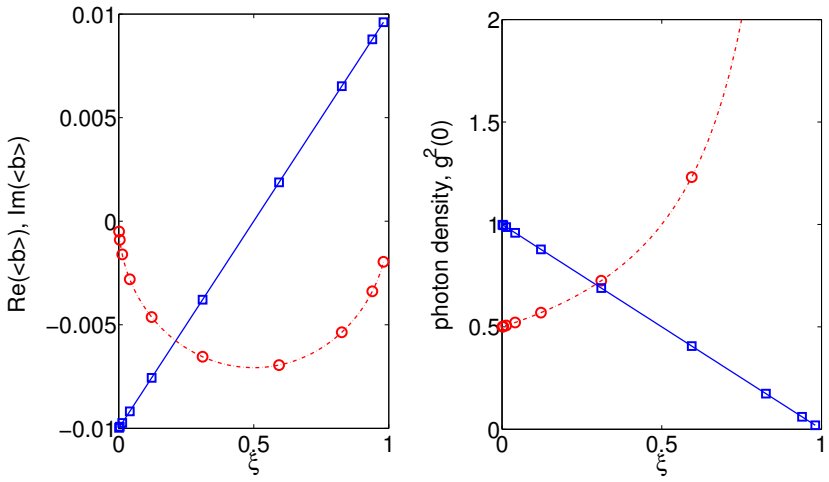

Figure 2.2: Results for a single cavity. Left panel: real (continuous blue line) and imaginary part (dotted-dashed red line), of the bosonic coherence $\langle b\rangle$ plotted vs ξ for $F/\Delta\omega = 10^{-2}$. The corresponding values of $\gamma/\Delta\omega$ range from $\frac{F^2}{10\Delta\omega^2}$ to $\frac{F}{5\Delta\omega}$. Lines are the result of exact P-representation calculations while markers correspond to the simplified expression of Eq.(2.81). Right panel: mean photon density $\langle b^\dagger b\rangle$ (continuous blue line) and $g^{(2)}(0)$ (red dashed-dotted line), vs. ξ. Same conditions and conventions as in the other panel.

As one might expect, these results are not limited to $n = 2$. The next paragraph is devoted to the general case with $n > 2$.

Generalized Fock states

In the case of n-photon resonance, the coupling between $|0\rangle$ and $|n\rangle$ is of the order n in F and the energy splitting proportional to $F^n/\Delta\omega^{n-1}$. In what follows we show that a state similar to Eq.(2.41) may be obtained in the limit $\frac{F^n}{\gamma\Delta\omega^{n-1}} \gg 1$.

The first thing to notice is that for $n > 2$, not only are the two states $|0\rangle$ and $|n\rangle$ degenerate in the absence of driving, but it is also true for all the states $|k\rangle$, $|q\rangle$ with $k + q = n$. Instead of the two states $|a\rangle$ and $|b\rangle$ of Eq.(2.25), we have several pairs $|a_k\rangle$, $|b_k\rangle$ mixing $|k\rangle$ and $|n-k\rangle$. Before writing an explicit expression for the master equation in the dressed basis, a few conclusions on the general structure of the equations can be drawn solely from the fact that the Hamiltonian is diagonal in this basis.

In particular, generalizing Eqs.(2.30-2.33), we can write the master equation in the

dressed basis in the following way:

$$i\partial_t \rho_{jj} = \gamma \sum_{pq} \alpha^j_{pq} \rho_{pq}, \tag{2.42}$$

$$i\partial_t \rho_{ij} = (E_i - E_j)\rho_{ij} + \gamma \sum_{pq} \beta^{ij}_{pq} \rho_{pq}, \tag{2.43}$$

where $i, j, p, q \in \{a_1, b_1, a_2, b_2 \dots a_k, b_k \dots\}$, E_i,E_j are the energy levels of the rotating-frame Hamiltonian and α^j_{pq}, β^{ij}_{pq} are generic coefficients. From the second equation we conclude that coherences vanish in the steady-states. Indeed the smallest value for $E_i - E_j$ is the energy splitting between eigenstates inside the subspace $\{|0\rangle, |n\rangle\}$. As a consequence, in the limit $\frac{F^n}{\gamma \Delta \omega^{n-1}} \gg 1$, the difference $E_i - E_j$ is always much larger than γ and the stationary value for ρ_{ij} goes to zero.

Taking this last result into account, the only stationary equations that remain to be solved contain only populations and may be written as:

$$\sum_q \alpha^j_{qq} \rho_{qq} = 0. \tag{2.44}$$

Notice that in this expression, neither γ nor F appears explicitly.

To go further we need to find the coefficients α^j_{qq}, which depend on the basis $\{|a_k\rangle, |b_k\rangle\}$. In the following we show that the expression for the two-photon resonance can be readily extended to the general case. Namely, the perturbed eigenstates, up to the lowest order in F, are:

$$|a_k\rangle = \frac{1}{\sqrt{2}}(|k\rangle + |n-k\rangle), \tag{2.45}$$

$$|b_k\rangle = \frac{1}{\sqrt{2}}(|k\rangle - |n-k\rangle), \tag{2.46}$$

for k integer and $0 \leq k \leq n/2$.

In its general formulation the problem of finding these eigenstates is solved by means of time-independent perturbation theory with degenerate levels. To find energies, and the corresponding eigenstates, one has to solve the so-called secular equation in each of the degenerate subspaces [85]. More precisely, the energies are solutions of:

$$\det[EP - h_{eff}(E)] = 0, \tag{2.47}$$

where P is the projector onto the considered subspace and h_{eff} is the effective Hamiltonian inside the subspace, given by:

$$h_{eff} = PHP + PVQ\frac{Q}{EQ - HQ}QVP. \tag{2.48}$$

Here we have introduced the projector $Q = 1 - P$, and the perturbation operator $V = F(b^\dagger + b)$. We do not need to solve Eq.(2.47) completely to find the expression for the eigenstates. In particular, it is sufficient for our purpose to show that the effective Hamiltonian for each subspace has the form:

$$h_{eff} = \begin{pmatrix} D & g \\ g & D \end{pmatrix}. \tag{2.49}$$

Indeed, such a matrix has eigenvectors similar to those of Eqs.(2.45)-(2.46).

Since the unperturbed Hamiltonian has only real matrix elements and F is assumed to be real, h_{eff} is a real matrix. It is also symmetric by definition. The only thing left to do is therefore to show that the two diagonal elements are equal. We are only interested in the leading terms in the expansion in powers F, which for the diagonal elements D_k and D_{n-k} are of second order and given by [86]:

$$\begin{aligned} D_k &= \sum_{n \neq k} \frac{|\langle k|V|n\rangle|^2}{E_k^{(0)} - E_n^{(0)}} \\ &= \frac{(k+1)F^2}{\Delta\omega - kU} + \frac{kF^2}{-\Delta\omega + (k-1)U}. \end{aligned} \tag{2.50}$$

Recalling the energy matching condition: $U/\Delta\omega = 2/(n-1)$ we find:

$$D_k = \frac{-(n+1)F^2}{\Delta\omega(n-2k-1)(2k-n-1)}, \tag{2.51}$$

which satisfies the symmetry condition:

$$D_k = D_{n-k}, \tag{2.52}$$

thereby showing that the effective Hamiltonian is of the form of Eq.(2.49). From this we conclude that the eigenstates of the full Hamiltonian, in the lowest order in F, are given by Eq.(2.45) and Eq.(2.46).

The last step is to write an explicit equation for stationary populations in the basis $\{|a_k\rangle, |b_k\rangle, \dots\}$. For simplicity, we will assume that n is odd, so that there is no non-degenerate singlet, but the same reasoning is valid also for even values of n. Projecting the master equation in the dressed basis and assuming that coherences vanish, we find:

$$n\rho_{a_k a_k} - \frac{k+1}{2}(\rho_{a_{k+1}a_{k+1}} + \rho_{b_{k+1}b_{k+1}}) - \frac{n-k+1}{2}(\rho_{a_{k-1}a_{k-1}} + \rho_{b_{k-1}b_{k-1}}) = 0 \tag{2.53}$$

$$n\rho_{b_k b_k} - \frac{k+1}{2}(\rho_{a_{k+1}a_{k+1}} + \rho_{b_{k+1}b_{k+1}}) - \frac{n-k+1}{2}(\rho_{a_{k-1}a_{k-1}} + \rho_{b_{k-1}b_{k-1}}) = 0 \tag{2.54}$$

In this form, these equations are valid from $k = 0$ to $k = \frac{n-1}{2} - 1$. A last equation is provided by the normalization condition $\mathrm{Tr}[\rho] = 1$. We see that a_k and b_k play symmetric roles for all k. We have therefore:

$$\rho_{a_k a_k} = \rho_{b_k b_k} \tag{2.55}$$

After this simplification, we are left with only one recurrence relation. The solution, up to a normalization constant, is provided by the binomial coefficients:

$$\rho_{a_k a_k} = \rho_{b_k b_k} = \frac{1}{2^n} \frac{n!}{k!(n-k)!} = \frac{1}{2^n} \binom{n}{k}. \tag{2.56}$$

Since all non-diagonal coefficients of the density matrix vanish in the dressed basis, the populations in Fock space are given by:

$$\langle k|\rho|k\rangle = \frac{1}{2}(\rho_{a_k a_k} + \rho_{b_k b_k}) = \frac{1}{2^n} \binom{n}{k}. \tag{2.57}$$

Besides, it is clear that coherences between state $|n\rangle$ and $|m\rangle$ that do not belong to the same subspace will vanish. As for coherences between $|k\rangle$ and $|n-k\rangle$, we have:

$$\langle k|\rho|n-k\rangle = \frac{1}{2}(\rho_{a_k a_k} - \rho_{b_k b_k}) = 0. \tag{2.58}$$

Hence, the density matrix is also diagonal in Fock space.

In conclusion, a state similar to Eq.(2.41) may be obtained in the limit $\frac{F^n}{\gamma \Delta\omega^{n-1}} \gg 1$ and the corresponding density matrix is:

$$\rho^{(n)} = \frac{1}{2^n} \sum_{k=0}^{n} \binom{n}{k} |k\rangle\langle k|. \tag{2.59}$$

The state of Eq.(2.59) is characterized by:

$$\langle b^\dagger b\rangle = \frac{n}{2}, \tag{2.60}$$

$$g^{(2)}(0) = 1 - \frac{1}{n}. \tag{2.61}$$

Note that the value of $g^{(2)}(0)$ is the same as in the n^{th}-lobe of the equilibrium model (pure Fock state with n photons). For this reason, we have called the mixed states of Eq.(2.59) "generalized Fock states". From the point of view of photon statistics, these states are non-classical. However, their Wigner function has no negative part, as we will see in the following. Before getting into the details of Wigner function calculations, we emphasize that Eq.(2.59-2.61) also apply to $n = 1$ ($\Delta\omega = 0$), in the limit $F/U \to 0$ and $\gamma/F \to 0$.

The Wigner transform is a way to map quantum mechanical Hermitian operators to real functions in phase space. When applied to the density matrix it gives the Wigner function. This function is a quasi-probability distribution over phase space. The occurrence of negative values is usually associated with "quantumness". the Wigner function is defined as follows [87]:

$$W(\beta) = \frac{1}{\pi}\mathrm{Tr}[\rho D(\beta)(-1)^{b^\dagger b} D(\beta)^{-1}], \tag{2.62}$$

where $D(\beta)$ is the displacement operator, which transforms the vacuum state $|0\rangle$ into a coherent state $|\beta\rangle$:

$$D(\beta)|0\rangle = e^{(\beta b^\dagger - \beta^* b)}|0\rangle = |\beta\rangle. \tag{2.63}$$

Defined in this way, the Wigner function satisfies the normalization condition:

$$\int W(\beta) d^2\beta = 1. \tag{2.64}$$

We see from Eq.(2.62) that the Wigner transform is linear in ρ. Since the density matrix $\rho^{(n)}$ in Eq.(2.59) is a linear combination of pure Fock states, its Wigner function is a linear combination of Fock states' Wigner functions. The Wigner function of a Fock state with n photons is given by [88]:

$$W(\beta) = \frac{2}{\pi}(-1)^n L_n(4|\beta|^2) e^{-2|\beta|^2}, \tag{2.65}$$

with $L_n(x)$ the n^{th} Laguerre polynomial:

$$L_n(x) = \sum_{k=0}^{n} (-1)^k \binom{n}{k} \frac{x^k}{k!}. \tag{2.66}$$

The Wigner function of $\rho^{(n)}$ is therefore of the form $\frac{2}{\pi} e^{-2|\beta|^2} P(4|\beta|^2)$, with P the polynomial:

$$P(x) = \frac{1}{2^n} \sum_{k=0}^{n} \sum_{q=0}^{k} (-1)^{k+q} \binom{n}{k} \binom{k}{q} \frac{x^q}{q!}. \tag{2.67}$$

Inverting the two summations and writing binomials coefficients explicitly we find:

$$P(x) = \frac{1}{2^n} \sum_{q=0}^{n} (-1)^q \frac{x^q}{q!} \sum_{k=q}^{n} (-1)^k \frac{n!}{(n-k)!(k-q)!q!}. \tag{2.68}$$

This last expression can be simplified by rewriting the sum over k as a sum over $k' = n - k$. The binomial coefficients $\binom{n}{q}$ and $\binom{n-q}{k'}$ naturally arise in the process and we get:

$$P(x) = \frac{1}{2^n} \sum_{q=0}^{n} (-1)^{n+q} \binom{n}{q} \frac{x^q}{q!} \sum_{k'=0}^{q} (-1)^{k'} \binom{n-q}{k'}. \tag{2.69}$$

The second sum, over k', is non zero only if $q = n$. $P(x)$ then reduces to a single monomial and its final expression is:

$$P(x) = \frac{x^n}{2^n n!}. \tag{2.70}$$

The Wigner function for $\rho^{(n)}$ is then:

$$W(\beta) = \frac{2^{n+1}|\beta|^{2n}}{\pi n!} e^{-2|\beta|^2}. \tag{2.71}$$

Note that this function has its maximum for $|\beta|^2 = n/2$, which is consistent with the fact that the mean photon number is $n/2$ in such a state. An interesting property of Eq.(2.71) is that it is always positive. The effect of the statistical mixture is to suppress all the negative values present in each of the individual Fock states' Wigner functions. Interestingly these states are quantum in terms of photon statistics ($g^{(2)}(0) < 1$) but their Wigner function does not take negative values. An example of Wigner function for pure and generalized Fock states is shown on Fig.(2.3).

Driving out of multiphotonic resonances.

In the case where multiphotonic absorption processes are non resonant, the mean photon number is expected to be very low. In such conditions, the density matrix can be approximated to lowest order in $F/\Delta\omega$ by a pure state [89]:

$$\rho = |\psi\rangle\langle\psi|, \tag{2.72}$$

with:

$$|\psi\rangle = \sum_n c_n |n\rangle. \tag{2.73}$$

Both $F/\Delta\omega$ and $\gamma/\Delta\omega$ are assumed to be much smaller than one, but it is not necessary to impose $F \gg \gamma$. The following treatment is still valid if $F/\Delta\omega$ and $\gamma/\Delta\omega$ are of the same order of magnitude. Keeping the lowest order in $F/\Delta\omega$ and $\gamma/\Delta\omega$ for the coefficients c_n, we obtain the following relation:

$$c_n = \frac{F/\Delta\omega\sqrt{n}c_{n-1}}{n - \frac{n(n-1)}{2}\frac{U}{\Delta\omega} + \frac{in\gamma}{2\Delta\omega}}. \tag{2.74}$$

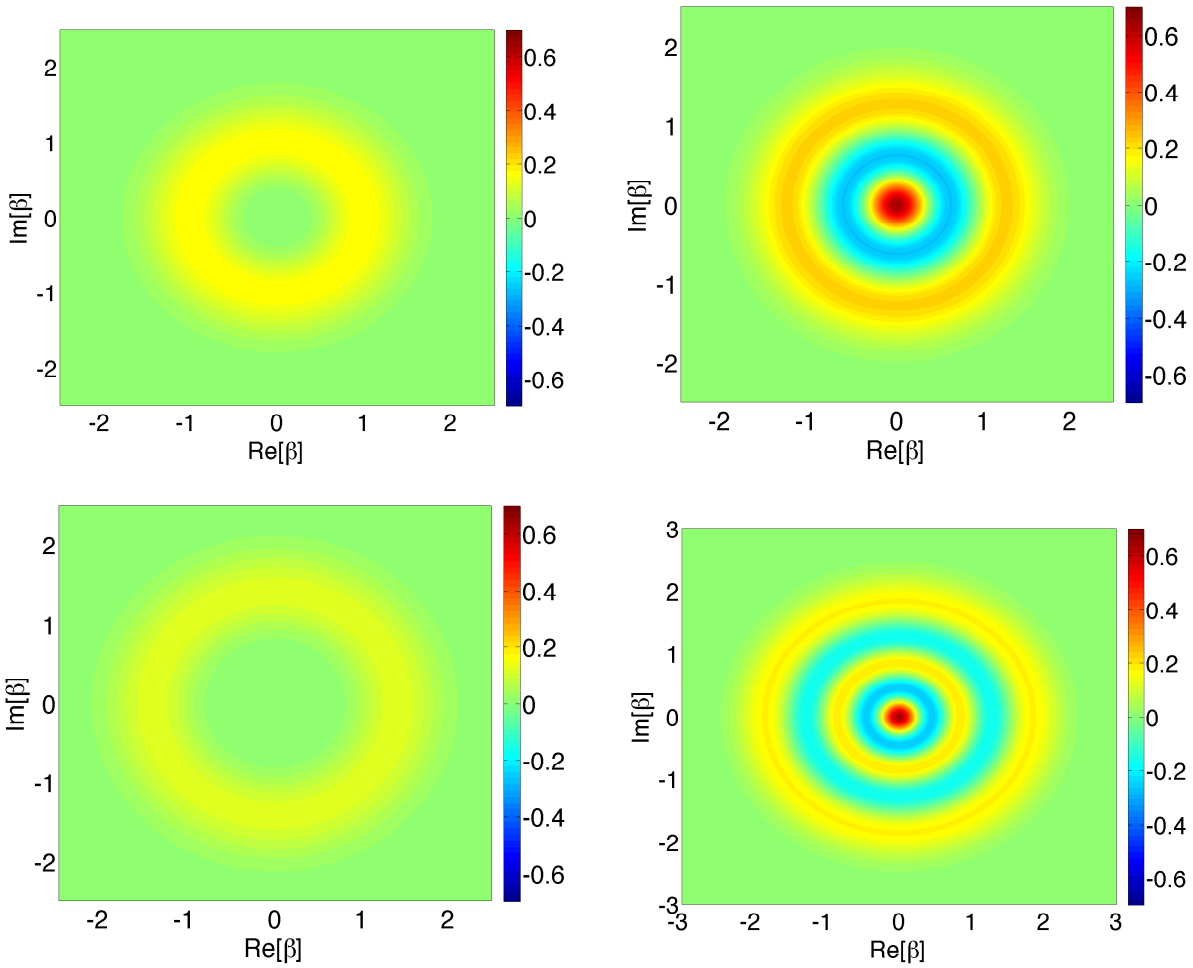

Figure 2.3: Wigner function of Fock states (right) and generalized Fock states (left), for $n = 2$ (top) and $n = 4$ (bottom). Contrary to pure Fock states, the Wigner function of generalized Fock states do not take negative values, even though $g^{(2)}(0) < 1$.

Neglecting the probability of having 3 or more photons inside the cavity, we find:

$$c_0 = 1, \tag{2.75}$$

$$c_1 = \frac{F}{\Delta\omega}(1 - \frac{i\gamma}{2\Delta\omega}), \tag{2.76}$$

$$c_2 = \frac{\sqrt{2}(F/\Delta\omega)^2}{2 - U/\Delta\omega}(1 - \frac{i\gamma}{2\Delta\omega}\frac{4 - U/\Delta\omega}{2 - U\Delta\omega}). \tag{2.77}$$

Eq.(2.75) stems from the normalization condition while the two other equations follow directly from Eq.(2.74).

From this we can compute the mean photon density and the second-order autocorrelation function:

$$\langle b^\dagger b\rangle = \left(\frac{F}{\Delta\omega}\right)^2, \tag{2.78}$$

$$g^{(2)}(0) = \frac{4}{(2 - U/\Delta\omega)^2}. \tag{2.79}$$

As expected, when the system becomes linear, i.e. $U \to 0$, the cavity is driven into a coherent state ($g^{(2)}(0) = 1$). However, the on-site interaction induces large fluctuations in the photon statistics when the two-photon absorption process becomes resonant ($U/\Delta\omega = 2$).

2.2.2 Coupled cavities: Mean-field solution

Now that we have a good understanding of the single-cavity dynamics, it is time to include tunneling of photons between neighboring cavities. We have seen that within the mean-field approximation, the coupling between sites is treated as a source term in an effective single-site Hamiltonian. For the driven-dissipative model, it means that the pump intensity F (which acts as a source term), is to be replaced with an effective one:

$$F \to F' = F - J\langle b\rangle. \tag{2.80}$$

Injected into the single-site expression for $\langle b\rangle$, this substitution yields the mean-field self-consistent equation.

Let us first go back to the two-photon resonance. The analytical expression for the bosonic coherence in this regime is:

$$\langle b\rangle = \frac{F}{\Delta\omega}(2\xi - 1) + i\frac{\gamma}{2F}(\xi - 1). \tag{2.81}$$

A plot of this function and a comparison with the exact general formula is shown in Fig.(2.2). Since ξ is also a function of F, the self-consistent equation stemming from Eq.(2.81) is difficult

to solve analytically in its general form. For $\xi \to 0$, however, the imaginary part can be neglected and we are left with the simple expression:

$$\langle b \rangle = -\frac{F}{\Delta\omega}. \tag{2.82}$$

The substitution $F \to F - J\langle b \rangle$ then gives:

$$\langle b \rangle = \frac{-F/\Delta\omega}{1 - J/\Delta\omega}. \tag{2.83}$$

This shows that the coupling between sites amounts to replacing F with $F' = \frac{F}{1-J/\Delta\omega}$. In other words, the effective pump is enhanced by the coupling between cavities. As a result, the system is driven into the $\xi = 0$ state and will stay there as long as the approximation $F'/\Delta\omega \ll 1$ holds. Results for different values of ξ are presented on Fig.(2.4). When $J/\Delta\omega \sim 1$ the above treatment ceases to be valid because $F' \sim \Delta\omega$, and the system enters another regime. Exact P-representation calculations show that the mean photon density starts to increase with J, while $g^{(2)}(0)$ goes to 1, thus indicating a crossover from a quantum state to a classical coherent one (see Fig.(2.4)). As we shall see in section 3.2.4, this idea is confirmed by the fact that the linear asymptotic behavior of $\langle b \rangle$ as a function of J visible on Fig.(2.4), corresponds to Gross-Pitaevski semi-classical predictions.

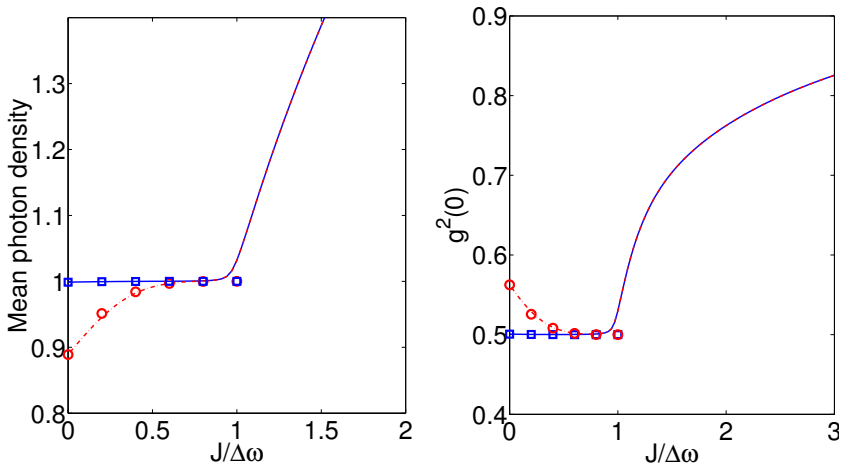

Figure 2.4: Two-photon resonance. Mean photon density and $g^{(2)}(0)$ as a function of the tunneling amplitude $J/\Delta\omega$ for $F/\Delta\omega = 10^{-2}$. The values of $\gamma/\Delta\omega$ are $\frac{F^2}{10\Delta\omega^2}$ (continuous blue line) and $\gamma/\Delta\omega = \frac{F^2}{\Delta\omega^2}$ (red dotted-dashed line). The lines show P-representation calculations and the markers the results of Eq.(2.83).The effect of coupling J is to drive the system into the state of Eq.(2.41), until the critical coupling $J_c = \Delta_\omega$ is reached.

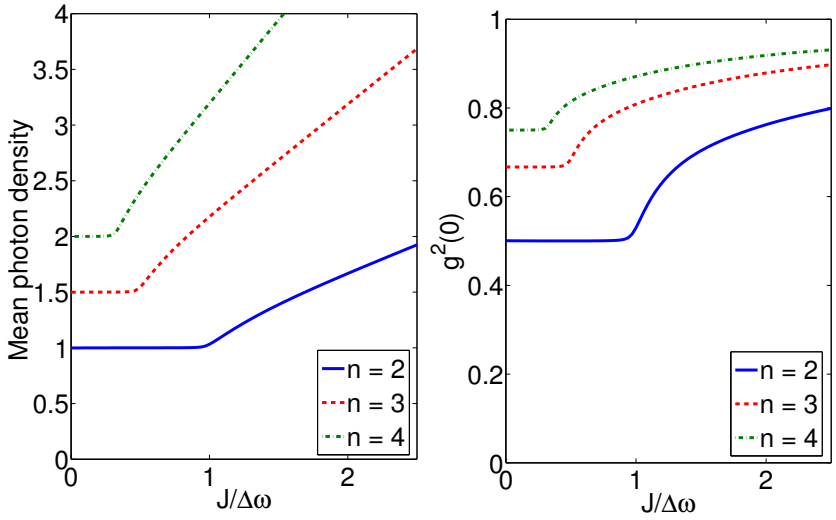

Figure 2.5: Quantum-to-classical crossover for $n = 2$ (continuous blue line), $n = 3$ (red dashed line), and $n = 4$ (green dotted-dashed line). The mean photon density and $g^{(2)}(0)$ are plotted as a function of the tunneling amplitude $J/\Delta\omega$ for $F/\Delta\omega = 10^{-2}$ and $F^n/(\Delta\omega^{n-1}\gamma) = 10$. The system stays in the state of Eq.(2.59) until a critical coupling $J_c = \Delta\omega/(n-1)$, after which it is driven towards a coherent state.

Once again, this can be extended to larger values of n. For the n-photon resonance in the limit $\frac{F^n}{\gamma\Delta\omega^{n-1}} \ll 1$, Eq.(2.82) for a single cavity becomes:

$$\langle b\rangle = -(n-1)\frac{F}{\Delta\omega}. \tag{2.84}$$

When the coupling between cavities in switched on, $\langle b\rangle$ is given by:

$$\langle b\rangle = \frac{-(n-1)F/\Delta\omega}{1-(n-1)J/\Delta\omega}, \tag{2.85}$$

which means that the system will stay in the state Eq.(2.59) until $J/\Delta\omega \sim 1/(n-1)$. As in the case of two-photon resonance, exact P-representation calculations presented on Figs.(2.5) and (2.6) show a crossover to a classical coherent state. This crossover is the closest equivalent, in this driven dissipative system, of the equilibrium Mott-insulating to superfluid phase transition. We emphasize that the phase of $\langle b\rangle$ is imposed by the pump, but the amplitude $|\langle b\rangle|$ is spontaneous: it becomes finite in the classical regime even though $F \to 0$ (see Fig.(2.6)).

Out of multiphotonic resonances, the coupling between cavities has a different effect. In this regime, the system is in a state described by Eqs.(2.75)-(2.77) at $J = 0$. The bosonic coherence is then:

$$\langle b\rangle = \frac{F}{\Delta\omega}. \tag{2.86}$$

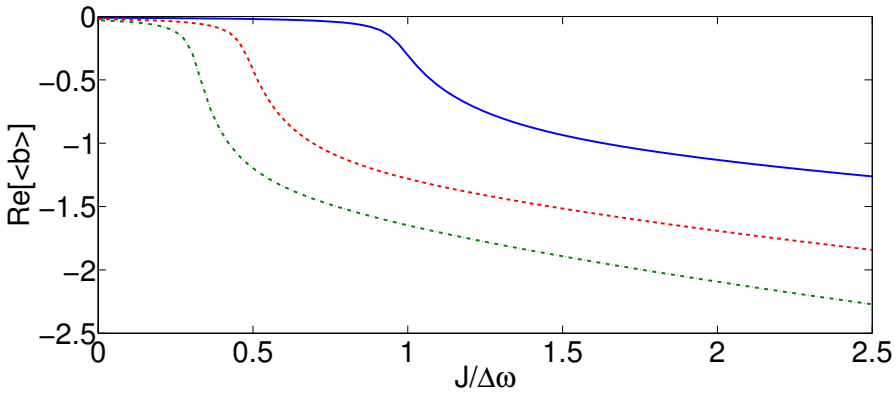

Figure 2.6: Quantum-to-classical crossover, seen from the value of the bosonic coherence $\langle b \rangle$, plotted as a function of $J/\Delta\omega$. Same parameters as in Fig.(2.5). In the quantum regime, $\langle b \rangle$ is very small ($\sim F/\Delta\omega$), and becomes large in the classical regime. Note that $\mathrm{Im}[\langle b \rangle] \sim \gamma/\Delta\omega \ll \mathrm{Re}[\langle b \rangle]$.

At finite J, it becomes:

$$\langle b \rangle = \frac{F/\Delta\omega}{1 + J/\Delta\omega}, \tag{2.87}$$

and the effective pump is given by $F \to F' = \frac{F}{1+J/\Delta\omega}$. Contrary to Eq.(2.85), the intensity of F' decreases with J. As a consequence, the system will remain in a state qualitatively similar to Eqs.(2.75)-(2.77) and no crossover occurs.

2.3 Conclusion

In investigating the limit of weak pumping and weak dissipation, we have shown that within a mean-field approach, the closest equivalent of the equilibrium Mott-insulator-to-superfluid transition is found when the external laser frequency is tuned so as to be at resonance with a n-photon absorption process. Moreover, if the pumping intensity is such that $\frac{F^n}{\gamma\Delta\omega^{n-1}} \gg 1$, the system is driven, on each lattice site, into a statistical mixture of Fock states that have the same value of $g^{(2)}(0)$ as a pure Fock state with n photons but a mean photon density of $n/2$. It stays in such a mixed state, which can be viewed as an driven-dissipative equivalent of a Mott insulator, until the coupling between sites reaches a critical value. Beyond this value a crossover to a coherent state, reminiscent of the superfluid side of the transition, occurs. In this regime the mean photon density increases with increasing tunneling and $g^{(2)}(0)$ goes to 1.

Outside of these multiphotonic resonances, the mean-photon density is much smaller than 1 and the state of the system is not as much affected by the coupling strength J, its effect being mainly to reduce the effective intensity of the pump. As a result, the photon statistics is determined primely by the ratio $U/\Delta\omega$. Photons are antibunched in the regime of photon blockade ($U/\Delta\omega \gg 1$) but strongly bunched in the vicinity of the two-photon resonance ($U/\Delta\omega \to 2$).

These considerations encourage to distinguish between two types of steady-state phases. The first one is a "high-density phase", with $g^{(2)}(0) \leq 1$ and a mean-photon density increasing with the tunneling rate. The second one is a "low-density phase" with $\langle b^\dagger b \rangle \ll 1$ and possibly large fluctuations in the photon statistics. We will see in the next chapter that these general characteristics of the steady-states remain visible at higher pumping and dissipation.

Chapter 3

Mean-field phase diagram of the driven-dissipative Bose-Hubbard model

In the previous chapter, we addressed the issue of driving and dissipation by solving the master equation in the Fock basis or in a dressed basis with only a few photons per site. This approach, which enabled us to derive analytical expressions for the single-site and mean-field density matrix, is well suited for weak pumping, when the mean number of photons inside the cavity is small. It is not efficient however, if a large number of Fock states per cavity must be taken into account. In this chapter, we will consider another method based on a coherent-state representation of the density matrix, which turns out to be much more powerful.

We begin by a few general considerations on how to use the coherent-state basis to represent operators and density matrices. Building up on the relative freedom in the choice of a representation given by the overcompleteness of the basis, we introduce a series of representations, known as "generalized P-representations". We will see that the main advantage of these representations is that they provide a way to map the operatorial master equation into the better-known Fokker-Planck equation. As shown by Drummond and Walls [90], generalized P-representations provide a general solution to the problem of a single nonlinear cavity.

By applying this exact result to mean-field theory, we are able to compute the phase diagram in the general case of arbitrary pumping and dissipation. One of the important features of the mean-field phase diagram is the appearance of bistability induced by the coupling between the cavities. For some values of the tunneling coefficient, several solutions of the self-consistent mean-field equation are found. We will see that many of the results obtained in the previous chapter, in particular those regarding the role of multiphotonic

resonances, are still relevant for the understanding of the steady-state phases at higher pumping and dissipation.

We then go further in our investigation of the phase diagram by studying the stability of the different solutions and their collective excitations. We compute the dispersion relation by linearizing the master equation around the mean-field steady state. This "generalized Bogoliubov approach" enables us to identify tunneling-induced instabilities in the phase diagram, signaling the breaking of translational symmetry in the lattice. Indeed, in certain regions of the parameter space, no stable homogeneous mean-field solutions have been found.

Throughout the chapter, P-representation calculations are compared with results obtained using a Gross-Pitaevskii (semi-classical) approach.

For the most part, the work presented in this chapter has been published in Ref.[23]. The comparison with the Gross-Pitaevskii approximation is included in Ref.[22].

3.1 Phase-space approach to quantum optics

Given the role that they play in the theoretical formulation of quantum optics, the set of coherent states seems a natural alternative to the Fock basis. As seen in Chap.1, their expression in Fock space is:

$$|\alpha\rangle = e^{-|\alpha|^2/2} \sum_{n=0}^{\infty} \frac{\alpha^n}{\sqrt{n!}} |n\rangle. \tag{3.1}$$

3.1.1 Coherent-state representation of the density matrix

The general problem of finding an expression for the density matrix in terms of coherent-state projection operators may be formulated in the following way: find a function $\mathcal{F}(\alpha, \beta)$ and an appropriate domain $\mathcal{D} \subset \mathbb{C}^2$ such that

$$\rho = \int\int_{\mathcal{D}} \mathcal{F}(\alpha, \beta) |\alpha\rangle\langle\beta^*| \mathrm{d}^2\alpha \mathrm{d}^2\beta. \tag{3.2}$$

If the basis were not overcomplete, such a function $\mathcal{F}(\alpha, \beta)$ would be unique and equal to the matrix elements of ρ in this basis: $\langle\alpha|\rho|\beta^*\rangle$. Besides, the integral would run over the whole space $\mathbb{C}^2$. However, as we have seen, coherent states are not orthogonal and thus the problem of finding $\{\mathcal{F}(\alpha, \beta), \mathcal{D}\}$ is not trivial. A consequence of the basis' overcompletness is that the set of all matrix elements $\langle\alpha|\rho|\beta^*\rangle$ contains a lot of redundant information. In fact, it can be shown that, in this basis, the density matrix is already entirely determined by its diagonal elements. To see this more clearly, let us write those matrix elements as

$$\langle\alpha|\rho|\alpha\rangle = \sum_{n,m} \langle n|\rho|m\rangle e^{-|\alpha|^2} \frac{(\alpha^*)^n (\alpha)^m}{\sqrt{n!m!}}. \tag{3.3}$$

We deduce from this expression that $e^{\alpha\alpha^*}\langle\alpha|\rho|\alpha\rangle$ acts as a kind of generating series for the matrix elements in Fock space. We find therefore:

$$\langle n|\rho|m\rangle = \frac{1}{\sqrt{n!m!}} \frac{\partial^n}{\partial\alpha^{*n}} \frac{\partial^m}{\partial\alpha^m} (e^{\alpha\alpha^*}\langle\alpha|\rho|\alpha\rangle)\Big|_{\alpha=0}. \tag{3.4}$$

Coming back to the task of finding $\{\mathcal{F}(\alpha, \beta), \mathcal{D}\}$, this last result suggests to look for a representation based only on diagonal projection operators:

$$\rho = \int P_{\mathrm{GS}}(\alpha, \alpha^*) |\alpha\rangle\langle\alpha| \mathrm{d}^2\alpha. \tag{3.5}$$

This is the Glauber-Sudarshan P-representation, introduced by Glauber and Sudarshan [91, 92]. It was shown to exist for all density operators but is not necessarily regular. In general

it is expressed in terms of singular distributions such as successive derivatives of the Dirac distribution [88]. An example of such singular P function is given by the coherent states themselves, since the P representation of a coherent state $|\alpha_0\rangle$ is:

$$P_{\mathrm{GS}}(\alpha, \alpha^*) = \delta(\alpha - \alpha_0). \tag{3.6}$$

At this point, it is important to keep in mind that the ultimate aim is for the representation of ρ to provide a efficient "encoding" of the system's dynamics. More precisely, in the same way that, projected into Fock space, the master equation yields a set of differential equations for the matrix elements in this basis, the same master equation will result in an equation of motion for the function $\mathcal{F}(\alpha, \beta)$. In this regard, the singularity of the Glauber-Sudarshan representation appears as an important drawback.

Although it may seem more "economical" in terms of information to work only with diagonal matrix elements, it is not the only alternative. In order to make the best of the relative freedom in the choice of the function $\mathcal{F}$, Drummond and Gardiner have proposed a more systematic scheme of defining representations by expanding ρ in terms of nondiagonal coherent-state projection operators [93]. Their "generalized P-representations" are of the form:

$$\rho = \int P(\alpha, \beta)\Lambda(\alpha, \beta) d\mu(\alpha, \beta), \tag{3.7}$$

where $\Lambda(\alpha, \beta)$ is a projection operator:

$$\Lambda(\alpha, \beta) = \frac{|\alpha\rangle\langle\beta^*|}{\langle\beta^*|\alpha\rangle}, \tag{3.8}$$

and $d\mu(\alpha\beta)$ the integration measure, whose choice will determine the different types of representation. As a first example, let us consider:

$$d\mu(\alpha, \beta) = \delta(\alpha - \beta^*) d^2\alpha d^2\beta. \tag{3.9}$$

We recover in this case the Glauber-Sudarshan P-representation defined in Eq.(3.5).

Complex P-representation

The complex P-representation is defined by

$$d\mu(\alpha, \beta) = \mathrm{d}\alpha\mathrm{d}\beta, \tag{3.10}$$

where α and β are two complex variables that are to be integrated on individual contours $\mathcal{C}_\alpha$ and $\mathcal{C}_\beta$. In such a representation, ρ is therefore written as:

$$\rho = \int_{\mathcal{C}_\beta} \int_{\mathcal{C}_\alpha} P(\alpha, \beta) \frac{|\alpha\rangle\langle\beta^*|}{\langle\beta^*|\alpha\rangle} \mathrm{d}\alpha \mathrm{d}\beta. \tag{3.11}$$

Positive P-representation

Another useful representation is obtained for:

$$d\mu = d^2\alpha d^2\beta, \tag{3.12}$$

allowing α and β to vary over the whole complex plane. One of the advantages of this representation is that it can always be chosen positive and thus be interpreted as a genuine probability distribution over a complex phase space (α, β). More precisely, it can be shown that its relation to matrix elements of ρ is [88]:

$$P(\alpha, \beta) = \frac{1}{4\pi^2} e^{\frac{-|\alpha-\beta|^2}{4}} \langle \frac{1}{2}(\alpha + \beta^*)|\rho|\frac{1}{2}(\alpha + \beta^*)\rangle, \tag{3.13}$$

which constitutes another proof that a density operator is entirely determined by coherent states diagonal matrix elements.

3.1.2 Fokker-Planck equations for generalized P-representations

One of the most interesting features of these coherent-state representations is that when the dynamics is described by the usual quantum optical master equation, the equation of motion obtained for $P(\alpha, \beta)$ takes the form of a Fokker-Planck equation. In this respect, the use of coherent-state representation has often been seen as establishing a quantum-to-classical correspondence, in the sense that the quantum master equation is mapped to the classical problem of diffusion in phase space. Note however that depending on the Hamiltonian, this equation may contain terms of higher order than the usual Fokker-Planck equation and may not be exactly solvable. The choice of representation is in fact dictated by the specific form of the resulting equation. For each of the representations, it is possible to build a "translation table" which indicates how to convert operators acting on ρ to differential operators acting on $P(\alpha, \beta)$.

Details of the derivation will be given only for the complex P-representation, since it will be the only one needed to solve the single cavity problem, but the procedure is essentially

the same for the other representations. The first step is to find the action of the creation and annihilation operators on the projectors $\Lambda(\alpha, \beta)$. It is most easily done by using unnormalized coherent states (also known as Bargmann states):

$$||\beta\rangle = \sum_{n=0}^{\infty} \frac{\beta^n}{\sqrt{n!}}|n\rangle = e^{|\beta|^2/2}|\beta\rangle, \tag{3.14}$$

which have the following nice properties:

$$b||\beta\rangle = \beta||\beta\rangle, \tag{3.15}$$

$$b^\dagger||\beta\rangle = \frac{\partial}{\partial\beta}||\beta\rangle. \tag{3.16}$$

Expressed in terms of this new states, the projectors $\Lambda(\alpha, \beta)$ read:

$$\Lambda(\alpha, \beta) = e^{-\alpha\beta}||\alpha\rangle\langle\beta^*||, \tag{3.17}$$

from which we deduce:

$$b\Lambda(\alpha, \beta) = \alpha\Lambda(\alpha, \beta), \tag{3.18}$$

$$b^\dagger\Lambda(\alpha, \beta) = (\frac{\partial}{\partial\alpha} + \beta)\Lambda(\alpha, \beta), \tag{3.19}$$

$$\Lambda(\alpha, \beta)b^\dagger = \beta\Lambda(\alpha, \beta), \tag{3.20}$$

$$\Lambda(\alpha, \beta)b = (\frac{\partial}{\partial\beta} + \alpha)\Lambda(\alpha, \beta). \tag{3.21}$$

Injecting these last results into Eq.(3.11):

$$b\rho = \int_{\mathcal{C}_\beta}\int_{\mathcal{C}_\alpha} P(\alpha, \beta)\alpha\Lambda(\alpha, \beta)\mathrm{d}\alpha\mathrm{d}\beta, \tag{3.22}$$

$$b^\dagger\rho = \int_{\mathcal{C}_\beta}\int_{\mathcal{C}_\alpha} P(\alpha, \beta)(\frac{\partial}{\partial\alpha} + \beta)\Lambda(\alpha, \beta)\mathrm{d}\alpha\mathrm{d}\beta, \tag{3.23}$$

$$\rho b^\dagger = \int_{\mathcal{C}_\beta}\int_{\mathcal{C}_\alpha} P(\alpha, \beta)\beta\Lambda(\alpha, \beta)\mathrm{d}\alpha\mathrm{d}\beta, \tag{3.24}$$

$$\rho b = \int_{\mathcal{C}_\beta}\int_{\mathcal{C}_\alpha} P(\alpha, \beta)(\frac{\partial}{\partial\beta} + \alpha)\Lambda(\alpha, \beta)\mathrm{d}\alpha\mathrm{d}\beta. \tag{3.25}$$

The differential operators acting on Λ generate operations on $P(\alpha, \beta)$ by integration by part. The integration contours have then to be chosen such that the boundary terms vanish, which

is always possible [93]. Finally we arrive at the following "translation table":

$$b\rho \to \alpha P(\alpha,\beta), \tag{3.26}$$

$$b^\dagger\rho \to (-\frac{\partial}{\partial\alpha}+\beta)P(\alpha,\beta), \tag{3.27}$$

$$\rho b^\dagger \to \beta P(\alpha,\beta), \tag{3.28}$$

$$\rho b \to (-\frac{\partial}{\partial\beta}+\alpha)P(\alpha,\beta). \tag{3.29}$$

From this we see that quadratic terms in the Hamiltonian will generate first order derivatives whereas second order derivatives will arise from quartic terms such as photon-photon interaction. Hence, the master equation takes the form of a Fokker-Planck equation on P:

$$\partial_t P(\boldsymbol{\alpha}) = \left(\frac{\partial}{\partial\alpha_i}A_i(\boldsymbol{\alpha}) + \frac{1}{2}\frac{\partial}{\partial\alpha_i}\frac{\partial}{\partial\alpha_j}D_{ij}(\boldsymbol{\alpha})\right)P(\boldsymbol{\alpha}), \tag{3.30}$$

where we have used the short-hand notation $\boldsymbol{\alpha} = (\alpha_1,\alpha_2) = (\alpha,\beta)$. The general form of this equation remains the same for all P representations, but for a given representation, the diffusion matrix D is not always positive definite.

Before going into the details of the implementation of Eq.(3.30) in the case of the single nonlinear cavity, let us mention, for the sake of generality, two other phase-space functions. One is the Wigner function that we have already encountered in the preceding chapter, the other is the Q-function or Husimi function.

3.1.3 Husimi and Wigner functions

In defining the P-representation, we associated a function of complex variables to the density matrix by imposing the form of the decomposition of ρ, while the expression for P remained implicit in the definition. What then needed to be proved was the existence of such function. It is also possible to proceed in another way, by first, giving an explicit expression for the function and second, verify that all the properties of the operator ρ can be recovered from this function. Both Wigner and Husimi functions are defined this way.

Husimi function

The Husimi or Q-function is defined as follows [94]:

$$Q(\alpha,\alpha^*) = \frac{1}{\pi}\langle\alpha|\rho|\alpha\rangle. \tag{3.31}$$

Since ρ is Hermitian, $Q(\alpha, \alpha^*)$ is positive. Besides, the factor $1/\pi$ ensure that it is normalized to unity: using the resolution of identity for coherent states we find

$$\int Q(\alpha, \alpha^*) \mathrm{d}^2\alpha = 1. \tag{3.32}$$

Therefore this function behaves like a probability distribution. It is well suited for calculation of averages of antinormally ordered operators:

$$\mathrm{Tr}(\rho b^n b^{\dagger m}) = \int \alpha^n \alpha^{*m} Q(\alpha, \alpha^*) \mathrm{d}^2\alpha. \tag{3.33}$$

It is interesting to note that the density matrix in Fock space can be reconstructed from the Q-function, showing that all the properties of the field are contained in this function. The first step in the derivation is to show that the Q-function may be expressed as a power series in α and α^* [88]:

$$Q(\alpha, \alpha^*) = \sum_{n,m} Q_{n,m} \alpha^m \alpha^{*n}, \tag{3.34}$$

with

$$Q_{n,m} = e^{-\alpha\alpha^*} \frac{\langle n|\rho|m\rangle}{\pi\sqrt{n!m!}}. \tag{3.35}$$

Then, the matrix elements of the density operator are given by:

$$\langle n|\rho|m\rangle = \pi\sqrt{n!m!} \sum_r Q_{n-r,m-r}. \tag{3.36}$$

Wigner function

Since we have already encountered the Wigner function in chapter 2 (see the definition in Eq.(2.62)), we will just briefly add that this quasiprobability distribution is useful for computing symmetrically ordered products of creation and annihilation operators:

$$\langle \{b^n b^{\dagger m}\}_{\mathrm{sym.}} \rangle = \int \alpha^n \alpha^{*m} W(\alpha, \alpha^*) \mathrm{d}\alpha. \tag{3.37}$$

We have seen that, in contrast with the Husimi function, the Wigner function may take negative values. A Wigner function with negative value indicates that the state of the electromagnetic field under consideration cannot be understood within a purely classical theory.

3.1.4 Exact solution of the single-cavity problem

The phase-space approach was successfully applied by Drummond and Walls to the problem of a single nonlinear cavity [90]. Using a complex P-representation for the density matrix, they were able to solve the corresponding Fokker-Planck equation and compute exactly all one-time correlation functions in the steady-state. The details of the derivation are presented in Ref.[90], we only give here the final result:

$$\langle (b^\dagger)^j (b)^j \rangle = \left| \frac{2F}{U} \right|^{2j} \times \frac{\Gamma(c)\Gamma(c^*)}{\Gamma(c+j)\Gamma(c^*+j)} \times \frac{\mathcal{F}(j+c, j+c^*, 8|F/U|^2)}{\mathcal{F}(c, c^*, 8|F/U|^2)}, \tag{3.38}$$

with

$$c = 2(-\Delta\omega - i\gamma/2)/U, \tag{3.39}$$

and the hypergeometric function

$$\mathcal{F}(c, d, z) = \sum_n^\infty \frac{\Gamma(c)\Gamma(d)}{\Gamma(c+n)\Gamma(d+n)} \frac{z^n}{n!}, \tag{3.40}$$

where Γ is the gamma special function.

The coefficients of the density matrix can be computed in a similar way:

$$\rho_{p,q} = \frac{1}{\sqrt{p!q!}} \left(\frac{-2F}{U} \right)^p \left(\frac{-2F^*}{U} \right)^q \frac{\Gamma(c)\Gamma(c^*)}{\Gamma(c+p)\Gamma(c^*+q)} \frac{\mathcal{F}(c+p, c^*+q, 4|F/U|^2)}{\mathcal{F}(c, c^*, 8|F/U|^2)}, \tag{3.41}$$

As an illustration of the usefulness of these formulas, let us rederive in a much quicker and more elegant manner the expression of the generalized Fock states found in Eq.(2.59), in the limit $\gamma \ll F \ll \Delta\omega$.

In correspondence of a n-photon resonance, with $n > 1$, the constant c in Eq.(3.39) is given by

$$c = -(n-1)(1 + i\frac{\gamma}{2\Delta\omega}), \tag{3.42}$$

which means that $c \approx -(n-1)$ for $\gamma \ll \Delta\omega$. Since the gamma function has poles at zero and negative integer values, the quantities $\Gamma(c+k), \Gamma(c^*+k)$ are diverging for $0 \leq k < n$, implying that certain coefficients of the hypergeometric series (3.40) will actually diverge in the limit $\gamma \ll F \ll \Delta\omega$.

From the above consideration, the leading contribution in the two hypergeometric functions in Eq.(3.41) are given by

$$\mathcal{F}(c, c^*, 2z) \simeq \frac{\Gamma(c)\Gamma(c^*)}{\Gamma(c+n)\Gamma(c^*+n)} \frac{(2z)^n}{n!}, \tag{3.43}$$

and

$$\mathcal{F}(c+k, c^*+k, z) \simeq \frac{\Gamma(c+k)\Gamma(c^*+k)}{\Gamma(c+n)\Gamma(c^*+n)} \frac{z^{n-k}}{(n-k)!}, \tag{3.44}$$

respectively, where $z = 4F^2/U^2$.

Substituting Eqs.(3.43) and (3.44) into the general expression for the density matrix, Eq.(3.41), we find

$$\rho_{kk} = \frac{1}{2^n k!} \frac{n}{(n-k)!}, \tag{3.45}$$

which corresponds exactly to Eq.(2.59).

It is also easy to see that off-diagonal terms will instead vanish in the same limit $\gamma \ll F \ll \Delta\omega$. Indeed, a similar analysis gives for $q < p$ (the opposite case can be treated in the same way):

$$\rho_{pq} = \frac{1}{\sqrt{p!q!}} \left(\frac{-2F}{U}\right)^{p-q} \frac{1}{2^n} \frac{n!}{(n-q)!(p-q)!}, \tag{3.46}$$

which indeed vanishes for vanishing pump amplitude, $F \to 0$.

The expression for the bosonic coherence is obtained in a similar way. The general formula for $\langle b \rangle$ is:

$$\langle b \rangle = \frac{F}{\Delta\omega + i\gamma/2} \times \frac{\mathcal{F}(1+c, c^*, 8|\frac{F}{U}|^2)}{\mathcal{F}(c, c^*, 8|\frac{F}{U}|^2)}, \tag{3.47}$$

and the leading term in the geometric function appearing in the numerator is:

$$\mathcal{F}(c+1, c^*, 2z) \simeq \frac{\Gamma(c+1)\Gamma(c^*)}{\Gamma(c+1+n)\Gamma(c^*+n)} \frac{(2z)^n}{n!}. \tag{3.48}$$

Using Eq.(3.43), we recover the result of Eq.(2.82):

$$\langle b \rangle = -(n-1)\frac{F}{\Delta\omega}. \tag{3.49}$$

Apart from this new derivation, the exact formulas are of course a powerful tool for computing the mean-field phase diagram of the model in the general case, for arbitrary pumping and dissipation.

3.2 Tunneling-induced bistability

The results for the single cavity can be directly applied to mean-field theory by performing the substitution $F \to F' = F - J\langle b\rangle$ of Eq.(2.80) and solving the self-consistent equation for $\langle b\rangle$ stemming from Eq.(3.47):

$$\langle b\rangle = \frac{(F - J\langle b\rangle)}{\Delta\omega + i\gamma/2} \times \frac{\mathcal{F}(1+c, c^*, 8|\frac{F-J\langle b\rangle}{U}|^2)}{\mathcal{F}(c, c^*, 8|\frac{F-J\langle b\rangle}{U}|^2)}. \tag{3.50}$$

The complete phase diagram can be extracted from Eq.(3.50) by solving the equation numerically. It is most easily done by starting from the exact result at $J = 0$ and increasing the tunneling strength step by step, taking the solution at step n as the initial value (required by the numerical solver), of the step $n + 1$.

One of the key features of the mean-field phase diagram turned out to be "tunneling-induced" bistability. That is, due to the substitution $F \to F - J\langle b\rangle$ performed when considering coupled cavities, the Eq.(3.50) may have multiple solutions, giving rise to several steady-states phases (for the same values of all the parameters). The remainder of this section will be devoted to getting a clearer understanding of this phenomenon. However, before looking at the most general case, it is useful to stay in the limit of weak dissipation while allowing the pump intensity to take arbitrary values. This regime has the virtue of eliminating one variable in an already large enough parameter space. Besides, upon "elimination" of γ, the functions involved in Eq.(3.50) become real (providing the field F is assumed to be real as well). It is therefore possible to visualize the solutions of the self-consistent equation graphically.

3.2.1 Solution for arbitrary pumping and weak dissipation

Interestingly, it turns out that for arbitrary pumping intensity, correlation functions calculated via the exact formula of Eq.(3.38) have a finite limit for $\gamma \to 0$. As in the previous chapter a good starting point is the isolated cavity.

Isolated Cavity

We know from Chap. 2 that in the limit of weak dissipation, if the intensity of the pump is also weak, the effect of multiphotonic resonances plays an important role. In particular, the resonances are visible in the form of peaks in the mean photon density when plotted as

a function of the on-site interaction $U/\Delta\omega$. The left panel of Figure 3.1 shows such plots for different values of $F/\Delta\omega$. We see that for $F/\Delta\omega = 0.2$ and $F/\Delta\omega = 0.4$, the peaks associated with the resonances are clearly visible and are located, as expected, at $U/\Delta\omega = 2/(n-1)$. In accordance with the results of Chap. 2, these peaks in the mean-photon density correspond to dips in the second-order correlation function, as shows in the right panel of Fig.(3.1). Besides, in this regime of parameters the value of $g^{(2)}(0)$ and $\langle b^\dagger b\rangle$ remains quite close to what was found in Eqs.(2.60) and (2.61).

However, as the intensity of the pump is increased further (see the plot corresponding to $F/\Delta\omega = 1.2$ in Fig.(3.1)), the coherent nature of the external field starts to dominate and the resonances, which are a manifestation of field quantization, disappear. Indeed, $g^{(2)}(0)$ goes to 1 with increasing pumping. Note that this result is consistent with the quantum-to-classical crossover that was previously uncovered. We saw that such a crossover takes place in the case of coupled cavities, when the effect of tunneling is equivalent to an increase in the *effective pump*, whereas here it takes place for a single cavity when the *real* pumping intensity is increased.

In Fig.(3.2) is shown the value of $\langle b\rangle$ as a function of $U/\Delta\omega$. Once again the results are in accordance with what was found in Chap. 2. A high density of photons is associated with $\langle b\rangle < 0$.

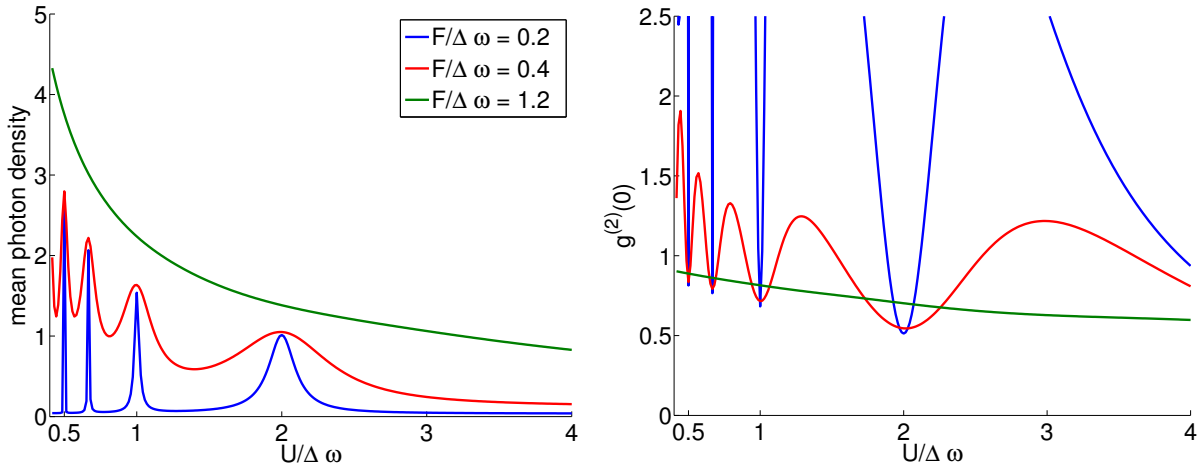

Figure 3.1: Density (left) and second-order correlation function (right) versus on-site interaction $U/\Delta\omega$ of a single cavity. Results are shown for $F/\Delta\omega = 0.2$ (blue), $F/\Delta\omega = 0.4$ (red) and $F/\Delta\omega = 1.2$ (green), with $\gamma \to 0$.

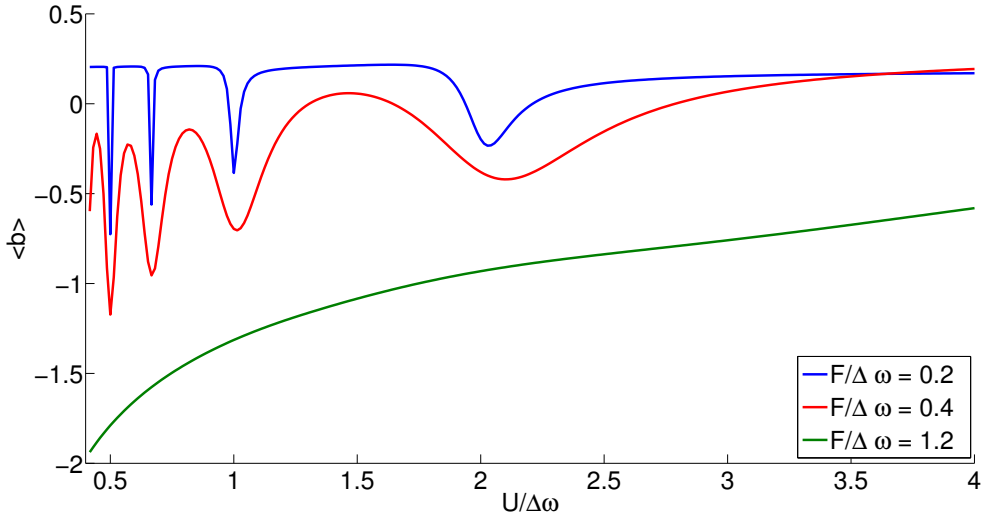

Figure 3.2: Bosonic coherence versus on-site interaction $U/\Delta\omega$ of a single cavity. Same parameters as in Fig.(3.1).

Onset of Bistability

Let us now look at the case of coupled cavities. Since in the regime of weak dissipation the bosonic coherence is real, the self-consistent mean-field equation given by Eq.(3.50) may be solved graphically. The solutions are most easily visualized when the parameter $X = J\langle b\rangle$ is introduced and the equation is written, for each value of U, as $X/J = h_U(F - X)$. In this last expression, we have omitted the parameter $\Delta\omega$ and assumed all other parameters of the Hamiltonian to be expressed in units of $\Delta\omega$.

As with any equation of the type $f(x) = ax$, the value of X that is solution of the mean-field equation is then given by the intersection of the straight line $Y = X/J$ with the curve of $h_U(F - X)$. Note that the latter can be obtained by translating the curve of $h_U(-X)$ to the right. Once the value of X is known, all the properties of the intra-cavity field are determined by the correlation functions of the single cavity, evaluated for the effective pump $F' = F - X$. As in the case of h_U, the plots of correlation functions for $F \neq 0$ can be obtained from the case $F = 0$ trough a translation of the plots to the right. Examples of such functions for $F = 0$ are shown on Fig.(3.3).

Different plots of the function $h_U(-X)$, for various values of U are shown on Fig.(3.4). A clarification is called for, regarding the value for $F = 0$ in these plots. It has been obtained by taking the limit $F \to 0$ while keeping $F/\gamma \gg 1$.

For multiphotonic resonances, the function $g(U, -X)$ has a "Leibniz S" shape. We see that depending on the value of J, there may be up to three solutions to the self-consistent equation. When three solutions $X_1 < X_2 < X_3$ exist, we have $X_1 < 0$, and this solution is the continuous extension of the one existing for $J = 0$. Consequently, the X_1 phase (in the bistable region) has a high-density of photons and $g^{(2)} \leq 1$. We also have $|X_2| \ll |X_1|, |X_3|$. The solution X_2 therefore yields a low-density phase. The solution X_3 gives rise to a steady-state with properties similar to the X_1 phase. We will not say much about this phase here, as stability studies at higher dissipation reveal that this phase is unstable.

Out of the multiphotonic resonances, the shape of the function $h_U(F - X)$ is more complex. It has basically the same properties as the Leibniz S when $X \to \infty$ but the initial slope is negative (as seen in Chapter 2), and the function has one extra local minimum and one extra local maximum (for X positive or negative respectively). In this case, the solution that is a continuous extension of the phase at $J = 0$ is a low-density phase. In contrast with the case of multiphotonic resonances, bistability manifests itself out of the resonances by the appearance of a high-density phase.

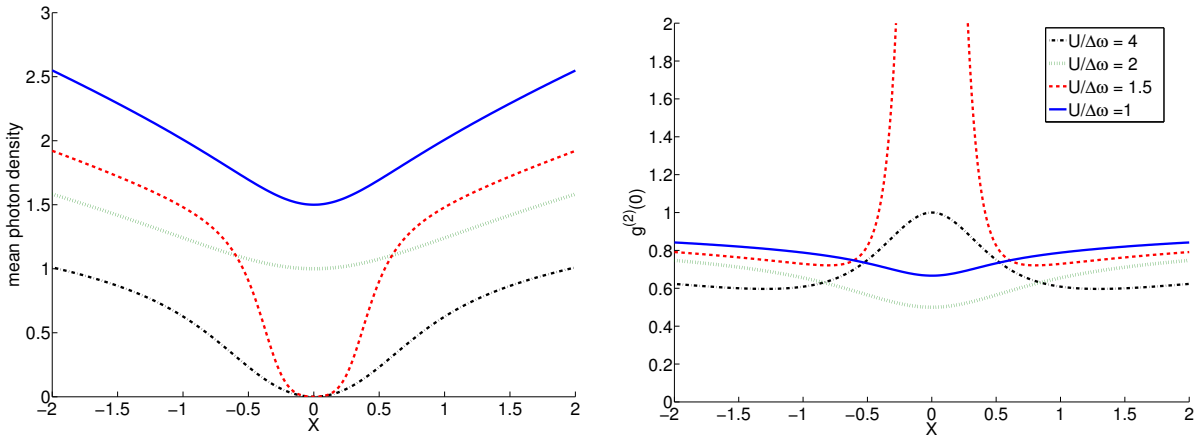

Figure 3.3: Density (left) and second-order correlation function (right) as a function of the parameter $X = J\langle b \rangle$. Results are shown for $U/\Delta\omega = 1$ (solid blue line), $U/\Delta\omega = 1.5$ (red dashed line), $U/\Delta\omega = 2$ (green dotted line) and $U/\Delta\omega = 4$ (black dotted-dashed line), with $\gamma \to 0$.

3.2.2 Bistability diagram in the general case

Let us now examine the bistability diagram in a more general case. In Fig.(3.9) is shown an example for $F/\Delta\omega = 0.4$ and $F/\Delta\omega = 0.2$, with $\Delta\omega > 0$. We have distinguished two regions

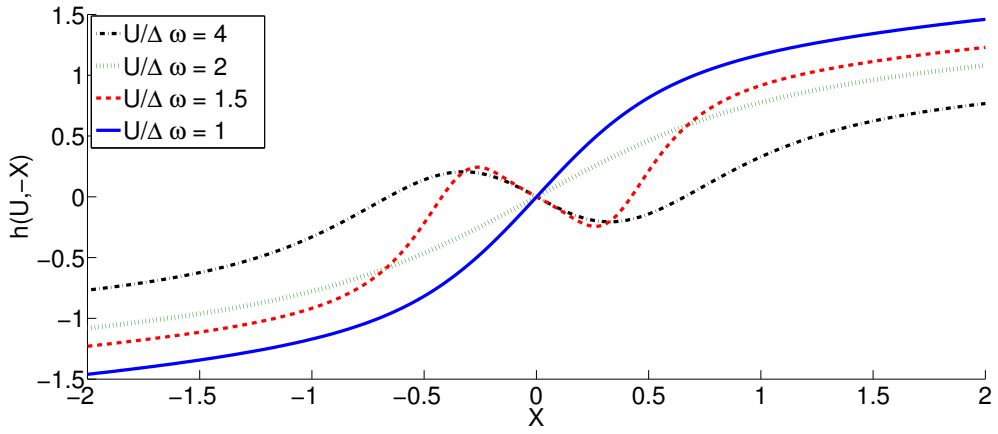

Figure 3.4: Behavior of the function $h_u(-X)$. Same values of U as in Fig.(3.1).

in the diagram: in the area in light blue (labeled "monostable"), there is only one solution to the mean-field self-consistent equation. Multiple solutions of this equation are found in the area in dark blue (labeled "bistable"). As in the previous subsection, the maximum number of solutions is 3. For this set of parameters, we are no longer in the regime of very weak dissipation. We will see however that most of the conclusions drawn in the previous subsection are still qualitatively relevant for the present case.

In particular, the presence of multiphotonic resonances is visible in the form a lobes in the diagram located at $U/\Delta\omega = 2/(n-1)$. In Fig.(3.9), only the lobes $n = 2$, $n = 3$ and $n = 4$ are clearly visible.

Although we will still focus in the following on the case of a blue-detuned external pump, i.e. $\Delta\omega > 0$, we found that the type of bistability discussed here, that is, induced by the coupling between the cavities also appears when the pump frequency is red-detuned with respect to the cavity mode, in contrast with the case of an isolated cavity. An intuitive understanding of this phenomenon will be given later in Sec. 3.2.4, when we compare P-representation calculations with the Gross-Pitaevskii approximation.

To gain further insight on tunneling-induced bistability, let us now look more closely into the properties of the different steady-states phases.

3.2.3 Low Density and High Density Phases

The mean photon density and the value of $g^{(2)}(0)$ are shown in Figs.(3.6) and (3.7) respectively. For each of these figures, two plots are displayed. In each case, the left part of the two

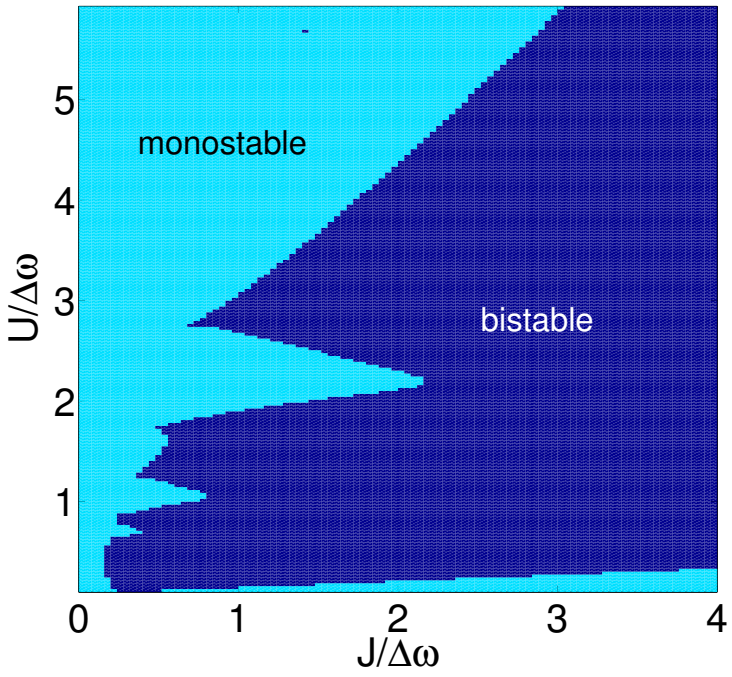

Figure 3.5: Number of mean-field solutions plotted as a function of $J/\Delta\omega$ and $U/\Delta\omega$, for $F/\Delta\omega = 0.4$, $\gamma/\Delta\omega = 0.2$ and $\Delta\omega > 0$. Light blue (labeled "monostable"): only one solution exists. Dark blue (labeled "bistable"): 2 or 3 solutions are found.

plots are the same, as they correspond to the monostable phase. They differ in the bistable region, each one showing a different steady-states phase.

As in the regime of weak pumping, we may identify in the general case a "high-density" phase and a "low-density phase". The low-density phase (see left panels of Figs.(3.6) and (3.7)), is very similar to what was shown to happen for a single cavity outside of multiphotonic resonances. Indeed, the mean photon density is of the order of 10^{-2} and it decreases with increasing J. As for the photon statistics, the emitted light is strongly bunched in the vicinity of the two-photon resonance. Note that the lobes mentioned above corresponding to multiphotonic resonances are clearly visible on the left panel of Fig.(3.6). This shows that at $J = 0$, the system is in the high-density phase in the presence of multiphotonic resonances and in the low-density phase outside of these resonances. When the coupling between the cavity is increased, the two phases start to coexist for a critical value of J.

The high-density phase can also be well understood in the light of what was uncovered in the regime of weak dissipation. First, at small J the states obtained for values of U satisfying the energy matching condition $U/\Delta\omega = 2/(n-1)$ are close to the generalized Fock states

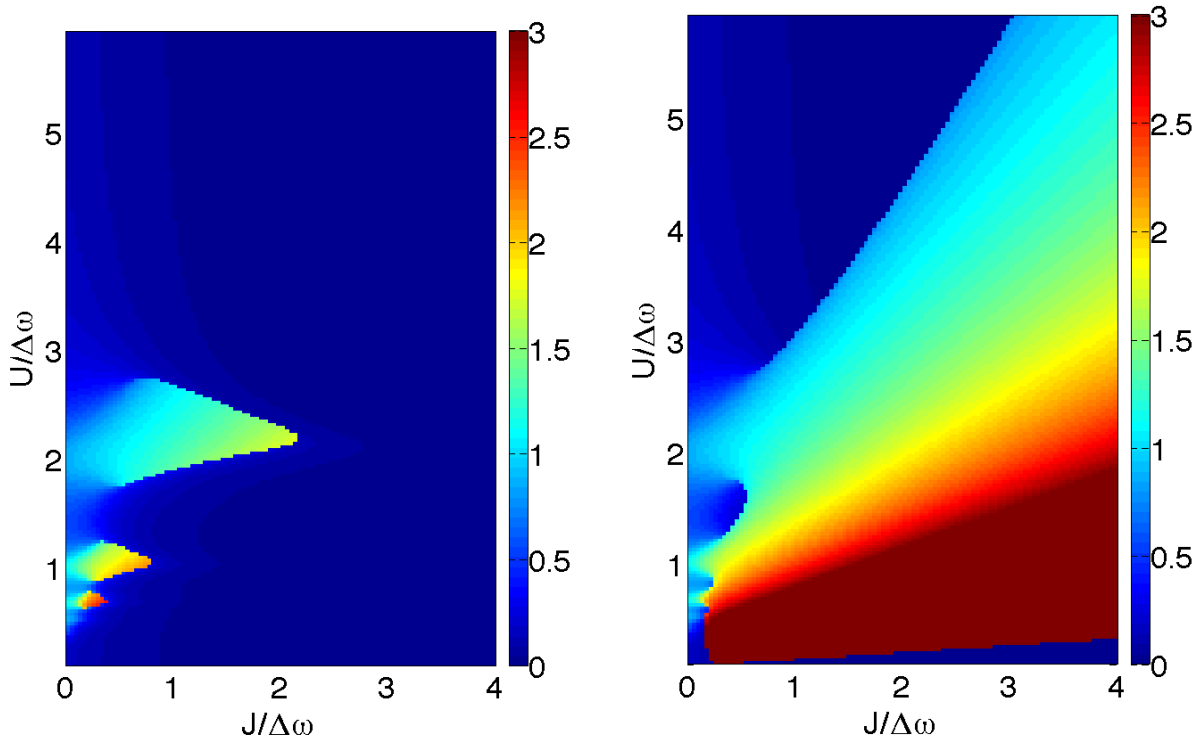

Figure 3.6: Photon occupation number as a function of $J/\Delta\omega$ and $U/\Delta\omega$ for $F/\Delta\omega = 0.4$ and $\gamma/\Delta\omega = 0.2$. Left panel: Mean photon density in the low-density phase. Right panel: the same quantity but for the high-density phase. For sake of clarity, the maximal value of the colorscale in the high-density phase has been set to 3, but the density is higher than 10 at high J and low U. Notice that the monostable region is the same for both panels.

described in the previous chapter. Of course, as the influence of the coherent external field gets stronger, these states are less nonclassical. For example, for the two-photon resonance and for the set of parameters chosen in Figs.(3.6)and (3.7), the minimum value of $g^{(2)}(0)$ is 0.6 instead of 0.5. Once again, the behavior of the mean-photon density with increasing coupling strength is the same as in the regime of weak dissipation, that is the strength of the mean-field effective pump is increased by the coupling. As a result, the mean photon density increases with increasing J. Besides, the light remains antibunched in this phase but tends to be coherent as $J/\Delta\omega \to \infty$.

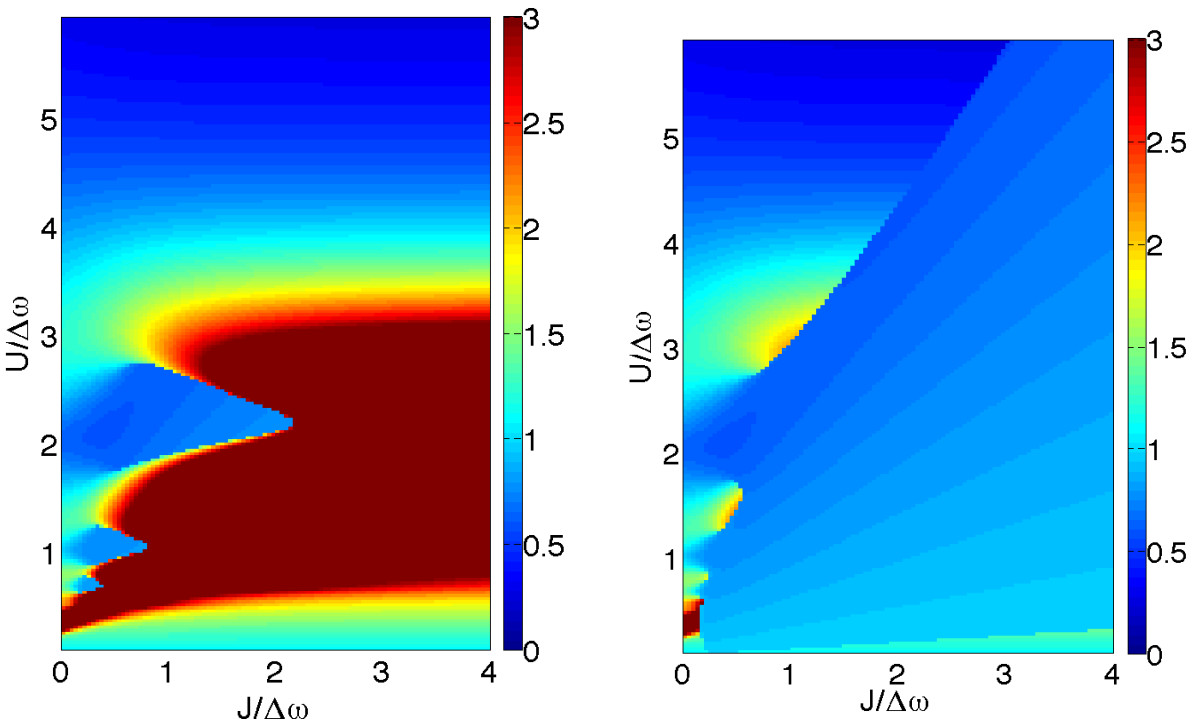

Figure 3.7: Second-order correlation function $g^2(0)$ as a function of $J/\Delta\omega$ and $U/\Delta\omega$. Same parameters as in Fig.(3.6). Left panel: low-density phase. Right panel: high-density phase.

3.2.4 Comparison with Gross-Pitaevskii calculations

The fact that in the high-density phase, the emitted light is almost coherent indicates that the system enters a semi-classical regime. An important feature of this regime is that correlation functions can be approximated by :

$$\langle b^{\dagger n} b^m \rangle \simeq \langle b^\dagger \rangle^n \langle b \rangle^m. \tag{3.51}$$

As a consequence, all these functions are determined by a single complex number, namely the bosonic coherence $\beta = \langle b \rangle$. A general differential equation for correlation functions can be readily obtained from Eq.(1.106). Its most general expression in the context of mean-field theory is the following:

$$\partial_t \langle b^{\dagger n} b^m \rangle = \langle [b^{\dagger n} b^m, H_{mf}] \rangle - \frac{i\gamma}{2}(n+m)\langle b^{\dagger n} b^m \rangle. \tag{3.52}$$

In the particular case of $\beta = \langle b \rangle$ and under the assumption of Eq.(3.51), the previous equation yields:

$$i\partial_t \beta = (-\Delta\omega - J - \frac{i\gamma}{2} + U|\beta|^2)\beta + F. \tag{3.53}$$

This equation is a single-mode version of the Gross-Pitaevskii equation for the lattice system. Note that in this regime, the decoupling of neighboring sites translates into a shift in the cavity frequency, $\Delta\omega \to \Delta\omega + J$. The steady-state value for β is:

$$\beta = \frac{F}{\Delta\omega + J - U|\beta|^2 + \frac{i\gamma}{2}}, \tag{3.54}$$

which gives a third order polynomial equation for the mean photon density $n = |\beta|^2$:

$$n\left[(\Delta\omega + J - nU)^2 + \frac{\gamma^2}{4}\right] = F^2. \tag{3.55}$$

This equation explains the linear asymptotic behavior of n as a function of $J/\Delta\omega$ visible on Fig.(2.4). Indeed, when $F, \gamma, \to 0$ and $J \to \infty$, we find:

$$n \sim \frac{J}{U}, \tag{3.56}$$

which agrees with the results of Fig.(2.4) and Fig.(2.5). Gross-Pitaevskii approximation is also relevant at higher pumping and dissipation, especially when the coupling between sites and the number of photons are very high. As it as been widely use in the theory of Bose-Einstein condensates, whether with cold atoms or polaritons, it is fruitful to compare Gross-Pitaevskii results with P-representation calculations presented above. For example, Fig.(3.8) shows that for large coupling between sites and in the 'high density' phase, Gross-Pitaevskii approximation is sufficient to capture the behavior of the mean photon density as a function of the on-site interaction U.

Gross-Pitaevskii criterium for bistability

Equation (3.55) (with $J = 0$) was introduced in quantum optics as part of a semi-classical theory of optical bistability in a single nonlinear cavity [90]. For some values of the parameters, Eq.(3.55) has three real and positive roots. One of them corresponds to the low-density phase and the two others to high-density phases. Up to this point, the general picture of bistability is not very different to what was shown above for P-representation calculations. Moreover, the fact that within the Gross-Pitaevskii approximation, the coupling between the cavities is equivalent to a shift in the cavity frequency explains why tunneling-induced bistability is not restricted to $\Delta\omega > 0$ but occurs also for $\Delta\omega < 0$.

Let us now compare the two methods on a more quantitative basis. Fig.(3.9) shows the two bistability diagrams obtained respectively from Eq.(3.55) and generalized P-representation.

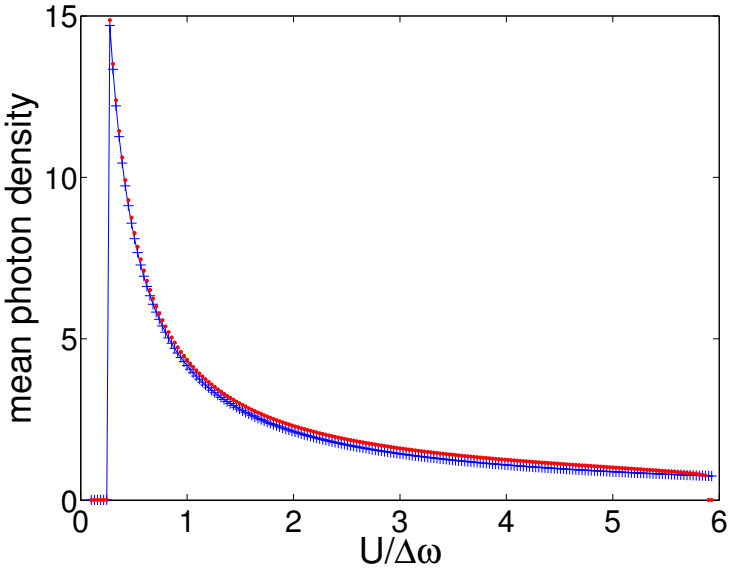

Figure 3.8: Mean photon density versus on-site repulsion U in the high density phase, for $J/\Delta\omega = 3$, $F/\Delta\omega = 0.4$, $\gamma/\Delta\omega = 0.2$. Red dots: P-representation calculations. Blue crosses: Gross-Pitaevskii approximation.

As expected, Gross-Pitaevskii approximation is very good for small values of U, and predicts accurately the appearance of bistability in the lower-right corner of the diagram. It is less accurate when U becomes large and on the whole, bistability is "overestimated" by the Gross-Pitaevskii criterium: monostable regions according to Eq.(3.55) (in orange on Fig.(3.9)), are much smaller that the exact ones (in light blue). In particular it fails completely to predict the lobe structure that is visible on the P-representation diagram. These lobes stem from the n-photon resonances discussed in the previous section. Since a semi-classical approach does not take into account the quantized nature of the field, these resonances are washed out in the Gross-Pitaevskii diagram.

In the framework of Gross-Pitaevskii approximation, the number of solutions is given by the sign of the discriminant of Eq.(3.55). A very good approximation for the critical value of U can be found by noticing that in the high-density phase, the photon density decreases with U. The critical value is then approximately the one for which the density is maximal. This yields:

$$\frac{U_{c1}}{\Delta\omega} = \frac{\gamma^2}{4F^2}(1 + \frac{J}{\Delta\omega}). \tag{3.57}$$

In fact, this approximate expression corresponds to the first term in the expansion in powers

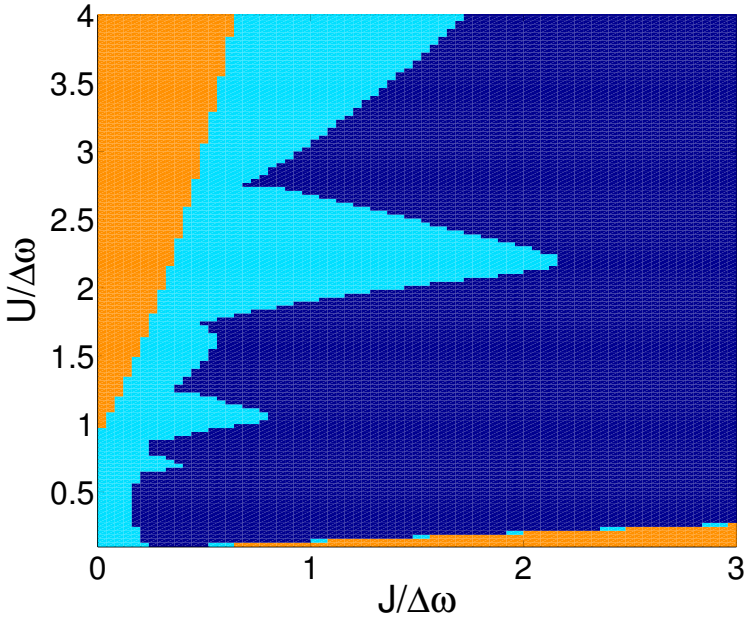

Figure 3.9: Gross-Pitaevskii and P-representation bistability diagrams. Orange: monostable phase according to both approximation schemes. Light blue: bistable according to Eq.(3.55) but monostable according to P-representation calculations. Dark blue: bistable phase according to both approximation schemes.

of $F/\Delta\omega$ of the exact solution. A similar expansion for the other frontier in the diagram gives:

$$\frac{U_{c2}}{\Delta\omega} = \frac{4\Delta\omega^2}{27F^2}(1 + J/\Delta\omega)^3. \tag{3.58}$$

The expansion up to the next term is:

$$\frac{U_{c1}}{\Delta\omega} = \frac{\gamma^2}{4F^2}(1 + \frac{J}{\Delta\omega}) - \frac{\gamma^4}{64\Delta\omega^2F^2(1 + J/\Delta\omega)}, \tag{3.59}$$

$$\frac{U_{c2}}{\Delta\omega} = \frac{4\Delta\omega^2}{27F^2}(1 + J/\Delta\omega)^3 + \frac{\gamma^2}{12F^2}(1 + J/\Delta\omega). \tag{3.60}$$

3.3 Instabilities

Until now, when discussing bistability, we have only considered the number of solutions of Eq.(3.50). In this section, we investigate the stability of these solutions and their corresponding excitation spectrum.

3.3.1 Generalized Bogoliubov theory

In the theory of weakly-interacting Bose-Einstein condensates, the energy spectrum of elementary excitations can be computed by taking into account small fluctuations above the condensate and linearizing the resulting time-dependent equation. This procedure leads to the celebrated Bogoliubov spectrum. The idea behind Bogoliubov theory can be extended to dissipative systems by considering fluctuations of the density matrix around the mean-field solution:

$$\rho = \bigotimes_{i=1}^{N} (\overline{\rho} + \delta\rho_i). \tag{3.61}$$

In Bogoliubov's original work, the key hypothesis was to assume that the operator of the condensate mode can be approximated by a c-number. This corresponds to the Gross-Pitaevskii approximation discussed earlier. Here, we need not assume field operators to be c-numbers, the only approximation is that the density matrix remains factorized.
By injecting Eq.(3.61) into the general master equation and keeping only first order terms in the fluctuations, we find linear differential equations for the coefficients of the matrices $\delta\rho_i$. These equations are coupled in real space but decoupled in reciprocal space, due to translational symmetry. We therefore introduce the Fourier transform of the matrices $\delta\rho_i$:

$$\delta\rho_{\mathbf{k}} = \frac{1}{\sqrt{N}} \sum_{i=1}^{N} e^{-i\mathbf{k}\cdot\mathbf{r}_i} \delta\rho_i. \tag{3.62}$$

For a 2D square lattice, the equations of evolution for $\delta\rho_{\mathbf{k}}$ that stem from linearization around the mean-field solution are:

$$i\partial_t \delta\rho_{\mathbf{k}} = \mathcal{L}_{mf}[\delta\rho_{\mathbf{k}}] + \mathcal{L}_{\mathbf{k}}[\delta\rho_{\mathbf{k}}], \tag{3.63}$$

where

$$\mathcal{L}_{mf}[\delta\rho_{\mathbf{k}}] = [H_{mf}, \delta\rho_{\mathbf{k}}] - \frac{i\gamma}{2}(2b\delta\rho_{\mathbf{k}}b^\dagger - b^\dagger b\delta\rho_{\mathbf{k}} - \delta\rho_{\mathbf{k}}b^\dagger b), \tag{3.64}$$

and

$$\mathcal{L}_{\mathbf{k}}[\delta\rho_{\mathbf{k}}] = -T_{\mathbf{k}} \left(\mathrm{Tr}(b\delta\rho_{\mathbf{k}})[b^\dagger, \rho_{mf}] + \mathrm{Tr}(b^\dagger\delta\rho_{\mathbf{k}})[b, \rho_{mf}] \right), \tag{3.65}$$

with

$$T_{\mathbf{k}} = \frac{2J}{z}(\cos k_x a + \cos k_y a). \tag{3.66}$$

The dispersion relation is obtained by diagonalizing the operator $\mathcal{L}_{mf} + \mathcal{L}_{\mathbf{k}}$ for every $\mathbf{k}$ in the Brillouin zone. Due to dissipation, the energy spectrum is complex and the system is dynamically stable if all eigenvalues have a negative imaginary part.

Note that the operator $\mathcal{L}_{mf}$ is the usual Liouvillian for the effective single cavity problem. This term in Eq.(3.63) is thus independent of $\mathbf{k}$. Propagation effects arise from the other term $\mathcal{L}_{\mathbf{k}}$.

Written in Fock space, Eq.(3.63) reads:

$$\begin{aligned} i\partial_t \delta\rho^{\mathbf{k}}_{n,m} &= [\Delta E_n - \Delta E_m - (m+n)\frac{i\gamma}{2}]\delta\rho^{\mathbf{k}}_{n,m} \\ &+ (F - J\langle b\rangle_{mf})(\sqrt{n}\delta\rho^{\mathbf{k}}_{n-1,m} - \sqrt{m+1}\delta\rho^{\mathbf{k}}_{n,m+1}) \\ &+ (F^* - J\langle b\rangle^*_{mf})(\sqrt{n+1}\delta\rho^{\mathbf{k}}_{n+1,m} - \sqrt{m}\delta\rho^{\mathbf{k}}_{n,m-1}) \\ &- T_{\mathbf{k}}(\sum_q \sqrt{q+1}\delta\rho^{\mathbf{k}}_{q+1,q})(\sqrt{n}\overline{\rho}_{n-1,m} - \sqrt{m+1}\overline{\rho}_{n,m+1}) \\ &- T_{\mathbf{k}}(\sum_q \sqrt{q+1}\delta\rho^{\mathbf{k}}_{q,q+1})(\sqrt{n+1}\overline{\rho}_{n+1,m} - \sqrt{m}\overline{\rho}_{n,m-1}) \\ &+ i\gamma\sqrt{(n+1)(m+1)}\delta\rho^{\mathbf{k}}_{n+1,m+1}, \end{aligned} \tag{3.67}$$

where:

$$\Delta E_n = -n\Delta\omega + \frac{Un(n-1)}{2}. \tag{3.68}$$

To prove that the present formalism is indeed a generalization of Bogoliubov's theory, we first apply it to the equilibrium Bose-Hubbard.

3.3.2 Application to the equilibrium Bose-Hubbard model

As with the equilibrium phase diagram in the previous chapter, we begin by investigating the Mott insulating phase.

Excitations in the Mott phase at equilibrium

We know that at equilibrium (and zero temperature), the mean-field density matrix in the Mott phase is a pure Fock state (the number of particles per site will be denoted by n_0). Therefore, we set:

$$\overline{\rho} = |n_0\rangle\langle n_0|. \tag{3.69}$$

Of course we also have in this case $\gamma = 0$ and $F = 0$. At this point, we need to reintroduce the chemical potential μ in order to recover equilibrium equations. From a purely formal point of view, all that is needed is to replace $\Delta\omega$ with μ in Eq.(3.63). It should be nonetheless

kept in mind that the idea of a "frame rotating at the pump frequency" does not have any physical meaning if $F = 0$.

Since in this configuration, the Hamiltonian is diagonal in the Fock basis, it is natural to use Eq.(3.67) that is written in this basis. Given the expression of the mean-field density matrix, the only non-trivial equations are those where $(n, m) \in \{(n_0, n_0-1), (n_0+1, n_0), (n_0-1, n_0), (n_0, n_0+1)\}$:

$$i\partial_t \delta\rho^{\mathbf{k}}_{n_0,n_0-1} = (E_{n_0} - E_{n_0-1})\delta\rho^{\mathbf{k}}_{n_0,n_0-1} + \sqrt{n_0}T_{\mathbf{k}}(\sqrt{n_0+1}\delta\rho^{\mathbf{k}}_{n_0+1,n_0} + \sqrt{n_0}\delta\rho^{\mathbf{k}}_{n_0,n_0-1}) \quad (3.70)$$

$$i\partial_t \delta\rho^{\mathbf{k}}_{n_0+1,n_0} = (E_{n_0+1} - E_{n_0})\delta\rho^{\mathbf{k}}_{n_0+1,n_0} - \sqrt{n_0+1}T_{\mathbf{k}}(\sqrt{n_0+1}\delta\rho^{\mathbf{k}}_{n_0+1,n_0} + \sqrt{n_0}\delta\rho^{\mathbf{k}}_{n_0,n_0-1}) \quad (3.71)$$

$$i\partial_t \delta\rho^{\mathbf{k}}_{n_0-1,n_0} = (E_{n_0-1} - E_{n_0})\delta\rho^{\mathbf{k}}_{n_0-1,n_0} - \sqrt{n_0}T_{\mathbf{k}}(\sqrt{n_0+1}\delta\rho^{\mathbf{k}}_{n_0,n_0+1} + \sqrt{n_0}\delta\rho^{\mathbf{k}}_{n_0-1,n_0}) \quad (3.72)$$

$$i\partial_t \delta\rho^{\mathbf{k}}_{n_0,n_0+1} = (E_{n_0} - E_{n_0+1})\delta\rho^{\mathbf{k}}_{n_0,n_0+1} + \sqrt{n_0+1}T_{\mathbf{k}}(\sqrt{n_0+1}\delta\rho^{\mathbf{k}}_{n_0,n_0+1} + \sqrt{n_0}\delta\rho^{\mathbf{k}}_{n_0-1,n_0}) \quad (3.73)$$

The density matrix is Hermitian, and since all the parameters are real, it is also real. In consequence, the last two equations do not provide any additional information and it is sufficient to consider the first two. The operator $\mathcal{L}_{mf} + \mathcal{L}_{\mathbf{k}}$ that needs to be diagonalized thus simply reduces to a 2×2 matrix, namely:

$$\mathcal{M}_{\mathbf{k}} = \begin{pmatrix} E_{n_0} - E_{n_0-1} + nT_{\mathbf{k}} & \sqrt{n(n+1)}T_{\mathbf{k}} \\ -\sqrt{n(n+1)})T_{\mathbf{k}} & E_{n_0+1} - E_{n_0} - (n+1)T_{\mathbf{k}} \end{pmatrix} \quad (3.74)$$

Let us recall that:

$$E_{n_0} - E_{n_0-1} = -\mu + (n_0 - 1)U, \quad (3.75)$$

$$E_{n_0+1} - E_{n_0} = -\mu + n_0 U. \quad (3.76)$$

Thus, the characteristic polynomial of $\mathcal{M}_{\mathbf{k}}$ is given by:

$$\chi(\Omega) = \Omega^2 - \Omega\left((2n_0 - 1)U - 2\mu - T_{\mathbf{k}}\right) + (n_0 U - \mu)((n_0 - 1)U) - \mu + T_{\mathbf{k}}(U + \mu). \quad (3.77)$$

Let us set:

$$\delta\mu = \mu - (n_0 - \frac{1}{2})U \quad \text{and} \quad x = n_0 + \frac{1}{2}. \quad (3.78)$$

With these notations, χ reads:

$$\chi(\Omega) = \Omega^2 + (2\delta\mu + T_{\mathbf{k}})\Omega + \delta\mu^2 - \frac{U^2}{4} + T_{\mathbf{k}}(U + \mu). \quad (3.79)$$

Finally, the dispersion relation for the elementary excitations is given by:

$$\omega_{\pm}(\mathbf{k}) = -\delta\mu - \frac{T_{\mathbf{k}}}{2} \pm \sqrt{T_{\mathbf{k}}^2 + U^2 - 4T_{\mathbf{k}}x}, \tag{3.80}$$

which is exactly the expression that is obtained using the usual methods of quantum field theory, for example in their path-integral formulation [95]. Starting from Eq.(3.67) it is also possible to calculate numerically the eigenvalues of the general 9×9 Bogoliubov matrix. Results for a point inside the first lobe and at the tip of the first lobe are shown in Fig.(3.10)

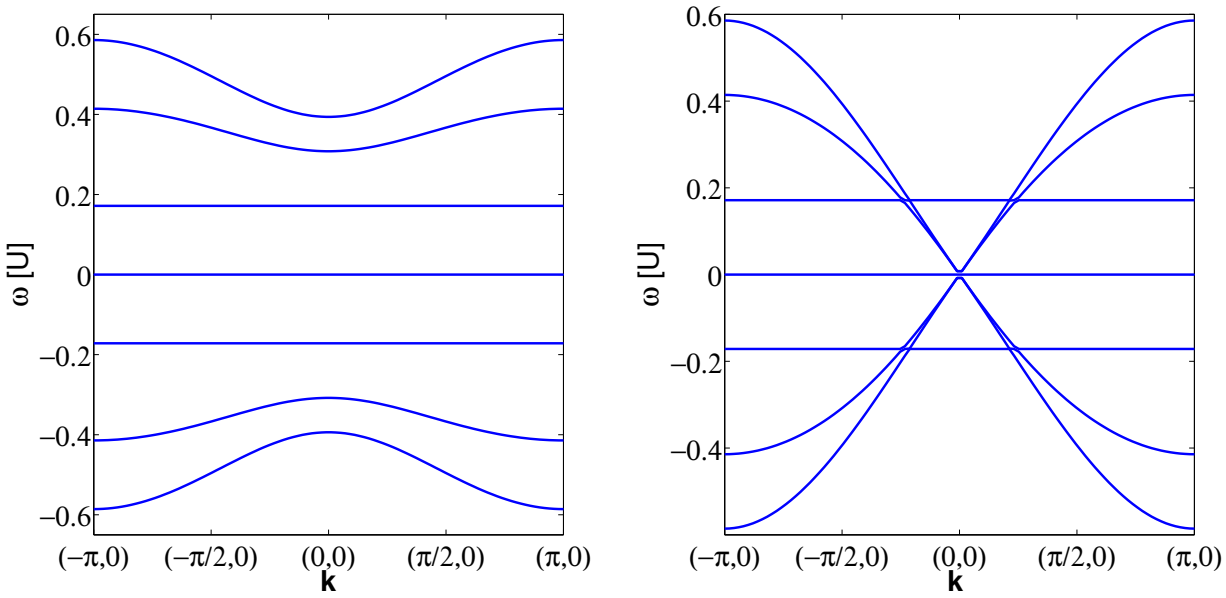

Figure 3.10: Left: bosons dispersion relation inside the first lobe. $J/U = J_c/2U$ and $\mu/U = \mu_c/U$, where J_c and μ_c correspond to the tip of the lobe. Right: Bosons dispersion at the tip of the first lobe. $J/U = 3 - 2\sqrt{2}$ and $\mu/U = \sqrt{2} - 1$.

The constant eigenvalues correspond to trivial equations in Eq. 3.63, and are not physically relevant. We also see here the $\pm\Omega$ symmetry that was underlined above. Looking at the positive eigenvalues, we recognize the "hole" and "particle" excitations. The presence of a gap in the spectrum is characteristic of the Mott insulating phase.

If the same dispersion relation is plotted at the tip of the lobe, a gapless phonon mode appears, indicating a transition to the superfluid phase (see right panel on Fig.(3.10)). Moreover, we recover the well-known Lorentz invariance at this particular point of the phase diagram [96].

The Superfluid Side of the Transition

Since the Gutzwiller ansatz is exact in the Mott phase, it is also expected to give satisfactory results in the superfluid phase, close to the transition.

We can therefore calculate numerically the mean-field solution and the excitation spectrum in the superfluid phase using the same method, as long as we stay close to the transition. A example of such a spectrum is on Fig.(3.11).

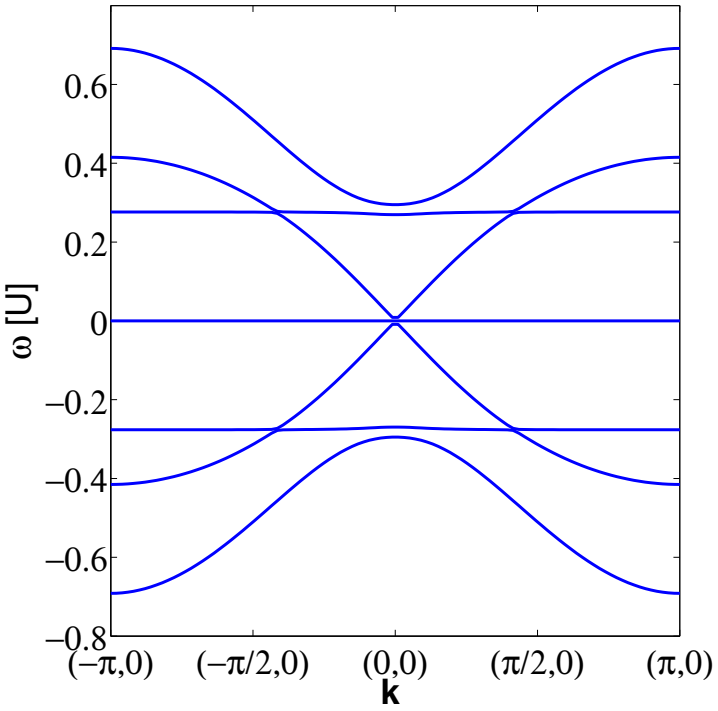

Figure 3.11: Bosons dispersion relation in the SF phase. $J/U = J_c/U + 0.06$ and $\mu/U = \mu_c/U - 0.12$.

Two modes can be identified in this spectrum: a gapless phonon mode, which corresponds to phase fluctuations of the order parameter, and a gapped mode, relative to amplitude fluctuations. Once again, these results are consistent with the ones obtained using other approaches [97].

3.3.3 Excitation spectrum for the driven-dissipative model

Emergence of inhomogeneous phases

Equipped with the generalized Bogoliubov theory, we can now compute the excitation spectrum of the driven-dissipative model and determine the stability of the different steady-states phases. The study was carried out for the same parameters as in Fig.(3.9). The number of stable solutions is shown on Fig.(3.12). As mentioned previously, in most of the bistable region, 2 out of the 3 potentially existing solutions are stable. There are however areas were the low-density phase becomes unstable (marked in red and yellow on Fig.(3.12)). In particular, in the region marked in red in Fig.(3.12), there is only one solution and it is unstable.

At this point, it is important to recall that within our mean-field approximation, all the sites are equivalent. Hence, we only have access to spatially homogeneous solutions. The fact that there is no homogeneous mean-field solution for some values of the parameters, may therefore indicate a breaking of translational symmetry and the emergence of inhomogeneous phases. Note that this kind of modulational instabilities do occur in other nonlinear optical systems like parametric oscillators [98].

In order to understand better this phenomenon, let us take a look at the excitation spectrum. Dispersion relations at the edge of the unstable region (points A, A', B and B' on Fig. 3.9), are plotted on Fig. 3.13 and 3.14. We see on Fig. 3.13 and Fig. 3.14 that on the left side of the unstable region, instabilities arise at $\mathbf{k} = (\pi/a, \pi/a)$. This indicates that as we cross the unstable region from the left by increasing the coupling between cavities, an inhomogeneous density-wave steady-state occurs. Note that the other edge, the unstable $\mathbf{k}$-vectors are smaller and located well inside the Brillouin zone. Another remarkable point is that the real part of the unstable branch is zero for every $\mathbf{k}$ inside the Brillouin zone while the imaginary part is strongly dispersive. Since in the case of thermal equilibrium the excitation spectrum is real, the existence of a purely imaginary branch is obviously related to dissipation. But it is interesting to note that the dispersive nature of purely imaginary branches is a consequence of interactions. Indeed, in the low-density phase, when $J \gg U$, all eigenvalues have completely flat imaginary parts. In this regime there are two (anti-conjugate) dispersive branches whose real parts originate from the bare boson dispersion on a square lattice.

The existence of this purely imaginary branch can be seen analytically in a very low density regime, assuming that there is at most one photon per site. We can then approximate

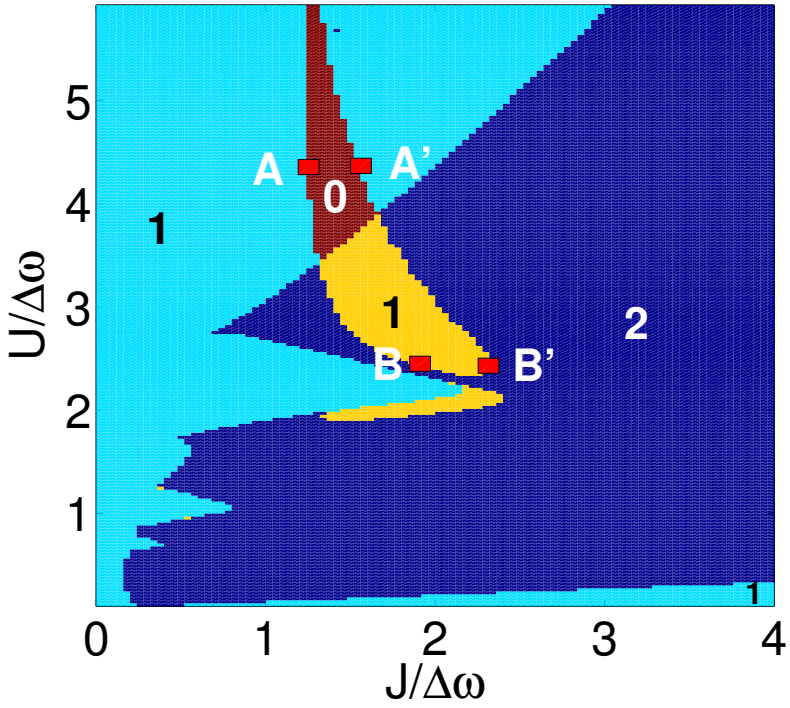

Figure 3.12: Number of stable mean-field solutions plotted as a function of $J/\Delta\omega$ and $U/\Delta\omega$. Same parameters as in Fig.(3.9). Yellow part (central region labeled with '1'): only one stable phase out of 3 existing solutions. Red part (label '0'): only one solution, which is unstable. A, A',B and B' are points on the edge of the unstable zone whose excitation spectrum is presented in Figs.(3.13) and (3.14).

our description by working in a truncated Hilbert space with at most one photon per site. The vector $\delta\rho^{\mathbf{k}}$ has then only four coefficients, $(\delta\rho^{\mathbf{k}}_{00}, \delta\rho^{\mathbf{k}}_{01}, \delta\rho^{\mathbf{k}}_{11}, \delta\rho^{\mathbf{k}}_{10})^T$ and $\mathcal{L}_{\mathbf{k}}$ is given by:

$$\mathcal{L} = \begin{pmatrix} 0 & (A^*+F^*)+T_{\mathbf{k}}\overline{\rho}^*_{10} & i\gamma & -(A+F)-T_{\mathbf{k}}\overline{\rho}_{10} \\ A+F & -\Delta\omega - T_{\mathbf{k}}(\overline{\rho}_{00}-\overline{\rho}_{11}) - i\frac{\gamma}{2} & -(A+F) & 0 \\ 0 & -(A^*+F^*)-T_{\mathbf{k}}\overline{\rho}^*_{10} & -i\gamma & (A+F)+T_{\mathbf{k}}\overline{\rho}_{10} \\ -(A^*+F^*) & 0 & A^*+F^* & \Delta\omega + T_{\mathbf{k}}(\overline{\rho}_{00}-\overline{\rho}_{11}) - i\frac{\gamma}{2} \end{pmatrix} \tag{3.81}$$

where $A = -J\langle b\rangle$ is the mean-field parameter, $(\overline{\rho}_{00}, \overline{\rho}_{10}, \overline{\rho}_{11})$ the coefficients of the steady-state density matrix and $T_{\mathbf{k}} = -2J/z(\cos(k_x a) + \cos(k_y a))$ as in Eq.(3.66).

Let us show that such 4×4-matrix has always a purely imaginary eigenvalue. First we see that the first and the third row of this matrix are not linearly independent. This is simply a consequence of the constraint $\mathrm{Tr}[\rho] = 1$, which in turn implies $\delta\rho^{\mathbf{k}}_{00} + \delta\rho^{\mathbf{k}}_{11} = 0$ at all times.

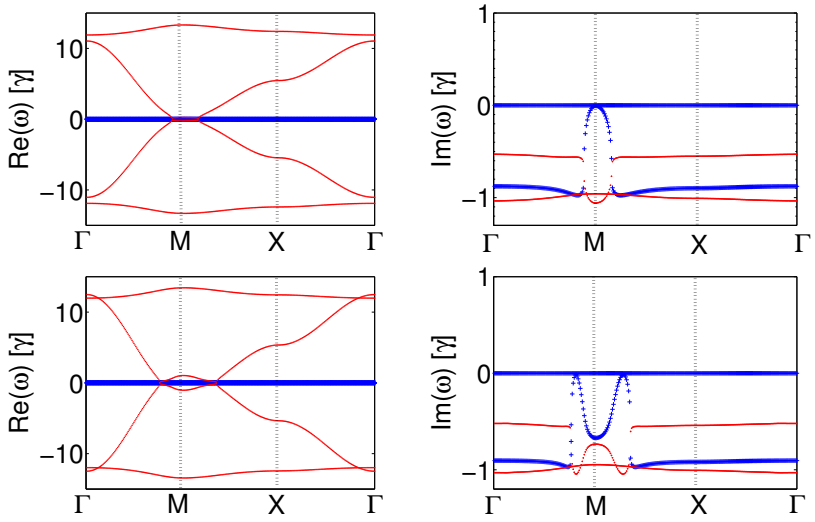

Figure 3.13: Energy-momentum dispersion of elementary excitations for points A (upper panel) and A' (lower panel), indicated in Fig.(3.12). Real and imaginary part of the low-energy branches (in units of γ) are plotted vs $\mathbf{k}$. $\Gamma = (0,0)$, $M = (\pi/a, \pi/a)$, $X = (\pi/a, 0)$ are special points in the Brillouin zone of the squared photonic lattice. Thick blue lines depict branches with a flat real part over the entire Brillouin zone, while the imaginary part is strongly dispersive with a resonance around specific wavevectors.

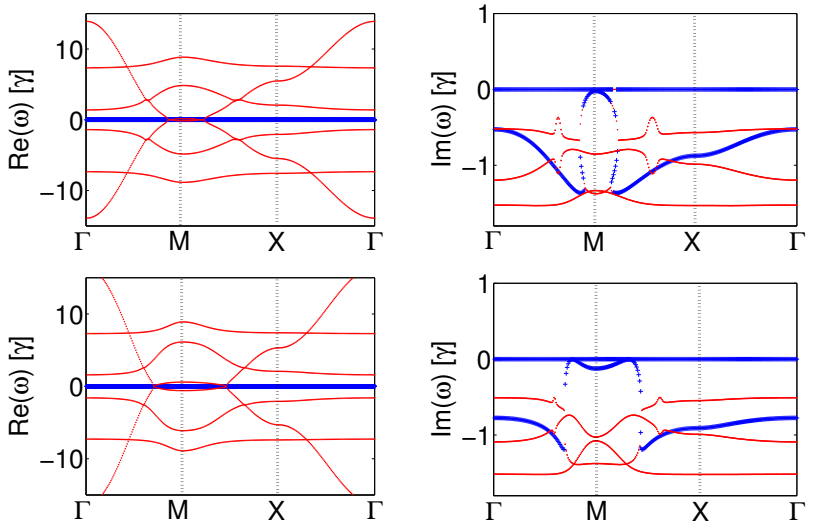

Figure 3.14: Excitation dispersions for points B (upper panel) and B' (lower panel). Same conditions as in Fig.(3.13).

It is therefore more convenient to work with the variables $\{\delta\rho_{00}^{\mathbf{k}} - \delta\rho_{11}^{\mathbf{k}}, \delta\rho_{00}^{\mathbf{k}} + \delta\rho_{11}^{\mathbf{k}}\}$ instead of $\{\delta\rho_{00}^{\mathbf{k}}, \delta\rho_{11}^{\mathbf{k}}\}$. In this new basis, upon elimination of the superfluous row and column, we obtain a 3×3 matrix, $i\mathcal{M}$ whose general structure is

$$\mathcal{M} = \begin{pmatrix} G & B & B^* \\ C & D & 0 \\ C^* & 0 & D^* \end{pmatrix}, \tag{3.82}$$

with $G = -\gamma \in \mathbb{R}$, $B = -2i(A^* + F^*) - 2it_{\mathbf{k}}\overline{\rho}_{10}^*$, $C = -i(A + F)$ and $D = i(\Delta\omega + t_{\mathbf{k}}(\overline{\rho}_{00} - \overline{\rho}_{11})) - \frac{\gamma}{2}$.

The factor i has been added for convenience, as it is more natural to work with real rather than purely imaginary quantities. Indeed, given the particular structure of $\mathcal{M}$, its characteristic polynomial χ has real coefficients. This polynomial reads:

$$\begin{aligned} \chi = &- X^3 + (2\mathrm{Re}(D) + G)X^2 \\ &+ (2\mathrm{Re}(\mathrm{BC}) - |D|^2 - 2\mathrm{Re}(D))X \\ &- 2\mathrm{Re}(B^*C^*D) + G|D|^2. \end{aligned} \tag{3.83}$$

Since $\chi \in \mathbb{R}[X]$, it has at least one real root and if the other two are not real, they are complex conjugate. In other words, $\mathcal{L}$, which has, up to a factor i, the same eigenvalues as $i\mathcal{M}$ has at least one imaginary branch.

We have checked numerically that in the low density regime such truncated matrix agrees with the results obtained by including the full linearization matrix.

Comparison with the Gross-Pitaevskii approximation

We have seen that Gross-Pitaevskii approximation gives satisfactory results in the weakly interacting sector of the phase diagram. Let us see what happen with the energy spectrum.

Computation of the dispersion relation is greatly simplified in this regime where the system is described by classical complex field. Fluctuations around the mean-field value β obey the following equation:

$$i\partial_t \begin{pmatrix} \delta\beta_{\mathbf{k}} \\ \delta\beta_{-k}^* \end{pmatrix} = \begin{pmatrix} -\Delta\omega - T_{\mathbf{k}} + 2U|\beta|^2 - i\gamma/2 & U\beta^2 \\ U\beta^{*2} & \Delta\omega + T_{\mathbf{k}} - 2U|\beta|^2 - i\gamma/2 \end{pmatrix} \begin{pmatrix} \delta\beta_{\mathbf{k}} \\ \delta\beta_{-k}^* \end{pmatrix}. \tag{3.84}$$

This leads to a complex Bogoliubov spectrum:

$$\omega_{\pm}(\mathbf{k}) = \pm\sqrt{(-\Delta\omega - T_k + 2U|\beta|^2)^2 - U^2|\beta|^4} - \frac{i\gamma}{2}. \tag{3.85}$$

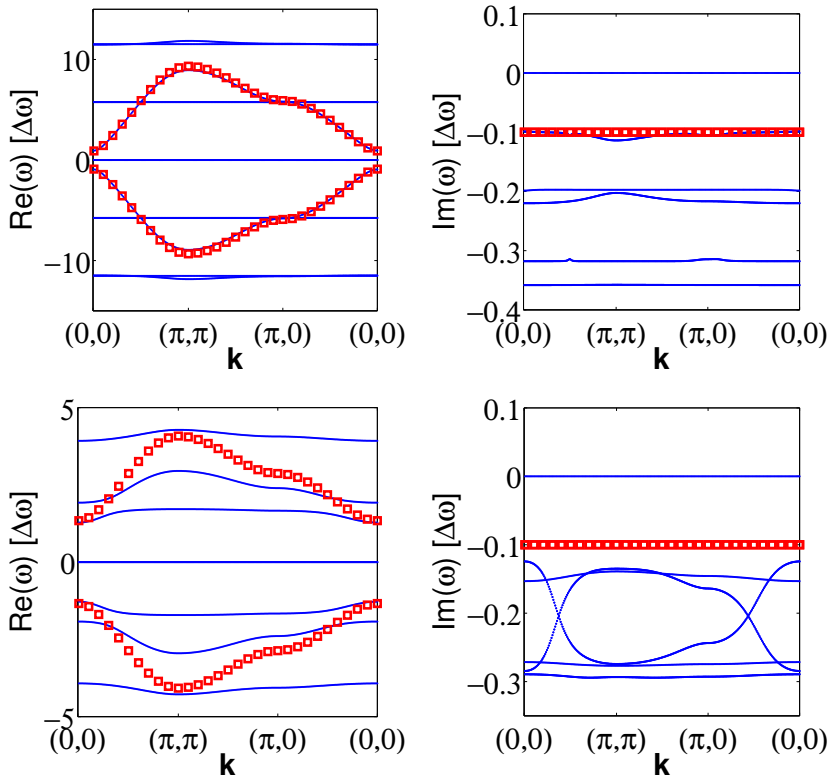

Figure 3.15: Energy-momentum dispersion of elementary excitations. Upper panels: $\gamma/\Delta\omega = 0.2$, $F/\Delta\omega = 0.4$, $U/\Delta\omega = 0.5$ and $J/\Delta\omega = 3$ (high-density phase). Real and imaginary part of the low-energy branches (in units of γ) are plotted vs $\mathbf{k}$. Blue and black lines depict branches obtained with Eq.(3.63), the two red lines are the branches derived from Gross-Pitaevskii equations. For these parameters, Gross-Pitaevskii approximation is accurate. Lower panels: $\gamma/\Delta\omega = 0.2$, $F/\Delta\omega = 0.4$, $U/\Delta\omega = 2$ and $J/\Delta\omega = 1$ (monostable phase). Gross-Pitaevskii approximation fails in the regime of strong correlations.

Dispersion relations extracted from Eq.(3.63) and Eq.(3.85) are shown on Fig.(3.15). For small on-site repulsion and large tunneling amplitude ($U/\Delta\omega = 0.5$ and $J/\Delta\omega = 3$, upper panels), the Gross-Pitaevskii approximation give good quantitative results and the corresponding spectrum is included in the more general approached outlined in Eq.(3.63). As expected, it fails in the regime of strong correlations. Lower panels of Fig.(3.15) show the dispersion relations for $U/\Delta\omega = 2$ and $J/\Delta\omega = 1$. In this regime, $g^{(2)}(0) = 0.69$, proving that the hypothesis of a quasi coherent state underlying the Gross-Pitaevskii approximation scheme is not justified.

3.4 Conclusion

In this chapter we presented an efficient method for computing the mean-field phase diagram of the driven-dissipative Bose-Hubbard model in the most general case. This method is based on an analytical solution for the single-site problem, relying on the use of the complex P-representation.

An important feature of the mean-field phase diagram is tunneling-induced bistability. In a wide region of the diagram, the theory predicts the existence of two stable steady-states (for the same value of all the parameters). Interestingly, these two stable phases share great similarities with the two types of steady-states found in Chap.2 at weak pumping and weak dissipation. Indeed, one of the phases has a high-density of photon and $g^{(2)}(0) \leq 1$. Besides, for values of $U/\Delta\omega$ corresponding to multiphotonic resonances and for weak tunneling rates, the light is strongly antibunched. The other phase is a low-density phase that exhibits superbunching near the two-photon resonance.

Remarkably, the study of stability revealed that for certain values of the parameters, collective excitations with a purely imaginary energy-momentum dispersion trigger modulational instabilities at specific wavevectors. This type of instabilities indicates the emergence of inhomogeneous phases in the system.

It is noteworthy that the prediction of tunneling-induced bistability is not specific to the P-representation mean-field theory. Indeed, such phenomenon also arises within the simpler framework of the Gross-Pitaevskii equation. We have shown however that in the strongly correlated regime, the Gross-Pitaevskii approximation fails to give correct results.

Although it is more accurate than the Gross-Pitaevskii approach, P-representation mean-field theory is still not a fully controlled approximation. Only further studies going beyond mean-field will eventually determine its range of validity. The next chapter is a first step in this direction.

Chapter 4

Exact numerical simulations on finite-size systems

Although the mean-field approximation that we have used extensively so far is exact in the limit $J = 0$ or $U = 0$, it is not a controlled approximation. It is indeed very difficult to evaluate the error on the density matrix or the observables, with respect to the exact solution. The only way to validate or invalidate the predictions of mean-field theory is therefore to compare it with the results of other more accurate methods. To go forward in this direction we have chosen to perform exact numerical simulations on finite-size arrays of cavities.

Simulating exactly quantum many-body systems is however a tremendous task: the dimension of the Hilbert space for a multipartite system consisting of m subsystems, each of them described by a space of dimension N, is N^m. Furthermore, in nonequilibrium conditions, the system can no longer be described in terms of pure states, but the full density matrix must be considered. In this case, the number of variables to be determined scales as N^{2m}, namely the square of the size of the Hilbert space. In the case of cavity arrays where we may have to consider 3 or 4 photons per site, the problem becomes quickly intractable with brute-force methods, even for relatively small lattices: the dimension of the Hilbert space for a 3×3 square lattice with up to 4 photons per cavity is already $5^9 \simeq 2 \times 10^6$.

In this context, the need for a new and efficient method for simulating two-dimensional driven-dissipative systems gave rise to an ambitious project that was started with Alexandre Baksic and Stefano Finazzi, under the supervision of Cristiano Ciuti. We were later joined by Florent Storme and are still actively working on the subject. As a result, rather than presenting a systematic study of the validity of the mean-field approximation, this chapter will focus on the main ideas and the first results of this new numerical method.

The main purpose of the method is to simplify the initial problem by restricting the time

evolution of the system to a small "corner" of the Hilbert space that would contain all the relevant many-body states. The accuracy of the results can then be improved by increasing the size of the corner until convergence (in the value of the observables) is reached.

We have developed two types of "corner method". In the first approach, we select the most probable states at the single-site level by diagonalizing the mean-field density matrix. The corner basis is then formed by taking the most probable products of single-site states. We will see that this approach has better performance than a direct simulation in Fock state but still has limitations in lattice size. The second, more sophisticated approach is based on a real-space renormalization procedure. The corner basis is constructed by merging smaller lattices and selecting the most probable product states. An article presenting the results of this second approach is currently under review [24].

4.1 A first approach: Selecting a corner space from the mean-field density matrix

The very general idea of selecting a small portion of a gigantic Hilbert space has been at the heart of several approximation schemes developed in the last decades. Most of these works were devoted to equilibrium systems for which the fundamental task is to find the many-body ground state. The first attempt in this direction was the renormalization group technique, proposed by Wilson and successfully applied to the Kondo problem [99]. Numerical implementations of this approach are based on the solution of a system with a smaller Hilbert space, where only the relevant physical states with the lower energy are retained. Ideally this procedure can be iterated by arbitrarily growing the size of the system step by step, by doubling it, for instance, at each iteration. Unfortunately, such a naive numerical implementation of the real-space renormalization group often yields poor results for nondissipative quantum lattice systems, because the boundary conditions imposed while solving the smaller system are generally not appropriate to describe the doubled one [100].

In the case of one-dimensional systems, a solution to this impasse is represented by the density matrix renormalization group (DMRG) [101], a more sophisticated technique which provides extremely precise results, often up to numerical precision, and which is based on the selection of most probable states of a properly constructed reduced density matrix. Behind the success of this method lies the fact that it operates on a very specific class of quantum states called matrix-product states (MPS) [102]. Generalization of this technique for spatial dimension larger than one have been introduced, based on an artificial description in terms of one-dimensional systems with long-range interactions [103] or through the generalization of matrix product states to projected entangled-pair states (PEPS) [104]. However, going from one to two spatial dimension makes all the calculations much more difficult. Hence, improving the efficiency of these algorithms is still a subject of intense research.

These approaches, and in particular the DMRG procedure for 1D-systems, can be generalized to open systems by working in the super-Hilbert space of density matrices [105, 106, 107, 108]. The price to pay is to add another level of complexity, which is still manageable for 1D systems but makes 2D problems even more difficult to tackle.

We have explored an alternative route and developed a new method that is well suited for dealing with two-dimensional systems such as arrays of nonlinear cavities. As already mentioned, the objective is to find a way to classify the states and select the most relevant

ones. One way of doing so is to find an approximate density matrix in the total Hilbert space, which can be readily diagonalized. In the basis in which this density matrix in diagonal, a certain probability is associated to each of the state-vectors. The subspace generated by the most probable states is then a good candidate for the "corner space". In this section, we describe a first implementation of this idea, taking the mean-field density matrix as an approximate solution. The different steps of the procedure, presented in details below, are the following:

1. Diagonalize the single-site mean-field density matrix.

2. Select the M most probable product states as a basis for the corner space.

3. Determine the steady-state solution of the density matrix in the corner space.

4. Increase M until convergence is reached for all the observables.

4.1.1 Main steps of the algorithm

Step 1: Diagonalization of the mean-field density matrix

The first step for the selection of the most probable states is to diagonalize the single-site mean-field density matrix:

$$\rho^{(MF)} = \sum_j p_j^{(MF)} |\psi_j^{(MF)}\rangle\langle\psi_j^{(MF)}|, \tag{4.1}$$

where the states are ordered in such a way that:

$$p_j^{(MF)} \geq p_{j+1}^{(MF)}. \tag{4.2}$$

Note that before diagonalization, the density matrix is typically represented in the Fock basis. For all practical purposes, one always has to set a maximum number of photons per site N_{max}, which will in turn determine the maximum number of eigenstates $|\psi_0^{(MF)}\rangle, |\psi_1^{(MF)}\rangle \ldots |\psi_{N_{max}}^{(MF)}\rangle$, of the mean-field density matrix that will be taken into account. This cutoff N_{max} has to be large enough to ensure convergence of the mean-field solution. If however the probability distribution of the eigenstates is concentrated on a few states, the number of states per site that will eventually contribute to the steady-state may be much smaller than N_{max}.

Step 2: Selection of the most probable product states as a basis for the corner space

Once the diagonal form of the mean-field density matrix in known, the states spanning the corner space are chosen in the following way: to select a corner space of size M, we keep the M most probable product states of the form

$$|\psi^{(MF)}_{r_j(1)}\rangle|\psi^{(MF)}_{r_j(2)}\rangle \dots |\psi^{(MF)}_{r_j(N_{site})}\rangle, \tag{4.3}$$

ranked according to the joint probability $p^{(MF)}_{r_j(1)}p^{(MF)}_{r_j(2)} \dots p^{(MF)}_{r_j(N_{site})}$, where the indices indicating the rank are such that:

$$p^{(MF)}_{r_j(1)}p^{(MF)}_{r_j(2)} \dots p^{(MF)}_{r_j(N_{site})} \geq p^{(MF)}_{r_{j+1}(1)}p^{(MF)}_{r_{j+1}(2)} \dots p^{(MF)}_{r_{j+1}(N_{site})}. \tag{4.4}$$

These states form an orthonormal basis of the corner space.

Note that in the expression above, one can have $p^{(MF)}_{r_j(k)} < p^{(MF)}_{r_{j+1}(k)}$ for some site indices even though the product of the probabilities is such that Eq.(4.4) is satisfied. It occurs, for example, if the probability distribution in Eq.(4.1) is such that

$$p^{(MF)}_1 p^{(MF)}_1 > p^{(MF)}_0 p^{(MF)}_2. \tag{4.5}$$

It is then more probable to have two sites in $|\psi^{(MF)}_1\rangle$ than one site in $|\psi^{(MF)}_2\rangle$ and one in $|\psi^{(MF)}_0\rangle$.

The Hilbert space generated by the product states of Eq.(4.3) can be viewed as composed of several "shells" containing states with the same probability. Indeed, the probability of a state is entirely determined by a vector $(n_0, n_1, \dots, n_{N_{max}})$, with

$$\sum_{j=0}^{N_{max}} n_j = N_{site}, \tag{4.6}$$

denoting the number of sites in states $|\psi^{(MF)}_0\rangle, |\psi^{(MF)}_1\rangle \dots |\psi^{(MF)}_{N_{max}}\rangle$ respectively. This vector defines a shell of states that are all related by an arbitrary permutation of the lattice sites leaving $(n_0, n_1, \dots, n_{N_{max}})$ unchanged. As a result, the number of states of a single shell is given by the multinomial coefficients

$$S(n_0, n_1, \dots, n_{N_{max}}) = \frac{N_{site}!}{\prod_{j=0}^{N_{max}} n_j!}, \tag{4.7}$$

and their probability is

$$p(n_0, n_1, \ldots, n_{N_{max}}) = \prod_{j=0}^{N_{max}} \left(p_j^{(MF)}\right)^{n_j}. \tag{4.8}$$

For example, the most probable shell is $(N_{site}, 0, \ldots, 0)$, which corresponds to the unique state where all sites are in $|\psi_0^{(MF)}\rangle$. The second most probable is $(N_{site}-1, 1, 0, \ldots, 0)$, for which one of the sites is in $|\psi_1^{(MF)}\rangle$ and all the others in $|\psi_0^{(MF)}\rangle$. We see that the selection of the state spanning the corner amounts to selecting the most probable shells, so that the number of total states in the corner is equal to M.

Once the M basis vectors of the corner space have been identified, the next task is to project all the operators governing the dynamics of the system on the corner space. One of the simplest ways to do so would be to write the matrix representation of the operators in the full space and delete afterwards the rows and columns corresponding to vectors laying outside of the corner space. However, for large lattices, this method requires the creation and manipulation of very large matrices. To avoid this difficulty, we have used an alternative way of projecting the operators on the corner space that is more efficient in terms of memory and do not require to write matrices in the full Hilbert space. Details on this procedure are presented in Appendix B.

At the end of step 2, we have at our disposal the matrix representation of all the relevant operators projected in the corner space.

Step 3: Determination of the steady-state density matrix in the corner space

The steady state of the system is determined by solving the master equation in the corner space. We assume that the master equation has the same form as Eq.(1.106), namely:

$$i\partial_t \rho = [H, \rho] + \frac{i\gamma}{2} \sum_{i=1}^{N_{site}} \left[2b_i \rho b_i^\dagger - b_i^\dagger b_i \rho - \rho b_i^\dagger b_i\right], \tag{4.9}$$

where all the operators are restricted to the corner space. There are several ways to find numerically the steady-states of Eq.(4.9). Usually, for a small corner space $\mathcal{C}(M)$, the fastest way is to solve Eq.(4.9) directly, in the vector space of operators on $\mathcal{C}(M)$, of which the density matrices form a convex set. This can be done by diagonalizing the Liouvillian superoperator

$$\mathcal{L} = [H, \bullet] - \frac{i\gamma}{2} \sum_{i=1}^{N_{sites}} \left[2b_i \bullet b_i^\dagger - b_i^\dagger b_i \bullet + \bullet\, b_i^\dagger b_i\right], \tag{4.10}$$

acting on ρ seen as a vector. Eigenvectors corresponding to the eigenvalue 0 are steady-states of the system. Alternatively, one can solve the differential equation Eq.(4.9) by using, e.g., Runge-Kutta algorithms, until the system reaches a stationary state.

These methods are fully deterministic and their precision is limited only by the performance of the diagonalization or time evolution algorithms. However, as they require to work in the space of operators, which has a dimension M^2, they are very demanding in terms of memory. In practice they are manageable as long as $M < 10^3$. When the dimension of the corner space is increased further, a Monte Carlo wave-function technique is needed [109, 110, 111, 112]. In this stochastic approach, which is detailed in Appendix A, the master equation is solved by averaging over quantum trajectories of pure states in presence of random quantum jumps. As the time evolution is performed on pure states, the matrices involved in the algorithm have a dimension M instead of M^2. With this technique, a size $M \sim 10^4$ is reachable, depending on the sparsity of the matrices.

Step 4: Increasing M until convergence is reached

The accuracy of the results is checked by increasing the size M of the corner space until convergence in the value of the observables is reached. We emphasize that in principle, by increasing arbitrarily M, the method becomes exact since the considered basis spans the entire Hilbert space. Of course, in practice, the method is useful when the number of states required to reach convergence is small enough to be treated numerically.

Note that although the basis spanning the corner space is formed by factorized states, with no correlations between different sites, the final steady-state may contain such correlations as it involves linear superpositions of the basis vectors.

4.1.2 Results

Although the method presented above is not restricted to any particular lattice model, we have first implemented it for the driven-dissipative Bose-Hubbard model on a 2×2 square lattice with periodic boundary conditions. For such a small number of sites, the size of the Hilbert space is reasonable. Setting a cutoff of $N_{max} = 4$ photons per site, the dimension of the total space is only $5^4 = 625$, which makes it possible to solve directly the master equation without resorting to wave-function Monte Carlo calculations. Figures 4.1 and 4.2 show the mean photon density and $g^{(2)}(0)$ in the steady-states, as a function of the number of states

in the corner. Results are shown for different values of the cut-off N_{max}. The parameters $F/\Delta\omega$ and $\gamma/\Delta\omega$ are the same as in the mean-field phase diagram presented in Fig.(3.9).

In Fig.(4.1) are shown the results for $U/\Delta\omega = 2$ and $J/\Delta\omega = 0.2$. As $J \ll U$ for this set of parameters (hereafter called point 1), we expect the mean-field approximation to be rather accurate. This is the case, since the deviation from mean-field is around 5%. As we have seen in Chap. 2, this value of U corresponds to the two-photon resonance, which explains that the (mean-field and exact) steady-states are reminiscent of the two-photon generalized Fock state defined in Eq.(2.41). Here, since $J \neq 0$ and $F/\Delta\omega = 0.4$, we are no longer in the very weak pumping regime, so the density is 0.9 instead of 1 and $g^{(2)}(0) = 0.6$ instead of 0.5. Note that this point of the phase diagram is located inside the monostable region according to the mean-field theory, so no bistability is expected to occur. Since the main purpose here is to benchmark the method, the study of bistability was postponed and will be included in future works.

We see from Fig.(4.1) that setting the maximum number of photons per site to 3 or 4 yields convergent results, which shows that $N_{max} = 4$ is enough to ensure that the cutoff on the number of photons does not affect the results. A cutoff of only 2 photons yields very poor results not shown on the figure. The maximum number of states in the corner is set to 305, which is more than enough to reach the exact steady states. Interestingly, the results obtained for 80 states are already a good approximation, with an error around 1%. For a 2×2 lattice, a Hilbert space of 80 states is smaller than a Fock space with a maximum of two photons per sites, which shows that for a point where the mean-field theory is a good approximation, our way of selecting the corner is more efficient than a simple truncation of the full Fock space.

In contrast with the first point, the second point of the phase diagram as been chosen in a region where the validity of the mean-field theory is not clear a priori. Indeed, the values of $U/\Delta\omega = 4$ and $J/\Delta\omega = 1.5$ correspond to the unstable region of the mean-field phase diagram. The discrepancy is confirmed by the results of Fig.(4.2). Indeed, the density in the steady-state of the 2×2 lattice is 5 times higher than the mean-field value and $g^{(2)}(0) = 2.4$ instead of 0.95. Note that since the density of photons is much smaller than for the previous point, a cutoff of 3 photons per site is already enough. For this set of parameters, reaching the stationary solution within the corner still requires less states than with the full Fock space, but the convergence speed is not as good as in the previous case. This is not surprising since the selection of the states is based on a approximate density matrix that is very far from the exact result.

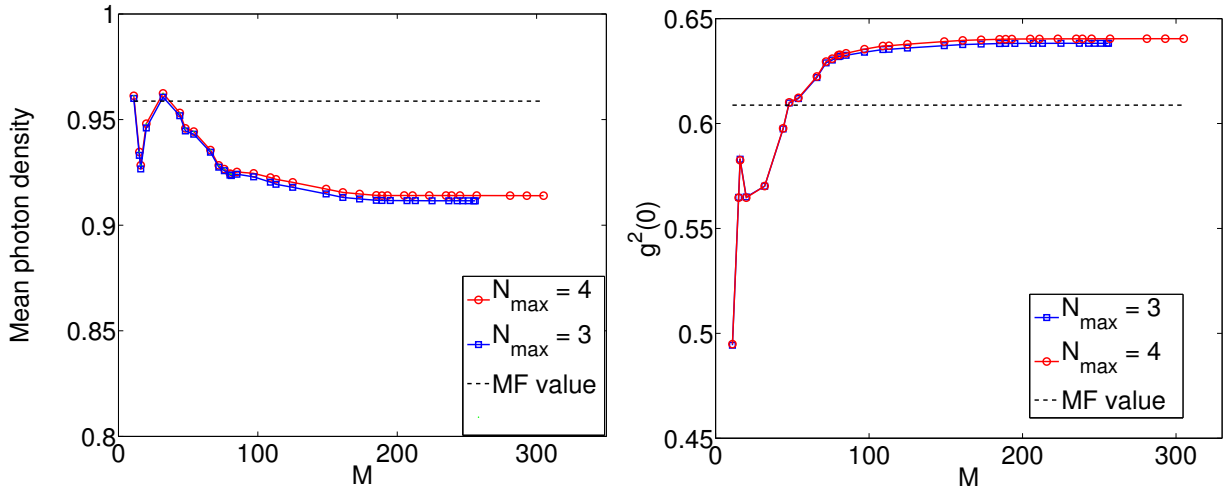

Figure 4.1: Mean photon density and $g^2(0)$ as a function of the number of states in the corner space for a 2×2 lattice. Point 1: $U/\Delta\omega = 2$, $J/\Delta\omega = 0.2$, $F/\Delta\omega = 0.4$, $\gamma/\Delta\omega = 0.2$. Dashed black line: mean-field solution

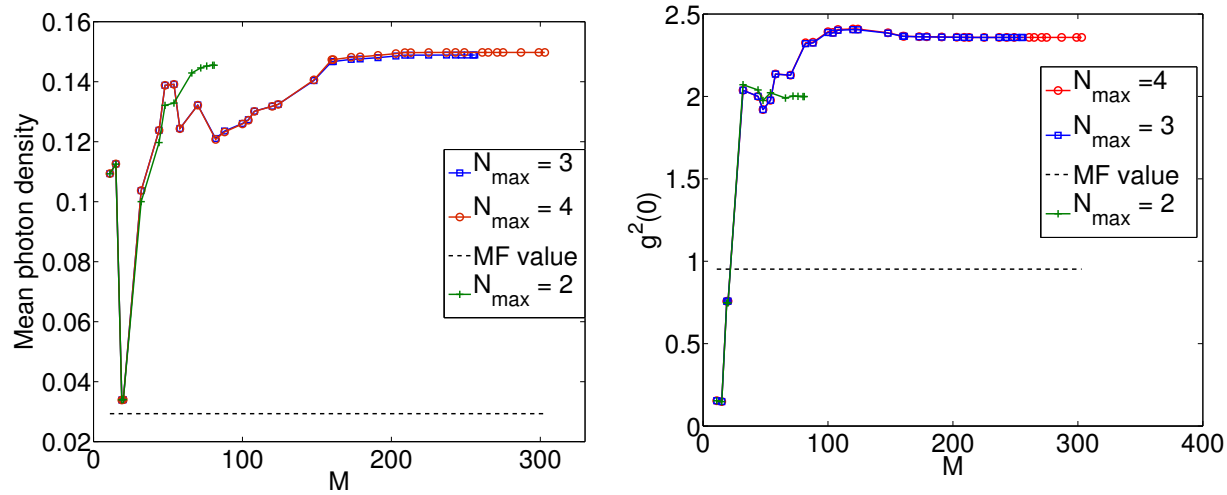

Figure 4.2: Mean photon density and $g^2(0)$ as a function of the number of states in the corner space for a 2×2 lattice. Point 2: $U/\Delta\omega = 4$, $J/\Delta\omega = 1.5$, $F/\Delta\omega = 0.4$, $\gamma/\Delta\omega = 0.2$. Dashed black line: mean-field solution.

For the 2×2 lattice, there was no need to use the wave-function Monte Carlo method outlined at the beginning of this chapter. This is no longer the case with the 3×3 lattice. For this size, a cutoff of 3 photons per site, yields a Hilbert space of dimension $4^9 = 262144$ and the numerical calculations become much heavier. Results for the point 1 of the phase diagram ($U/\Delta\omega = 2$ and $J/\Delta\omega = 0.2$), are reported in the left panel of Tab.(4.1). We have calculated the mean photon density and $g^{(2)}(0)$ for up to 55 395 states in the corner. Given the performance of the method on the 2×2 lattice, which already gives good results for a corner size corresponding to 3 states per site (81 states), the results on the 3×3 for this size of the corner should be close to the exact solution. Indeed, 3 states per site on a 3×3 lattice correspond to $3^9 = 19683$ states. Note that the values of the observables are closer to the mean-field solution for the 3×3 lattice than for the 2×2 lattice. For the former, the discrepancy is around 3%.

We have already noted that for the second point ($U/\Delta\omega = 4$ and $J/\Delta\omega = 1.5$), the exact stationary solution is very far from the mean-field solution, and as a result, the method is less efficient. This is of course more problematic in the case of a 3×3 lattice, since the full Hilbert space is much larger. In fact, we were not able to reach convergence with this approach for this lattice size. This is also explained by the fact that, if the solution we are looking for is very far from the mean-field result, the time necessary to reach the steady state is also longer, thereby slowing down the calculations even more. As an alternative, results for $U/\Delta\omega = 4$ but $J/\Delta\omega = 0.2$ are shown in the right panel of Tab.(4.1). For this smaller value of the tunneling strength, the mean-field approximation works better and convergence is reached for less than 7000 states.

These few examples on 2×2 and 3×3 lattices already bring to light the potentials and shortcomings of this first attempt at selecting a relevant corner of the Hilbert space. When the mean-field approximation is accurate, this new method is indeed much more efficient than a direct simulation in the Fock basis. It allows for a finer modulation of number of states than a simple truncation of the Fock space so that convergence is reached, in the best-case scenario, with a much smaller number of states. Moreover, once convergence is reached, arbitrary precision is achievable. We have seen however that as soon as deviations for the mean-field results become significant, the state selection based on this approximate density matrix does not lead to a fast convergence. Furthermore, even when the number of states is significantly reduced when compared to the truncated Fock space, the size of the corner is still expected to grow exponentially with the number of lattice sites. For example, if the corner method reduces the number of states per site that have to be taken into account

N_{max}	$\langle b^\dagger b\rangle$	$g^{(2)}(0)$
463	0.1273(1)	0.841(1)
835	0.1282(2)	0.856(2)
1978	0.1279(2)	0.864(2)
3788	0.1286(5)	0.860(4)
6713	0.1284(2)	0.862(2)
MF	0.1250	0.8359

N_{max}	$\langle b^\dagger b\rangle$	$g^{(2)}(0)$
3851	0.955(1)	0.5950(8)
7136	0.947(1)	0.6115(8)
26595	0.941(3)	0.623(2)
55395	0.936(3)	0.627(2)
MF	0.9587	0.6088

Table 4.1: Mean photon density and $g^{(2)}(0)$ for a 3×3 lattice, corresponding to two different points in the phase diagram and calculated with the method of Sec. 4.1. For each point, results are shown for different sizes of the corner space. For both points, $F/\Delta\omega = 0.4\gamma/\Delta\omega = 0.2$ and $J/\Delta\omega = 0.2$. The left table correspond to $U/\Delta\omega = 4$, and the right one to $U/\Delta\omega = 2$. The error on the last significative digit is due to to finite Monte Carlo sampling and the last row corresponds to the mean-field prediction.

form 4 to 3, as it is the case for the point 1 discussed above, simulations on lattices larger than 3×3 are already out of reach.

This limitation is essentially due to the fact that the selection of the states forming the corner is based on a single-site mean-field density matrix. More precisely, by starting from mean-field density matrix, we end up with a corner spanned by tensor products of N single-site states. Consequently, the method can be improved by taking as a basis for the corner, not products of single-site states but products of states that already include several sites. An implementation of this idea, related to the spatial renormalization group approach is presented in the next section.

4.2 Corner space renormalization method

4.2.1 General principles of the method

The idea behind the second and more sophisticated approach that we have explored is to construct the corner space by taking products of states belonging to two lattices of smaller size, for which we know the exact density matrix. An efficient way to simulate large lattices is then to iterate the procedure, so as to double the size of the system at each iteration. On this specific point, the method is close to the spirit of Wilson's spatial renormalization group [99]. The steps of this Corner Space Renormalization method are the following:

1. Determine the steady-state density matrix for small lattices, for which an exact inte-

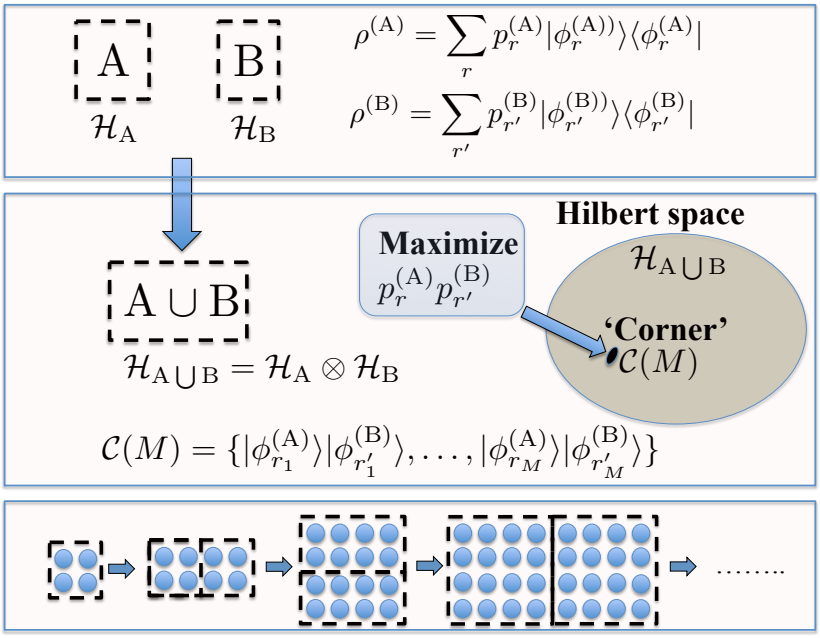

Figure 4.3: Sketch describing the general idea and ingredients of the Corner Space Renormalization method.

gration of the master equation is possible.

2. Merge spatially two of these lattices and select the M most probable product states as a basis for the corner space.

3. Determine the steady-state solution of the density matrix in the corner space.

4. Increase M until convergence is reached.

5. In order to simulate a larger lattice, go back to step 2.

These different steps are summarized in Fig.(4.3). Steps 3 and 4 of this algorithm are the same as in the previous one. The main difference between the two lies in steps 2 and 5, which are detailed below.

Step 2: Merging of two lattices and selection of the most probable states spanning the corner

Let us suppose that we know the steady-state density matrices $\rho^{(\mathrm{A})}$ and $\rho^{(\mathrm{B})}$ for two lattices A and B. The goal is to use these solutions to select the relevant corner for the larger lattice obtained by merging spatially A and B. Note that the corresponding Hilbert space is then $\mathcal{H}_{(\mathrm{A}\cup\mathrm{B})} = \mathcal{H}_{\mathrm{A}} \otimes \mathcal{H}_{\mathrm{B}}$ where $\mathcal{H}_{\mathrm{A}}$ and $\mathcal{H}_{\mathrm{B}}$ are the Hilbert spaces of systems A and B.

The procedure for selecting the most relevant states is then quite similar to what has been presented previously. Each density-matrix operator can be diagonalized as:

$$\rho^{(\mathrm{A})} = \sum_r p_r^{(\mathrm{A})} |\phi_r^{(\mathrm{A}))}\rangle\langle\phi_r^{(\mathrm{A})}|, \tag{4.11}$$

where the states $|\phi_r^{(\mathrm{A})}\rangle$ form an orthonormal basis for the Hilbert space $\mathcal{H}_{\mathrm{A}}$ of A and p_r^{A} are the corresponding probabilities (analogous notations hold for the quantities relating to the other subsystem B). The corner is then spanned by the most probable states of the form

$$|\phi_{r_j}^{(\mathrm{A})}\rangle \otimes |\phi_{r'_j}^{(\mathrm{B})}\rangle, \tag{4.12}$$

according to their joint probability $p_{r_j}^{(A)} p_{r'_j}^{(B)}$. As in the previous section the rank indices are such that:

$$p_{r_1}^{(\mathrm{A})} p_{r'_1}^{(\mathrm{B})} \geq p_{r_2}^{(\mathrm{A})} p_{r'_2}^{(\mathrm{B})} \geq ... \geq p_{r_M}^{(\mathrm{A})} p_{r'_M}^{(\mathrm{B})}, \tag{4.13}$$

and the corner space is spanned by the orthonormal basis states

$$\{|\phi_{r_1}^{(\mathrm{A})}\rangle|\phi_{r'_1}^{(\mathrm{B})}\rangle, |\phi_{r_2}^{(\mathrm{A})}\rangle|\phi_{r'_2}^{(\mathrm{B})}\rangle, ..., |\phi_{r_M}^{(\mathrm{A})}\rangle|\phi_{r'_M}^{(\mathrm{B})}\rangle\}. \tag{4.14}$$

The lattices A and B are not necessarily identical and the code we have developed is designed to be as general as possible. The properties of a lattice and its associated Hamiltonian is encoded in a specific class of objects. In particular, the geometry of the lattice is stored as an attribute of this class. The merging of two lattices is then done by defining a new instance of the class with a new geometry, and by building all the operators associated with this new geometry. To be compatible with different types of lattices, the geometry is defined by the links between the sites. In view of the merging procedure, it was also useful to distinguish between internal and external links: external links represent the boundary conditions and are the one that may be broken and redefined when connecting two lattices together, while internal links do not change in the merging process.

Once the geometry of the new lattice $A \cup B$ is defined, the next task is to compute the operators in the new corner. The tunneling operators that correspond to internal links in the lattice as well as all the operators acting only on a single site of the lattice, can be

constructed in the same way. Let us take the example of an annihilation operator. If a site j belongs to lattice B, then

$$b_j = I^{(\mathrm{A})} \otimes b_j^{(\mathrm{B})}, \tag{4.15}$$

where $I^{(\mathrm{A})}$ is the Identity matrix acting in the Hilbert space $\mathcal{H}_{\mathrm{A}}$. The expression for the tunneling operators connecting the two lattice is of the form:

$$b_i^\dagger b_j = b_i^{(\mathrm{A})\dagger} \otimes b_j^{(\mathrm{B})}, \tag{4.16}$$

where the two sites i and j, belong to lattice A and B respectively. The new Hamiltonian is then defined by:

$$H^{(\mathcal{C})} = H^{(\mathrm{A})} \otimes I^{(\mathrm{B})} + I^{(\mathrm{A})} \otimes H^{(\mathrm{B})} + J_{\mathrm{A-B}}, \tag{4.17}$$

where $H^{(\mathrm{A})}$ and $H^{(\mathrm{B})}$ are the Hamiltonians of the lattices A and B, and $J_{\mathrm{A-B}}$ is an operator including all tunneling operators coupling the two lattices. The latter is therefore defined by:

$$J_{\mathrm{A-B}} = -J \sum_{<i\in\alpha, j\in\beta>} \left(b_i^{(\mathrm{A})\dagger} \otimes b_j^{(\mathrm{B})} + b_i^{(\mathrm{A})} \otimes b_j^{(\mathrm{B})\dagger} \right), \tag{4.18}$$

where α and β denote the sites on the common edge of the two lattices. Of course, the size of the corner is most of the time much smaller than the Hilbert space $\mathcal{H}_{(\mathrm{A}\cup\mathrm{B})}$. This means that in the matrix representation of the operators defined above, only rows and column corresponding to states belonging to the selected corner are to be kept.

Step 5: Iteration of the procedure

For homogeneous systems, an efficient way to iterate the procedure is to choose A and B as identical, so as to double the size of the system at each iteration. This iterative process makes this method much more powerful than the one described in the previous section. Indeed, with this approach the knowledge gained in simulating a N-site lattice is exploited to solve the $2N$-site problem, whereas it is "waisted" if one starts from the mean-field density matrix for each lattice size.

Besides, in the Corner Space Renormalization method, correlations between sites are treated exactly within the subsystems A and B. As a result, a selection of the states based on the approximate density matrix $\rho^{(\mathrm{A})} \otimes \rho^{(\mathrm{B})}$ is more efficient than the one based on the single-site mean-field solution $\bigotimes_{i=1}^{N} \rho_{\mathrm{MF}}$.

M	$\langle b^\dagger b\rangle$	$g^{(2)}(0)$	$g^{(2)}_{<j,l>}$
20	0.0902	1.646	1.28
50	0.1006	1.513	1.34
100	0.1044	1.454	1.26
200	0.0968	1.324	1.51
400	0.1006	1.291	1.51
800	0.1009(2)	1.242(3)	1.57(2)
1600	0.1014(2)	1.226(3)	1.58(2)
3200	0.1002(2)	1.185(2)	1.63(2)
6400	0.0994(2)	1.179(3)	1.63(1)

Table 4.2: Steady-state expectation values obtained with the Corner Space Renormalization method. Parameters: 4×4 square lattice with periodic boundary conditions, $U/\Delta\omega = 4$, $J/\Delta\omega = 0.6$, $F/\Delta\omega = 0.4$, $\gamma/\Delta\omega = 0.2$. A number $N_{max} = 3$ of bosons per site is required to reach convergence. In this case, the dimension of the full Hilbert space is $4^{16} \simeq 4.3 \cdot 10^9$.

4.2.2 Results

To benchmark the method, we have first considered a 4×4 lattice with periodic boundary conditions. The exact steady-state was first computed for a 2×2 lattice. The lattice was then doubled twice, to reach 4×2 and 4×4. Results for $U/\Delta\omega = 4$ and $J/\Delta\omega = 0.6$ are reported in Tab.(4.2). For this value of the tunneling strength, deviations from the mean-field theory are important (around 20%). We see that the number of states in the corner required to reach convergence is 6 400, which is significantly less than the 55 593 that were needed for the 3×3 lattice with the first approach. However, when in the previous section we computed the operators by starting from the mean-field density matrix, the matrices obtained were very sparse in the corner basis. The doubling procedure, on the other hand, does not yield sparse matrices. Indeed, the states spanning the corner already contain correlations between sites, so the operators do not have in general a sparse representation in this basis. In a certain sense, all the unnecessary information contained in the sparse matrices of the first approach is gradually eliminated in the successive iteration of the doubling procedure. From a practical point of view, this means that it would not be possible with our current resources to handle a corner of 50 000 states using the second method. The maximum is more likely to be between 8000 and 10 000 (the main limitation is the memory of our computer cluster).

In order to characterize the deviation from mean-field theory in a more precise way, we

have computed the nearest-neighbor correlation function:

$$g^{(2)}_{<j,l>} = \frac{\langle b_j^\dagger b_l^\dagger b_j b_l \rangle}{\langle b_j^\dagger b_j \rangle \langle b_l^\dagger b_l \rangle}. \tag{4.19}$$

Note that we recover the on-site correlation function $g^{(2)}(0)$ for $i = l$. By definition this function is constant and equal to 1 for the mean-field solution. As seen is Tab.(4.2), $g^{(2)}_{<j,l>} \simeq 1.6$ in the stationary solution, which confirms that this method is able to restore correlations between neighboring sites that are neglected at the mean-field level.

We have also tried to combine this second method with the first one. We have calculated the steady-states for a 3×3 lattice using the first method (which is still much more efficient than using a truncated Fock basis), and used this result to simulate a 3×6 lattice. An example of time evolution for different lattice sizes is shown in Fig.(4.4). The parameters of the Hamiltonian are the same as in Tab.(4.2). We see that, although the deviation from the mean-field solution remains significant, it decreases as the system size is increased. What is even more interesting is that close results are obtained for 3×3, 4×4 and 6×3 lattices, indicating that we are approaching the result for the thermodynamical limit.

A summary of all the results obtained so far is presented in Tab.(4.3). Remarkably, the corner size (necessary to reach convergence) does not grow exponentially with the size of the lattice but seems to follow a power law. It is however too early to establish any precise scaling behavior. In particular, the performance of the method depends strongly on the parameters of the Hamiltonian. For hard-core ($U = \infty$), or weakly interacting bosons ($U \to 0$), accurate results can be reached very quickly. The convergence is much slower in strongly correlated phases, when U and J are of the same order of magnitude and both large when compared with the other parameters of the system.

Another conclusion to be drawn from Tab.(4.3) is that mean-field theory works quite well for small values of $J/\Delta\omega$, of the order of 0.2.

4.3 Conclusion and outlook

In order to go beyond the mean-field approximation in our investigation of the driven-dissipative Bose-Hubbard model, we have developed a new numerical method for simulating driven-dissipative arrays of cavities that is well suited for handling lattices with more than one spatial dimension. The general idea behind this method is to select a small corner of the Hilbert space, where the master equation for the density matrix is solved by using, e.g,, a wave-function Monte Carlo algorithm.

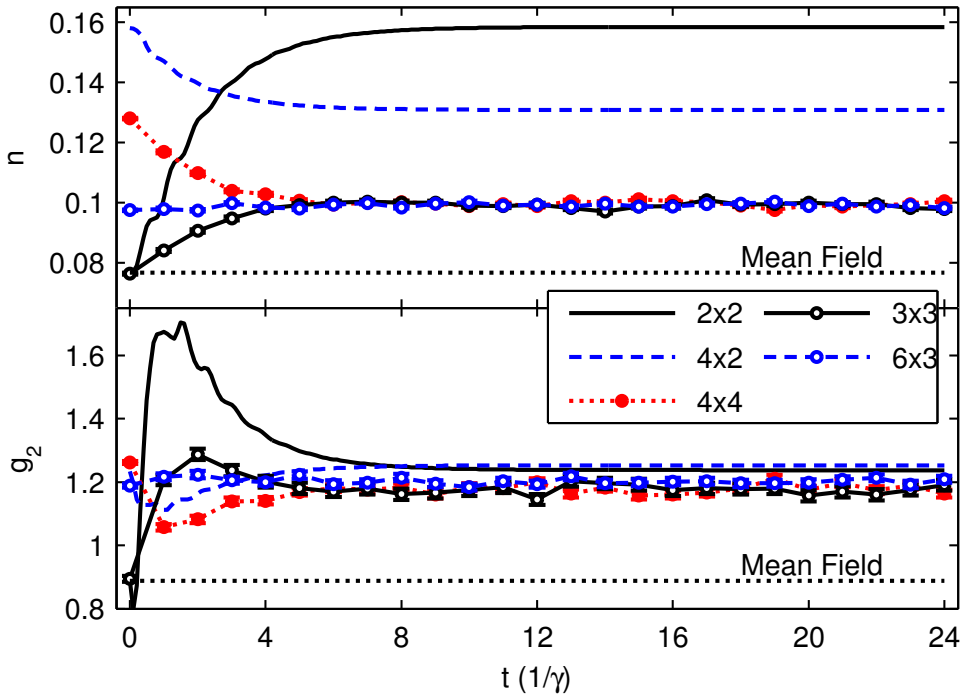

Figure 4.4: Evolution of $n = \langle b^\dagger b \rangle$ and $g^{(2)}(0)$ as a function of time t (units of $1/\gamma$) on lattices of various size. Solid lines represent evolutions performed by direct integration of the master equation, while points depict wave-function Monte Carlo calculations. When error bars are not shown, the statistical error is smaller than the point size. Parameters as in Table 4.2.

The challenging part of the task is of course to find the most relevant corner space. To do so, we selected, as a basis for the corner, the most probable eigenstates of an approximate density matrix. A first implementation of this general scheme was carried out by choosing the mean-field solution as the approximate density matrix. This approach proved to be more efficient than a direct simulation of the master equation in a truncated Fock basis and showed that mean-field theory worked well for small values of J. However, the method provided satisfactory results only when the deviation from the mean-field solution was small. In particular convergence of the results with the size of the corner was too slow to be able to capture accurately strong correlations between the lattice sites.

To overcome these limitations and select the corner space on the basis of more accurate density matrix, we developed an iterative procedure allowing to use the solution for a lattice of size N to compute the steady-state of a lattice of size $2N$. This second approach is very promising as the size of the corner appears not to grow exponentially with the lattice size.

The work presented in this chapter is still in progress and is part of a project involving

Parameters		Mean-field		Corner method				
$U/\Delta\omega$	$J/\Delta\omega$	$\langle b^\dagger b\rangle$	$g^{(2)}(0)$	N_{sites}	M	$\langle b^\dagger b\rangle$	$g^{(2)}(0)$	$g^{(2)}_{\langle j,l\rangle}$
∞	0.2	0.0953	0	8×4	1600	0.09527(2)	0	1.0436(3)
				8×8	8000	0.0948(2)	0	1.0237(6)
4	0.2	0.125	0.836	4×4	3200	0.1281(4)	0.859(4)	1.172(5)
				6×3	6400	0.1282(9)	0.858(9)	1.173(4)
4	0.6	0.0768	0.8879	4×4	6400	0.0994(2)	1.179(3)	1.63(1)
				6×3	6400	0.0992(1)	1.202(4)	1.65(1)
2	0.2	0.9587	0.6088	4×2	6400	0.9275(8)	0.631(1)	1.0127(8)
				3×3	8000	0.9281(9)	0.617(1)	1.0069(6)
0.2	0.2	0.1156	1.265	8×8	400	0.1156	1.260	0.9883
				16×8	600	0.1156	1.259	0.9897
0.1	0.2	0.1126	1.112	16×8	400	0.1126	1.1107	0.9950
				16×16	400	0.1126	1.1105	0.9941
0	0.2	0.1103	1	8×4	200	0.1103	0.9995	1.000
				8×8	400	0.1103	0.9995	1.000

Table 4.3: Steady-state expectation values obtained with the corner space renormalization method for lattices with different sizes and parameters (periodic boundary conditions). Mean-field results are also reported for comparison. Parameters: $F/\Delta\omega = 0.4$ and $\gamma/\Delta\omega = 0.2$. The maximum number of bosons per site is $N_{max} = 1$ for hardcore bosons, $N_{max} = 3$ for $U/\Delta\omega = 4, 2$ and $N_{max} = 4$ for $U = 0$.

several members of the group. There is room for numerous improvements in the efficiency of the method but it is clear that our approach has the potential to become a precious tool to explore the physics of driven-dissipative quantum systems with more than one spatial dimensions and to benchmark analytical theories for such systems. In particular, future studies may include disorder, geometric frustration as well as artificial gauge fields.

General conclusion and outlook

The tremendous experimental advances in solid-state cavity and circuit quantum electrodynamics have opened the way to the realization of arrays of nonlinear cavities where the on-site effective photon-photon interactions are large enough to enter the strongly correlated regime. As we have seen in Chapter 1, such arrays of cavities can be accurately described by a driven-dissipative version of the Bose-Hubbard model where photon losses are compensated by an external pump laser. The main task of this PhD thesis was to study the steady-state phases of this quantum model. Unfortunately, in its general formulation and for an arbitrary large number of cavities, this problem is far too complicated to be solved exactly and some approximations must be performed.

In Chap. 2 and 3 we have considered an infinite array with periodic boundary conditions, and computed the steady-states within the framework of the mean-field approximation. The main simplifying assumption was to take a factorized Gutzwiller ansatz for the density matrix. In Chapter 2, this approach was first applied to the driven-dissipative model in the limit of weak pumping and weak dissipation. Exploring this regime was very fruitful to gain a clear understanding of the relation between the better-known equilibrium Bose-Hubbard model and its driven-dissipative counterpart. In particular, an equivalent of the Mott-insulating state was found in the form of statistical mixtures of Fock states with half the photon density of a pure Fock state but with the same value of the second-order correlation function $g^{(2)}(0)$. These nonclassical states of light arise when the laser frequency is tuned so as to be at resonance with multiphotonic absorption processes. It was shown that these states survive up to a critical value of the coupling between the cavities above which a crossover to (classical) quasi-coherent states occurs. The study of the weak dissipation and weak pumping regime also revealed that outside of the multiphotonic resonances, a lower density of photons could be associated with strong fluctuations in the photon statistics, leading to the phenomenon of "photon superbunching" in the vicinity of the two-photon resonance.

The mean-field approach was extended in Chapter 3 to arbitrary pumping and dissi-

pation. By using an exact solution of the single-cavity problem based on the complex P-representation of the density matrix, a general phase diagram was established. A general feature of this diagram is the appearance of bistability induced by the coupling between the cavities. Indeed, in a large portion of the parameter space, two stable mean-field steady-states were found. The properties of the different phases in the bistable region are related to the types of state uncovered in Chapter 2: one phase shows a low density of photons and strong bunching while the other has a much higher density of photons and exhibits antibunching, in accordance with what was found for the multiphotonic resonances. Interestingly, stability studies also revealed that for some values of the parameters in the monostable region, the unique mean-field solution is unstable. These instabilities are triggered by a purely imaginary excitation branch, which has no equivalent at equilibrium, and indicates the formation of inhomogeneous patterns in the system.

The main motivation behind the use of the mean-field approximation was its successful prediction of the Mott-insulator-to-superfluid transition in the equilibrium model. However, this approximation is not fully controlled a priori and the need arose to test it against other more accurate results. To do so, we have performed numerical simulations on finite-size arrays of cavities. The main challenge is that the dimension of the associated Hilbert space grows exponentially with the number of cavities, making brute-force simulations of large arrays impossible. In order to circumvent this difficulty, we have solved the master equation in a "small corner" of the Hilbert space containing the most relevant states. The accuracy of the results was controlled by increasing the dimension of the corner space until convergence is reached. Applying this "corner method" to the driven-dissipative Bose-Hubbard model, we showed that for small values of the coupling between cavities, the mean-field theory is a good approximation. Significant deviation occurs when J is increased and competes with the on-site interaction U. These first results are part of an ambitious project involving several members of the group and offer numerous perspectives. Concerning the method itself, an important task will be to determine precisely how the corner size scales with the number of cavities. More importantly, the method that we have developed is quite general and can be applied to a great variety of driven-dissipative lattice models. In particular, future studies could explore the physics of 2D arrays of nonlinear cavities with complex elementary cells (including disorder), geometric and spin frustration as well as the role of artificial gauge fields in extended lattices. As witnessed by the numerous conferences, workshops and summer schools organized on the topic, many-body physics with light is a vibrant research field and I hope to have convinced the reader of its interest.

Appendices

Appendix A

Wave-function Monte Carlo algorithm

We present in this appendix the wave-function Monte Carlo technique [109, 110, 111, 112].

The time evolution of the system is assumed to be governed by a Lindblad master equation of the form

$$\frac{d\rho}{dt} = i[\rho, H] + \sum_i \left[C_i \rho C_i^\dagger - \frac{1}{2}\left(C_i^\dagger C_i \rho + \rho C_i^\dagger C_i \right) \right], \tag{A.1}$$

where we have introduced a slightly different notation than in the rest of the manuscript: the dissipation rate γ has been absorbed in the operators C_i describing the relaxation of the system due to the interaction with the external bath. This expression is quite general, and in the case of optical cavities, these operators are given by

$$C_i = \sqrt{\gamma_i} b_i, \tag{A.2}$$

The general principle of the wave-function Monte Carlo technique is to compute the density matrix of the system by averaging over stochastic realizations of pure states, whose evolution is such that it reproduces the master equation. In other words, we want to write the density matrix as

$$\rho(t) = \overline{|\psi(t)\rangle\langle\psi(t)|}, \tag{A.3}$$

where the overline denotes an average over all possible quantum trajectories of the pure states. To see how this can be done, let us write the time evolution of a density matrix of the form $\rho = |\psi\rangle\langle\psi|$ obeying the master equation, between times t and $t + dt$:

$$\rho(t+dt) = (1 - idtH')|\psi(t)\rangle\langle\psi(t)|(1 + idtH'^\dagger) + \sum_k dt C_k |\psi(t)\rangle\langle\psi(t)| C_k^\dagger + O(dt^2), \tag{A.4}$$

where, we have introduced a nonhermitian Hamiltonian

$$H' = H - \frac{i}{2}\sum C_i^\dagger C_i. \tag{A.5}$$

We see that Eq.(A.4) can easily be rewritten in term of a statistical mixture of pure states:

$$\rho(t+dt) = (1 - \sum_i \delta p^{(i)})|\psi_0\rangle\langle\psi_0| + \sum_i \delta p^{(i)}|\psi_i\rangle\langle\psi_i|, \tag{A.6}$$

with

$$|\psi_0\rangle = \frac{e^{-iH'dt}|\psi(t)\rangle}{\langle\psi(t)|e^{+iH'^{\dagger}dt}e^{-iH'dt}|\psi(t)\rangle^{1/2}}, \tag{A.7}$$

$$|\psi_i\rangle = \frac{C_i|\psi(t)\rangle}{\langle\psi(t)|C_i^{\dagger}C_i|\psi(t)\rangle^{1/2}}, \tag{A.8}$$

$$\delta p^{(i)} = \langle\psi(t)|C_i^{\dagger}C_i|\psi(t)\rangle dt. \tag{A.9}$$

Note that in Eq.(A.6), we have used

$$\langle\psi(t)|e^{+iH'^{\dagger}dt}e^{-iH'dt}|\psi(t)\rangle = 1 - \sum_i \delta p^{(i)} = 1 - \delta p, \tag{A.10}$$

which is guaranteed by the relation $\mathrm{Tr}[\rho] = 1$.

The way to proceed is then to chose randomly at each time step one of the states $|\psi_i\rangle$ or $|\psi_0\rangle$ according to the probability distribution $\delta p^{(i)}$. Formulated in this way, the time evolution appears as a continuous evolution under the nonhermitian Hamiltonian H', randomly interrupted by quantum jumps. These jumps physically correspond to the loss of one quantum from the system due to the interaction with the bath and are implemented by applying one of the operators C_i to the wave-function. By construction, the density matrix obtained by averaging over all trajectories is solution of the master equation Eq.(A.1).

A simple implementation of this algorithm consists in performing the time evolution with a constant time step δt. After each step, one decides whether to make a jump and in which channel, according to the statistical distribution determined by $\delta p^{(i)}$. If a jump is made in channel i, than the wave function at time $t + \delta t$ becomes

$$|\psi(t+\delta t)\rangle = |\psi_i\rangle \tag{A.11}$$

while if no jump occurs

$$|\psi(t+\delta t)\rangle = |\psi_0\rangle. \tag{A.12}$$

Note that, to ensure accurate results, δt must be much less than $1/\gamma_i$, for any i. This implies that the probability of making a quantum jump δp is very small at any t. To perform the evolution of the wave function in a more efficient way, the times t_j at which jump occurs can be randomly determined according to the statistical distribution of the

time T elapsed between two successive quantum jumps [113]. This allows one to perform the time evolution between two jumps with a more efficient algorithm, such as an adaptive Runge-Kutta method. If the Hilbert space is small enough and the Hamiltonian does not explicitly depend on time, one can also diagonalize the nonhermitian Hamiltonian H' and compute the evolution operator $e^{i\hat{H}'(t_{j+1}-t_j)}$ between two jumps by directly evaluating the exponential of the complex eigenvalues of H'. However this new basis is not orthonormal and the change-of-basis matrix P is not unitary, since $\hat{H}'$ is not Hermitian. One must then introduce a nontrivial scalar product $S = (P^\dagger P)^{-1}$ to compute the expectation values of the observables.

To find the statistical distribution of T, one can divide T in n small finite intervals δt. The probability of making a jump between time t_n and $t_n + \delta t$, after a time $T = t_n - t_0$ from the last jump at $t = t_0$ is

$$\delta P(T) = \delta p_n \prod_{m=0}^{n-1} (1 - \delta p_m), \tag{A.13}$$

where δp_m is the probability of making a jump at time t_m. The product in the right hand side of Eq. (A.13) is computed by recursively using Eqs. (A.12) and (A.10),

$$|\psi_n\rangle = \frac{e^{-iH'_{n-1}\delta t}|\psi_{n-1}\rangle}{(1-\delta p_{n-1})^{1/2}} = \prod_{m=0}^{n-1} \left(\frac{e^{-iH'_m \delta t}}{(1-\delta p_m)^{1/2}} \right) |\psi_0\rangle. \tag{A.14}$$

and noting that by construction $\langle\psi_n|\psi_n\rangle = 1$, we have:

$$\delta P(T) = \delta p_n \langle\psi_0| \prod_{l=0}^{n-1} \left(e^{iH_l'^\dagger \delta t} \right) \times \prod_{m=0}^{n-1} \left(e^{-iH'_m \delta t/\hbar} \right) |\psi_0\rangle. \tag{A.15}$$

In the continuous limit,

$$dP(T) = dp(t) \langle\psi(t_0)| e^{i\int_{t_0}^{t_0+T} dt\, H'^\dagger(t)} \times e^{-i\int_{t_0}^{t_0+T} dt\, H'(t)} |\psi(t_0)\rangle. \tag{A.16}$$

In the Monte Carlo evolution, if ϵ is a random number between 0 and 1, T is determined by solving

$$\langle\psi(t_0)| e^{i\int_{t_0}^{t_0+T} dt, H'^\dagger(t)} \times e^{-i\int_{t_0}^{t_0+T} dt\, H'(t)} |\psi(t_0)\rangle = \epsilon. \tag{A.17}$$

If H' does not depend on time, this reduces to solve

$$\langle\psi(t_0)| e^{iH'^\dagger T} \times e^{-iH'T} |\psi(t_0)\rangle = \epsilon. \tag{A.18}$$

Working in a basis where H' is diagonal, the solution of this equation requires a relatively short computation time.

Appendix B

Projection of the operators on the corner space

In this appendix, we present the algorithm used in the first type of "corner method" based on the mean-field solution (see Section 4.1), to project the operators on the corner space without having to write their matrix representation in the full Hilbert space.

The algorithm relies on the fact that the total Hilbert space of a N-site lattice is a tensor product of single-site Hilbert spaces. In particular, all the creation and destruction operators from which the total Hamiltonian is constructed, are operators acting on a single site only. As a result, they can be written as a tensor product of single-site operators. For example, the operator annihilating a particle on the first site of the lattice reads

$$b_1 = b \otimes I \otimes \cdots \otimes I, \tag{B.1}$$

with b and I the annihilation and identity operators respectively, in the single-site Hilbert space.

Projecting these operators in the corner will then amount to deleting, in the total tensor-product matrix, the superfluous rows and columns corresponding to discarded states. The total matrix however may very well be too big to be computed directly. Besides it contains a great deal of unnecessary information that will be erased by the projection process.

To avoid theses difficulties, we will construct the projected operator iteratively, by adding the sites one by one and eliminating as much useless information as possible at each iteration, thus avoiding to compute the matrix in the total Hilbert space.

In order to understand better the principle of this method, let us take the example of an operator $H = h^{(1)} \otimes h^{(2)}$ acting on a space $E_1 \otimes E_2$. The operator H may be written in the

form:

$$H = \sum_{i_1,j_1,i_2,j_2} h^{(1)}_{j_1 i_1} h^{(2)}_{j_2 i_2} |j_1 j_2\rangle\langle i_1 i_2|, \tag{B.2}$$

where i_1, j_1, i_2, j_2 are indices labeling the states in the single-site Hilbert space. In its general formulation, the projection of H is done by deleting the rows and columns related to the states $|j_1 j_2\rangle$ that lie outside the corner, after having computed the tensor product $h^{(1)} \otimes h^{(2)}$. However, this operation can be simplified whenever there exist some states $|l_1\rangle$ (belonging to E_1) for which all the states $|l_1 j_2\rangle$ are outside of the corner space, no matter what value the index j_2 takes. Under such circumstances, it is possible, without changing the final result, to suppress the superfluous rows and columns directly in the matrix $h^{(1)}$ before performing the tensor product $h^{(1)} \otimes h^{(2)}$.

The main advantage of this method is that the biggest operator that we need to consider is now

$$\tilde{H} = \sum_{i_1,j_1,i_2,j_2} \tilde{h}^{(1)}_{j_1 i_1} h^{(2)}_{j_2 i_2} |j_1 j_2\rangle\langle i_1 i_2|, \tag{B.3}$$

where $\tilde{h}^{(1)}$ is the operator $h^{(1)}$ without the superfluous rows and columns.

Proceeding in an iterative way, the method can be extended to the general case of an operator

$$A = \bigotimes_{i=1}^{N} a_i, \tag{B.4}$$

acting on the Hilbert space

$$\mathcal{H} = \bigotimes_{i=1}^{N} E_i. \tag{B.5}$$

It is particularly efficient when in the M product states $\{|\psi^{(MF)}_{r_j,1}\rangle|\psi^{(MF)}_{r_j,2}\rangle \dots |\psi^{(MF)}_{r_j,N_{site}}\rangle\}$ spanning the corner space, most of the sites are in the fundamental state $|\psi^{(MF)}_0\rangle$. In this case the corner space is composed of only a few shells of states and many superfluous rows and columns in the operator matrices can be eliminated at each step of the procedure outlined above.

Appendix C

List of publications

Peer-reviewed articles

1. **Corner space renormalization method for driven-dissipative 2D correlated systems**
   S. Finazzi, A. Le Boité, F. Storme, A. Baksic and C. Ciuti
   arXiv preprint, arxiv:1502.05651 (2015)

2. **Bose-Hubbard model: Relation between driven-dissipative steady-states and equilibrium quantum phases**
   A. Le Boité, G. Orso and C. Ciuti
   Physical Review A, **90**, 063621 (2014)

3. **Steady-states phases and tunneling-induced instabilities in the driven-dissipative Bose-Hubbard model**
   A. Le Boité, G. Orso and C. Ciuti
   Physical Review Letters, **110**, 233601 (2013)

Talks given at conferences

1. **PLMCN 2014, Montpellier (France)**
   Phase diagram of a driven-dissipative Bose-Hubbard model
   June 2014

2. **APS March Meeting, Baltimore (USA)**
   Phase diagram of a driven-dissipative Bose-Hubbard model
   March 2013

Bibliography

[1] A. D. Stone, *Einstein and the Quantum: The Quest of the Valiant Swabian*. Princeton University Press, 2013.

[2] P. A. M. Dirac, "Quantum theory of emission and absorption of radiation," *Proc. Roy. Soc. Lond. A*, vol. 114, p. 243, 1927.

[3] E. Fermi, "Quantum theory of radiation," *Reviews of Modern Physics*, vol. 4, no. 1, pp. 87–132, 1932.

[4] R. J. Glauber, "The quantum theory of optical coherence," *Physical Review*, vol. 130, no. 6, p. 2529, 1963.

[5] H. Kimble, M. Dagenais, and L. Mandel, "Photon antibunching in resonance fluorescence," *Physical Review Letters*, vol. 39, no. 11, p. 691, 1977.

[6] P. Kapitza, "Viscosity of liquid helium below the l-point," *Nature*, vol. 141, no. 3558, p. 74, 1938.

[7] M. H. Anderson, J. R. Ensher, M. R. Matthews, C. E. Wieman, and E. A. Cornell, "Observation of bose-einstein condensation in a dilute atomic vapor," *Science*, vol. 269, no. 5221, pp. 198–201, 1995.

[8] K. B. Davis, M.-O. Mewes, M. R. Andrews, N. Van Druten, D. Durfee, D. Kurn, and W. Ketterle, "Bose-einstein condensation in a gas of sodium atoms," *Physical Review Letters*, vol. 75, no. 22, p. 3969, 1995.

[9] M. Brambilla, L. Lugiato, V. Penna, F. Prati, C. Tamm, and C. Weiss, "Transverse laser patterns. ii. variational principle for pattern selection, spatial multistability, and laser hydrodynamics," *Physical Review A*, vol. 43, no. 9, p. 5114, 1991.

[10] K. Staliunas, "Laser ginzburg-landau equation and laser hydrodynamics," *Physical Review A*, vol. 48, no. 2, p. 1573, 1993.

[11] I. Carusotto and C. Ciuti, "Quantum fluids of light," *Reviews of Modern Physics*, vol. 85, pp. 299–366, Feb 2013.

[12] J. Kasprzak, M. Richard, S. Kundermann, A. Baas, P. Jeambrun, J. Keeling, F. Marchetti, M. Szymanska, R. Andre, J. Staehli, *et al.*, "Bose-Einstein condensation of exciton polaritons," *Nature*, vol. 443, no. 7110, pp. 409–414, 2006.

[13] I. Carusotto and C. Ciuti, "Probing microcavity polariton superfluidity through resonant rayleigh scattering," *Physical Review Letters*, vol. 93, p. 166401, Oct 2004.

[14] A. Amo, J. Lefrère, S. Pigeon, C. Adrados, C. Ciuti, I. Carusotto, R. Houdré, E. Giacobino, and A. Bramati, "Superfluidity of polaritons in semiconductor microcavities," *Nature Physics*, vol. 5, no. 11, pp. 805–810, 2009.

[15] G. Nardin, G. Grosso, Y. Léger, B. Pietka, F. Morier-Genoud, and B. Deveaud-Plédran, "Hydrodynamic nucleation of quantized vortex pairs in a polariton quantum fluid," *Nature Physics*, 2011.

[16] A. Amo, S. Pigeon, D. Sanvitto, V. Sala, R. Hivet, I. Carusotto, F. Pisanello, G. Lemenager, R. Houdre, E. Giacobino, *et al.*, "Hydrodynamic solitons in polariton superfluids," *Science*, vol. 332, no. 6034, pp. 1167–1170, 2011.

[17] S. Pigeon, I. Carusotto, and C. Ciuti, "Hydrodynamic nucleation of vortices and solitons in a resonantly excited polariton superfluid," *Physical Review B*, vol. 83, p. 144513, Apr 2011.

[18] D. Sanvitto, S. Pigeon, A. Amo, D. Ballarini, M. De Giorgi, I. Carusotto, R. Hivet, F. Pisanello, V. Sala, P. Guimaraes, *et al.*, "All-optical control of the quantum flow of a polariton condensate," *Nature Photonics*, vol. 5, no. 10, pp. 610–614, 2011.

[19] H. Flayac and V. Savona, "Input-output theory of the unconventional photon blockade," *Physical Review A*, vol. 88, no. 3, p. 033836, 2013.

[20] M. Greiner, O. Mandel, T. Esslinger, T. W. Hänsch, and I. Bloch, "Quantum phase transition from a superfluid to a mott insulator in a gas of ultracold atoms," *Nature*, vol. 415, no. 6867, pp. 39–44, 2002.

[21] S. Schmidt and J. Koch, "Circuit qed lattices: Towards quantum simulation with superconducting circuits," *Annalen der Physik*, vol. 525, no. 6, pp. 395–412, 2013.

[22] A. Le Boité, G. Orso, and C. Ciuti, "Bose-hubbard model: Relation between driven-dissipative steady states and equilibrium quantum phases," *Physical Review A*, vol. 90, no. 6, p. 063821, 2014.

[23] A. Le Boité, G. Orso, and C. Ciuti, "Steady-state phases and tunneling-induced instabilities in the driven dissipative bose-hubbard model," *Physical Review Letters*, vol. 110, no. 23, p. 233601, 2013.

[24] S. Finazzi, A. Le Boité, F. Storme, A. Baksic, and C. Ciuti, "Corner space renormalization method for driven-dissipative 2d correlated systems," *arXiv preprint arXiv:1502.05651*, 2015.

[25] J. W. Negele and H. Orland, *Quantum many-particle systems*. Westview, 1988.

[26] S. Weinberg, *The quantum theory of fields*, vol. 2. Cambridge university press, 1996.

[27] D. F. Walls and G. J. Milburn, *Quantum optics*. Springer, 2007.

[28] C. Cohen-Tannoudji, J. Dupont-Roc, and G. Grynberg, *Photons and Atoms: Introduction to Quantum Electrodynamics*. Wiley-VCH, 1989.

[29] R. Hanbury Brown and R. Twiss, "Correlation between photons in two coherent beams of light," *Nature*, vol. 177, no. 4497, pp. 27–29, 1956.

[30] J.-P. Gazeau, *Coherent states in quantum physics*. Wiley-VCH, 2009.

[31] E. Schrödinger, "Der stetige übergang von der mikro-zur makromechanik," *Naturwissenschaften*, vol. 14, no. 28, pp. 664–666, 1926.

[32] M. Hillery, "An introduction to the quantum theory of nonlinear optics," *Acta Physica Slovaca. Reviews and Tutorials*, vol. 59, no. 1, pp. 1–80, 2009.

[33] P. D. Drummond and M. Hillery, *The Quantum Theory of Nonlinear Optics*. Cambridge University Press, 2014.

[34] P. D. Drummond, "Electromagnetic quantization in dispersive inhomogeneous nonlinear dielectrics," *Physical Review A*, vol. 42, no. 11, p. 6845, 1990.

[35] J.-M. Raimond, M. Brune, and S. Haroche, "Manipulating quantum entanglement with atoms and photons in a cavity," *Reviews of Modern Physics*, vol. 73, no. 3, p. 565, 2001.

[36] M. Fleischhauer, A. Imamoglu, and J. P. Marangos, "Electromagnetically induced transparency: Optics in coherent media," *Reviews of Modern Physics*, vol. 77, no. 2, p. 633, 2005.

[37] B. Deveaud and (Ed.), *The Physics of Semiconductors Microcavities*. Wiley-CH, 2007.

[38] A. Kavokin, J. J. Baumberg, G. Malpuech, and F. P. Laussy, *Microcavities*. Oxford University Press, 2007.

[39] R. Schoelkopf and S. Girvin, "Wiring up quantum systems," *Nature*, vol. 451, no. 7179, pp. 664–669, 2008.

[40] J. You and F. Nori, "Atomic physics and quantum optics using superconducting circuits," *Nature*, vol. 474, no. 7353, pp. 589–597, 2011.

[41] A. Amo and J. Bloch, "Cavity polaritons: A crossroad between nonlinear optics and atomic condensates," in *Strong Light-Matter Coupling: From Atoms to Solid States Systems* (A. Auffèves, D. Gerace, M. Richard, S. Portolan, M. F. Santos, L. C. Kwek, and C. Miniatura, eds.), World Scientific, 2014.

[42] O. El Daıf, A. Baas, T. Guillet, J. Brantut, R. Kaitouni, J. Staehli, F. Morier-Genoud, and B. Deveaud, "Polariton quantum boxes in semiconductor microcavities," *Applied Physics Letters*, vol. 88, p. 061105, 2006.

[43] A. Verger, C. Ciuti, and I. Carusotto, "Polariton quantum blockade in a photonic dot," *Physical Review B*, vol. 73, p. 193306, May 2006.

[44] S. M. Girvin, "Circuit qed: superconducting qbits coupled to microwave photons," in *Quantum Machines: Measurement Control of Engineered Quantum Systems* (M. Devoret, B. Huard, R. Schoelkopf, and L. F. Cugliandolo, eds.), vol. 96, Oxford University Press, 2014.

[45] M. Devoret, "Lecture at college de france, quantum circuits and signals, 13 may 2008."

[46] F. R. Ong, M. Boissonneault, F. Mallet, A. Palacios-Laloy, A. Dewes, A. Doherty, A. Blais, P. Bertet, D. Vion, and D. Esteve, "Circuit qed with a nonlinear resonator:

ac-stark shift and dephasing," *Physical Review Letters*, vol. 106, no. 16, p. 167002, 2011.

[47] E. T. Jaynes and F. W. Cummings, "Comparison of quantum and semiclassical radiation theories with application to the beam maser," *Proceedings of the IEEE*, vol. 51, no. 1, pp. 89–109, 1963.

[48] C. Ciuti, G. Bastard, and I. Carusotto, "Quantum vacuum properties of the intersubband cavity polariton field," *Physical Review B*, vol. 72, no. 11, p. 115303, 2005.

[49] T. Niemczyk, F. Deppe, H. Huebl, E. Menzel, F. Hocke, M. Schwarz, J. Garcia-Ripoll, D. Zueco, T. Hümmer, E. Solano, *et al.*, "Circuit quantum electrodynamics in the ultrastrong-coupling regime," *Nature Physics*, vol. 6, no. 10, pp. 772–776, 2010.

[50] A. Ridolfo, M. Leib, S. Savasta, and M. J. Hartmann, "Photon blockade in the ultrastrong coupling regime," *Physical Review Letters*, vol. 109, no. 19, p. 193602, 2012.

[51] S. Haroche and J. M. Raimond, *Exploring the quantum*. Oxford University Press, 2006.

[52] T. Grujic, S. Clark, D. Jaksch, and D. Angelakis, "Non-equilibrium many-body effects in driven nonlinear resonator arrays," *New Journal of Physics*, vol. 14, no. 10, p. 103025, 2012.

[53] F. Petruccione and H.-P. Breuer, *The theory of open quantum systems*. Oxford university press, 2002.

[54] C. W. Beenakker, "Random-matrix theory of quantum transport," *Reviews of Modern Physics*, vol. 69, no. 3, p. 731, 1997.

[55] A. Imamoḡlu, H. Schmidt, G. Woods, and M. Deutsch, "Strongly interacting photons in a nonlinear cavity," *Physical Review Letters*, vol. 79, no. 8, pp. 1467–1470, 1997.

[56] C. Lang, D. Bozyigit, C. Eichler, L. Steffen, J. M. Fink, A. A. Abdumalikov, M. Baur, S. Filipp, M. P. da Silva, A. Blais, and A. Wallraff, "Observation of resonant photon blockade at microwave frequencies using correlation function measurements," *Physical Review Letters*, vol. 106, p. 243601, 2011.

[57] K. M. Birnbaum, A. Boca, R. Miller, A. D. Boozer, T. E. Northup, and H. J. Kimble, "Photon blockade in an optical cavity with one trapped atom," *Nature*, vol. 436, no. 7047, pp. 87–90, 2005.

[58] T. Liew and V. Savona, "Single photons from coupled quantum modes," *Physical Review Letters*, vol. 104, no. 18, p. 183601, 2010.

[59] M. Bamba, A. Imamoğlu, I. Carusotto, and C. Ciuti, "Origin of strong photon antibunching in weakly nonlinear photonic molecules," *Physical Review A*, vol. 83, p. 021802, Feb 2011.

[60] S. Ferretti, V. Savona, and D. Gerace, "Optimal antibunching in passive photonic devices based on coupled nonlinear resonators," *New Journal of Physics*, vol. 15, no. 2, p. 025012, 2013.

[61] D. Gerace and V. Savona, "Unconventional photon blockade in doubly resonant microcavities with second-order nonlinearity," *Physical Review A*, vol. 89, no. 3, p. 031803, 2014.

[62] M.-A. Lemonde, N. Didier, and A. A. Clerk, "Antibunching and unconventional photon blockade with gaussian squeezed states," *Physical Review A*, vol. 90, no. 6, p. 063824, 2014.

[63] M. P. A. Fisher, P. B. Weichman, G. Grinstein, and D. S. Fisher, "Boson localization and the superfluid-insulator transition," *Physical Review B*, vol. 40, pp. 546–570, Jul 1989.

[64] A. Greentree, C. Tahan, J. Cole, and L. Hollenberg, "Quantum phase transitions of light," *Nature Physics*, vol. 2, no. 12, pp. 856–861, 2006.

[65] D. G. Angelakis, M. F. Santos, and S. Bose, "Photon-blockade-induced mott transitions and xy spin models in coupled cavity arrays," *Physical Review A*, vol. 76, p. 031805, Sep 2007.

[66] M. Hartmann, F. Brandão, and M. Plenio, "Strongly interacting polaritons in coupled arrays of cavities," *Nature Physics*, vol. 2, no. 12, pp. 849–855, 2006.

[67] D. Rossini and R. Fazio, "Mott-insulating and glassy phases of polaritons in 1d arrays of coupled cavities," *Physical Review Letters*, vol. 99, no. 18, p. 186401, 2007.

[68] M. Schiró, M. Bordyuh, B. Öztop, and H. Türeci, "Phase transition of light in cavity qed lattices," *Physical Review Letters*, vol. 109, no. 5, p. 053601, 2012.

[69] I. Carusotto, D. Gerace, H. E. Tureci, S. De Liberato, C. Ciuti, and A. Imamoğlu, "Fermionized photons in an array of driven dissipative nonlinear cavities," *Physical Review Letters*, vol. 103, p. 033601, Jul 2009.

[70] M. J. Hartmann, "Polariton crystallization in driven arrays of lossy nonlinear resonators," *Physical Review Letters*, vol. 104, p. 113601, Mar 2010.

[71] J. Jin, D. Rossini, R. Fazio, M. Leib, and M. J. Hartmann, "Photon solid phases in driven arrays of nonlinearly coupled cavities," *Physical Review Letters*, vol. 110, no. 16, p. 163605, 2013.

[72] F. Nissen, S. Schmidt, M. Biondi, G. Blatter, H. E. Türeci, and J. Keeling, "Nonequilibrium dynamics of coupled qubit-cavity arrays," *Physical Review Letters*, vol. 108, p. 233603, Jun 2012.

[73] A. Tomadin, V. Giovannetti, R. Fazio, D. Gerace, I. Carusotto, H. E. Türeci, and A. Imamoglu, "Signatures of the superfluid-insulator phase transition in laser-driven dissipative nonlinear cavity arrays," *Physical Review A*, vol. 81, p. 061801, Jun 2010.

[74] J. Hubbard, "Electron correlations in narrow energy bands," *Proceedings of the Royal Society of London. Series A. Mathematical and Physical Sciences*, vol. 276, no. 1365, pp. 238–257, 1963.

[75] K. Sheshadri, H. Krishnamurthy, R. Pandit, and T. Ramakrishnan, "Superfluid and insulating phases in an interacting-boson model: mean-field theory and the rpa," *Europhysics Letters*, vol. 22, p. 257, 1993.

[76] J. Freericks and H. Monien, "Strong-coupling expansions for the pure and disordered bose-hubbard model," *Physical Review B*, vol. 53, no. 5, p. 2691, 1996.

[77] N. Elstner and H. Monien, "Dynamics and thermodynamics of the bose-hubbard model," *Physical Review B*, vol. 59, no. 19, p. 12184, 1999.

[78] K. Sengupta and N. Dupuis, "Mott-insulator-to-superfluid transition in the bose-hubbard model: a strong-coupling approach," *Physical Review A*, vol. 71, no. 3, pp. 033629_1–033629_8, 2005.

[79] P. Anders, E. Gull, L. Pollet, M. Troyer, and P. Werner, "Dynamical mean field solution of the bose-hubbard model," *Physical Review Letters*, vol. 105, p. 096402, Aug 2010.

[80] B. Capogrosso-Sansone, N. V. Prokof'ev, and B. V. Svistunov, "Phase diagram and thermodynamics of the three-dimensional bose-hubbard model," *Physical Review B*, vol. 75, p. 134302, Apr 2007.

[81] B. Capogrosso-Sansone, i. m. c. G. m. c. Söyler, N. Prokof'ev, and B. Svistunov, "Monte carlo study of the two-dimensional bose-hubbard model," *Physical Review A*, vol. 77, p. 015602, Jan 2008.

[82] A. Georges, "Lecture at college de france, bosonic mott transition and cold atoms, 19 may 2010."

[83] W. Krauth, M. Caffarel, and J.-P. Bouchaud, "Gutzwiller wave function for a model of strongly interacting bosons," *Physical Review B*, vol. 45, pp. 3137–3140, Feb 1992.

[84] S. Shamailov, A. Parkins, M. Collett, and H. Carmichael, "Multi-photon blockade and dressing of the dressed states," *Optics Communications*, vol. 283, no. 5, pp. 766–772, 2010.

[85] C. Cohen-Tannoudji, J. Dupont-Roc, and G. Grynberg, *Atom-photon interactions: basic processes and applications*. Wiley Online Library, 1992.

[86] L. D. Landau and E. M. Lifshitz, *Quantum Mechanics, Non-Relativistic Theory*. Pergamon Press, 1977.

[87] K. Cahill and R. Glauber, "Density operators and quasiprobability distributions," *Physical Review*, vol. 177, no. 5, p. 1882, 1969.

[88] C. Gardiner and P. Zoller, *Quantum noise: a handbook of Markovian and non-Markovian quantum stochastic methods with applications to quantum optics*, vol. 56. Springer, 2004.

[89] H. Carmichael, R. Brecha, and P. Rice, "Quantum interference and collapse of the wavefunction in cavity qed," *Optics Communications*, vol. 82, no. 1, pp. 73–79, 1991.

[90] P. Drummond and D. Walls, "Quantum theory of optical bistability. i. nonlinear polarisability model," *Journal of Physics A: Mathematical and General*, vol. 13, p. 725, 1980.

[91] R. Glauber, "Coherent and incoherent states of the radiation field," *Physical Review*, vol. 131, no. 6, pp. 2766–2788, 1963.

[92] E. Sudarshan, "Equivalence of semiclassical and quantum mechanical descriptions of statistical light beams," *Physical Review Letters*, vol. 10, no. 7, pp. 277–279, 1963.

[93] P. Drummond and C. Gardiner, "Generalised p-representations in quantum optics," *Journal of Physics A: Mathematical and General*, vol. 13, p. 2353, 1980.

[94] K. Husimi, "Some formal properties of the density matrix," *Proc. Phys. Math. Soc. Jpn*, vol. 22, no. 264, p. 123, 1940.

[95] D. van Oosten, P. van der Straten, and H. T. C. Stoof, "Quantum phases in an optical lattice," *Physical Review A*, vol. 63, p. 053601, Apr 2001.

[96] M. Endres, T. Fukuhara, D. Pekker, M. Cheneau, P. Schauss, C. Gross, E. Demler, S. Kuhr, and I. Bloch, "The 'higgs' amplitude mode at the two-dimensional superfluid/mott insulator transition," *Nature*, vol. 487, pp. 454–458, July 2012.

[97] S. D. Huber, E. Altman, H. P. Büchler, and G. Blatter, "Dynamical properties of ultracold bosons in an optical lattice," *Physical Review B*, vol. 75, p. 085106, Feb 2007.

[98] I. Carusotto and C. Ciuti, "Spontaneous microcavity-polariton coherence across the parametric threshold: Quantum monte carlo studies," *Physical Review B*, vol. 72, p. 125335, Sep 2005.

[99] K. G. Wilson, "The renormalization group: Critical phenomena and the Kondo problem," *Reviews of Modern Physics*, vol. 47, pp. 773–840, 1975.

[100] S. R. White and R. M. Noack, "Real-space quantum renormalization groups," *Physical Review Letters*, vol. 68, pp. 3487–3490, 1992.

[101] U. Schollwöck, "The density-matrix renormalization group," *Reviews of Modern Physics*, vol. 77, pp. 259–315, 2005.

[102] M. Fannes, B. Nachtergaele, and R. F. Werner, "Finitely correlated states on quantum spin chains," *Comm. Math. Phys.*, vol. 144, pp. 443–490, 1992.

[103] T. Xiang, J. Lou, and Z. Su, "Two-dimensional algorithm of the density-matrix renormalization group," *Physical Review B*, vol. 64, no. 10, p. 104414, 2001.

[104] F. Verstraete, M. M. Wolf, D. Pérez-García, and J. I. Cirac, "Criticality, the area law, and the computational power of projected entangled pair states," *Physical Review Letters*, vol. 96, no. 22, p. 220601, 2006.

[105] F. Verstraete, J. J. García-Ripoll, and J. I. Cirac, "Matrix Product Density Operators: Simulation of Finite-Temperature and Dissipative Systems," *Physical Review Letters*, vol. 93, no. 20, p. 207204, 2004.

[106] M. Zwolak and G. Vidal, "Mixed-State Dynamics in One-Dimensional Quantum Lattice Systems: A Time-Dependent Superoperator Renormalization Algorithm," *Physical Review Letters*, vol. 93, no. 20, p. 207205, 2004.

[107] T. Prosen and M. Žnidarič, "Matrix product simulations of non-equilibrium steady states of quantum spin chains," *J. Stat. Mech.*, vol. 2, p. 35, 2009.

[108] I. Pizorn, "One-dimensional bose-hubbard model far from equilibrium," *Physical Review A*, vol. 88, no. 4, p. 043635, 2013.

[109] Y. Castin, *Notes de cours de Master 2. Mécanique quantique avancée*, 2011.

[110] K. Mølmer, Y. Castin, and J. Dalibard, "Monte Carlo wave-function method in quantum optics," *J. Opt. Soc. Am. B*, vol. 10, pp. 524–538, 1993.

[111] H. Carmichael, *An open systems approach to quantum optics: lectures presented at the Université Libre de Bruxelles, October 28 to November 4, 1991*, vol. 18. Springer Science & Business Media, 1993.

[112] M. Plenio and P. Knight, "The quantum-jump approach to dissipative dynamics in quantum optics," *Reviews of Modern Physics*, vol. 70, no. 1, p. 101, 1998.

[113] R. Dum, A. S. Parkins, P. Zoller, and C. W. Gardiner, "Monte carlo simulation of master equations in quantum optics for vacuum, thermal, and squeezed reservoirs," *Physical Review A*, vol. 46, pp. 4382–4396, 1992.